FLUID MECHANICS RESEARCH

Vol. 37 **No. 3** **2010**

CONTENTS

Computational Modelling of MHD Flow and Mass Transfer in Stretching Sheet with Slip Effects at the Porous Surface[†]

Dulal Pal[1] and **Babulal Talukdar**[2]

[1]Department of Mathematics, Visva-Bharati University,
Santiniketan, West Bengal-731 235, India
E-mail: dulalp123@rediffmail.com

[2]Department of Mathematics, Gobindapur High School,
Murshidabad-742 225, West Bengal, India

This paper presents a perturbation and numerical analysis of the flow and mass transfer characteristics of Newtonian fluid flowing in a horizontal channel with lower side being a stretching sheet and upper being permeable plate bounded by porous medium in presence of transverse magnetic field. The governing nonlinear equations and their associated boundary conditions are first cast into dimensionless forms by a local non-similar transformation. The resulting equations are then solved using perturbation method and the finite difference scheme. Numerical results for flow and concentration distribution and the skin-friction coefficient have been obtained for different values of the governing parameters numerically and their values are presented through table and graphs. The effects of various physical parameters Hartman number, Reynolds number, slip parameter etc. on dimensionless horizontal and vertical velocities and also on mass transfer characteristics are discussed in detail. In particular, the effect of slip velocity at interfacial surface on skin friction factor is found to be more pronounced in a system for higher value of magnetic field. The results also show that the magnetic field parameter has a significant influence on the fluid flow and mass transfer characteristics.

* * *

Nomenclature

$\boldsymbol{B}$	magnetic induction intensity vector;
B_0	magnetic intensity;
C	dimensionless concentration;
C_f	skin friction coefficient;

[†]Received 27.11.2008

ISSN 1064-2277
© 2010 Begell House, Inc.

c	stretching parameter;
c_0	uniform concentration;
c_w	unknown solute concentration;
D	diffusion coefficient;
$\boldsymbol{E}$	electric field intensity vector;
h	width of the channel;
$\boldsymbol{J}$	electric current density vector;
k	the porous permeability parameter;
M	Hartmann number;
$\boldsymbol{q}$	the velocity vector;
Re	stretching Reynolds number;
$\mathrm{Re}_c = R_c$	cross-flow Reynolds number;
$\mathrm{Re}_{\mathrm{ent}}$	entrance Reynolds number;
u^*	velocity component along x^*-axis;
u_{slip}	slip velocity at porous wall;
u_0	uniform inlet velocity;
v^*	velocity component along y^*-axis;
v_w	vertical velocity at the porous layer;
x^*	distances along the plate;
x	dimensionless distances along the plate;
y^*	distances perpendicular to the plate;
y	dimensionless distances perpendicular to the plate.

Greek symbols

α	slip parameter depends on structure of the porous medium;
μ	dynamic viscosity;
μ_m	magnetic permeability;
ν	kinematic viscosity;
ϕ	porous parameter;
ρ	density;
σ	magnetic conductivity;
τ	friction coefficient.

Superscripts

$'$	differentiation with respect to y;
*	dimensional properties.

Subscripts

j	grid point along x direction;
m	grid point along y direction;
w	wall condition.

Introduction

In recent years considerable attention has been given to study boundary layer flows of viscous fluids over a stretching sheet. This is due to its important applications in engineering, such as the

aerodynamic extrusion of plastic sheets, the boundary layer along a liquid film condensation process, the cooling process of metallic plate in a cooling bath, and in glass and polymer industries. In 1961 Sakiadis [1] initiated the study of boundary layer flows over a flat plate. He considered the boundary layer flow over a flat surface moving with a constant velocity and formulated a boundary layer equation for two-dimensional and axisymmetric flows. The Sakiadis study was further extended to the stretching flat plate by Crane [2]. The work of Sakiadis and Crane was further extended by many researchers to include many other physical investigations such as; suction or injection, heat or mass transfer analysis and magnetohydrodynamic flows etc. The study of boundary layer flows over a stretching surface for impermeable plate was done by Banks [3], Banks and Zaturska [4], Grubka and Bobba [5], Ali [6], and Ariel [7] whereas studied for the permeable plate were done by Erickson [8], Gupta and Gupta [9], Chen and Char [10], Chaudhary et al. [11], Elbashbeshy [12] and Magyari and Keller [13]. In all the above research work, the authors have considered the flows due to stretching of the wall over an infinite plate with unbounded domain.

Magneto-hydrodynamics (MHD) is the branch of continuum mechanics which deals with the flow of electrically conducting fluids in electric and magnetic fields. Magneto-hydrodynamic equations are ordinary electromagnetic and hydrodynamic equations modified to take into account the interaction between the motion of the fluid and the electromagnetic field. The formulation of the electromagnetic theory in a mathematical form is known as Maxwell's equation. Hartmann flow is a classical problem that has important applications in magnetohydrodynamic (MHD) power generators and pumps, accelerators, aerodynamic heating, electrostatic precipitation, polymer technology, the petroleum industry, and purification of crude oil and fluid droplets and sprays. Hartmann and Lazarus [14] studied the influence of a transverse uniform magnetic field on the flow of a viscous incompressible electrically conducting fluid between two infinite parallel stationary and insulating plates. The problem was then extended in numerous ways.

A very little attention has been given to the channel flows driven due to stretching surface. In 1983, Borkakoti and Bharali [15] studied the hydromagnetic flow and heat transfer in a fluid bounded by two parallel plates where the lower plate is stretching at a different temperature and the upper plate is subjected to uniform injection. The effects of rotation on the hydromagnetic flow between two parallel plates studied by Banerjee [16], where the upper plate is porous and solid, and the lower plate is a stretching sheet by using perturbation technique up to first-order of approximation. These perturbation results are only valid for small values of the Reynolds number. Vajravelu and Kumar [17] obtained analytic (perturbation) as well as numerical solutions of the nonlinear coupled system arising in axially symmetric hydromagnetic flow between two horizontal plates in a rotating system where the lower plate being a stretching sheet and the upper plate is subjected to uniform injection.

The no-slip boundary condition is widely used for flows involving Newtonian fluids past solid boundaries. However, it has been found that a large class of polymeric materials slip or stick-slip on solid boundaries. For instance, when polymeric melts flow due to an applied pressure gradient, there is a sudden increase in the throughput at a critical pressure gradient. Berman [18] was the first to study flows in composite layers under a uniform withdrawal of flux through the walls. He obtained a solution by a perturbation technique for velocity field using the no-slip condition. No-slip boundary conditions are a convenient idealization of the behavior of viscous fluids near walls. The boundary conditions relevant to flowing fluids are very important in predicting fluid flows in many applications. Since most naturally occurring media are porous in structure, a study of convection in porous media is important. Beavers and Joseph [19] found experimentally that when fluid flows in a parallel plate channel, one of whose walls is a porous medium, there is a velocity slip at the porous wall. They have shown that the shear effects are transmitted into the permeable medium

through a boundary layer region and proposed a slip condition at the fluid-porous medium boundary. Similar kinds of problems were further studied by Blythe and Simpkins [20] and Richardson [21]. Saffman [22] showed that for small permeability the following expression is sufficient to calculate the slip velocity u_{slip}, as being proportional to the shear rate:

$$u_{\text{slip}} = \frac{\sqrt{k}}{\alpha}\left(\frac{\partial u}{\partial y}\right) + O(k), \tag{1}$$

where k is the permeability and α is a porous parameter depending upon the structure of the porous medium.

The study of mass transfer, in such a type of flow in a porous channel is of great importance in geophysics and engineering science. In recent years a considerable amount of work has been devoted to the study of natural and mixed convection in porous media/channels. It seems reasonable to investigate the effect of slip boundary conditions (assuming that the slip velocity depends on the shear stress only) on the dynamics of fluids in porous media by studying the flow of a Newtonian fluid in a parallel plate channel. The effect of the shear stress on the slip velocity was studied by Rao and Rajagopal [23]. They studied the effect of slip boundary conditions on the flow of the fluids in a channel. They investigated the flow of a linearly viscous fluid when the slip depends on both the shear stress and the normal stress. If the shear stress at the wall is greater than the critical shear stress, the flow slips at the wall and conversely if the shear stress is not large enough, then the classical Poiseulle solution with no-slip is observed. Singh and Laurence [24] studied the concentration polarization in a composite layer using the $\boldsymbol{BJ}$-slip condition. Rudraiah and Musuoka [25] have investigated the effect of slip and magnetic field on composite systems analytically and numerically. They obtained important characteristics of the conducting flow as well as the concentration fields in the composite layer. In real systems there is always a certain amount of slip, which, however, is hard to detect experimentally because of the required space resolution. Later, Shivakumara et al. [26] studied concentration polarization in MHD flow in composite systems using $\boldsymbol{BJ}$-slip condition analytically and numerically.

In the present work, the steady Hartmann flow of a viscous incompressible electrically conducting fluid is studied with mass transfer. The fluid is flowing between two electrically insulating plates, lower being stretching sheet and upper is covered by a porous media, and uniform suction and injection is applied through the permeable surface. An external uniform magnetic field is applied perpendicular to the stretching sheet. The magnetic Reynolds number is assumed small so that the induced magnetic field is neglected (Sutton and Sherman [27]). Chakraborty and Gupta [28] investigated on the motion of an electrically conducting fluid past a horizontal plate in the motion being caused solely by the stretching of the plate. Thus in this paper the effects of slip on the hydromagnetic flow and mass transfer between two horizontal plates, the lower being a stretching sheet and the upper a porous solid plate have been studied. The coupled set of the equations of motion and the diffusion equation including the viscous nonlinear equations are solved analytically and numerically using finite-difference approximations to obtain the velocity and concentration distributions. We consider a problem analogous to the forced convection where the momentum equation is independent of concentration distribution and the diffusion equation is coupled with the velocity distribution. The momentum equation is solved analytically, under the assumption of two-dimensional motion, for velocity distribution. A first-order perturbation technique satisfying the slip velocity at the porous surface is used. Knowing the velocity field, we solve the diffusion equation numerically by employing a finite-difference method.

1. Formulation of the Problem

Consider the steady flow of an electrically conducting viscous fluid in a porous medium which is bounded by two horizontal non-conducting plates where the lower plate is taken as stretching sheet and upper is a permeable porous plate which is shown in Fig. 1. The fluid is assumed to be flowing between two horizontal plates located at the $y^* = 0, h$ planes. The two plates are assumed to be electrically insulating and a uniform magnetic field Bo is applied in the positive y-direction.The fluid is permeated by a strong magnetic field $\boldsymbol{B} = [0; B_0(x^*); 0]$. MHD equations are the usual electromagnetic and hydrodynamic equations, but they are modified to take account of the interaction between the motion and the magnetic field. As in most problems involving conductors, Maxwell's displacement currents are ignored so that electric currents are regarded as flowing in closed circuits. Assuming that the velocity of flow is too small compared to the velocity of light, that is, the relativistic effects are ignored. The system of Maxwell's equations can be written in the form:

$$\begin{aligned} \nabla \times \boldsymbol{B} = \mu \boldsymbol{J}, \qquad \nabla \cdot \boldsymbol{J} = 0, \\ \nabla \times \boldsymbol{E} = 0, \qquad \nabla \cdot \boldsymbol{B} = 0. \end{aligned} \tag{2}$$

When magnetic field is not strong then electric field and magnetic field obey Ohm's law which can be written in the form

$$\boldsymbol{J} = \sigma(\boldsymbol{E} + \boldsymbol{q} \times \boldsymbol{B}), \tag{3}$$

where $\boldsymbol{B}$ is the magnetic induction intensity, $\boldsymbol{E}$ is the electric field intensity, $\boldsymbol{J}$ is the electric current density, μ is the magnetic permeability, and σ is the electrical conductivity. In the equation of motion, the body force $\boldsymbol{J} \times \boldsymbol{B}$ per unit volume is added. This body force represents the coupling between the magnetic field and the fluid motion which is called Lorentz force. The induced magnetic field is assumed to be negligible. This assumption is justified by the fact that the magnetic Reynolds number is very small. This is a rather important case for some practical engineering problems where the conductivity is not large in the absence of an externally applied field and with negligible effects of polarization of the ionized gas. It has been taken that $\boldsymbol{E} = 0$. That is, in the absence of convection outside the boundary layer, $\boldsymbol{B} = B_0$ and $\nabla \times \boldsymbol{B} = \mu \boldsymbol{J} = 0$, then Eq. (2) leads to $\boldsymbol{E} = 0$. Thus, the Lorentz force becomes

$$\boldsymbol{J} \times \boldsymbol{B} = \sigma(\boldsymbol{E} + \boldsymbol{q} \times \boldsymbol{B}) \times \boldsymbol{B}.$$

In what follows, the induced magnetic field will be neglected. This is justified if the magnetic Reynolds number is small. Hence, to get a better degree of approximation, the Lorentz force can be

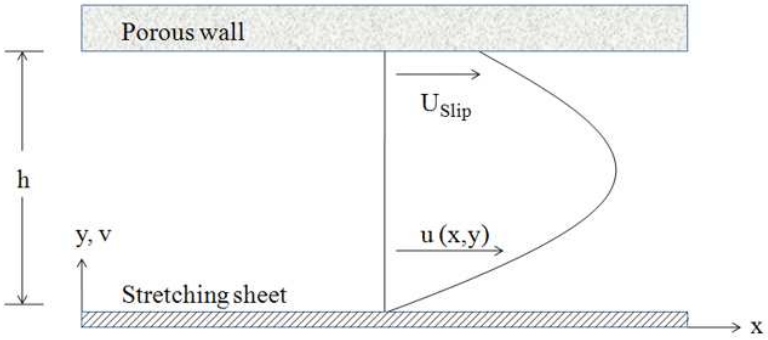

Fig. 1. Physical configuration of the problem.

replaced by

$$\sigma(\boldsymbol{E}+\boldsymbol{u}\times\boldsymbol{B})\times\boldsymbol{B}=-\sigma B_0^2\boldsymbol{u},$$

where $\boldsymbol{u}$ is used for velocity vector.

The equations of motion can be put into the following forms for steady flow:

$$\frac{\partial u^*}{\partial x^*}+\frac{\partial v^*}{\partial y^*}=0, \tag{4}$$

$$u^*\frac{\partial u^*}{\partial x^*}+v^*\frac{\partial p^*}{\partial y^*}=-\frac{1}{\rho}\frac{\partial p^*}{\partial x^*}+\nu\left(\frac{\partial^2 u^*}{\partial x^{*2}}+\frac{\partial^2 u^*}{\partial y^{*2}}\right)-\frac{\sigma B_0^2}{\rho}u^*, \tag{5}$$

$$u^*\frac{\partial v^*}{\partial x^*}+v^*\frac{\partial v^*}{\partial y^*}=-\frac{1}{\rho}\frac{\partial p^*}{\partial y^*}+\nu\left(\frac{\partial^2 v^*}{\partial x^{*2}}+\frac{\partial^2 v^*}{\partial y^{*2}}\right), \tag{6}$$

where u^*, v^* are the fluid velocity components along the x^*- and y^*-axes; ρ is the density; ν is the kinematic viscosity; σ is the magnetic conductivity; B_0 is the magnetic intensity.

The boundary conditions are:

$$\begin{aligned} &y^*=0, \qquad u^*=cx^*, && v^*=0,\\ &y^*=h, \qquad u^*=u_{\text{slip}}=-\frac{\sqrt{k}}{\alpha h}\frac{\partial u^*}{\partial y^*}, && v^*=v_w, \end{aligned} \tag{7}$$

where c is the stretching parameter v_w is the vertical velocity in the porous layer, k the permeability of the porous medium, α is the slip parameter, h is the width of the channel.

2. Formulation of the Problem and Method of Solution

2.1. Flow analysis. To solve the governing equations (5) and (6), we use the following non-dimensional quantities:

$$u^*=cx^*f'(y), \qquad v^*=-chf(y), \qquad p^*=\frac{\mu u_0 p}{h}, \qquad x=\frac{x^*}{h}, \qquad y=\frac{y^*}{h}, \tag{8}$$

where $f'(y)$ is the dimensionless stream function.

Using Eq. (8), we get from Eqs. (5) and (6) as

$$-\frac{1}{\rho}\frac{\mu u_0}{h^2}\frac{\partial p}{\partial x}=c^2xh\left[f'^2-ff''-\frac{f'''}{\mathrm{Re}}+\frac{\mathrm{M}^2}{\mathrm{Re}}f'\right], \tag{9}$$

$$-\frac{1}{\rho}\frac{\mu u_0}{h^2}\frac{\partial p}{\partial y}=c^2h\left[ff'-\frac{f''}{\mathrm{Re}}\right], \tag{10}$$

where $\mathrm{Re}=ch^2/\nu$ is the stretching Reynolds number; $\mathrm{M}=\sqrt{\sigma/(\nu\rho)}\,B_0h$ is the Hartmann number; c is stretching parameter.

Eliminating p between Eqs. (5) and (6), we get

$$f'''-\mathrm{Re}(f'^2-ff'')-\mathrm{M}^2f'=A, \tag{11}$$

where A is a constant to be determined.

The corresponding boundary conditions are obtained from Eq. (7) using Eq. (8) as

$$\begin{aligned} y=0: \qquad & f'=1, && f=0, \\ y=1: \qquad & f'=-\frac{\sqrt{k}}{\alpha h^2}=-\phi f'', && f=-\frac{v_w}{ch}=\mathrm{Re}_c, \end{aligned} \tag{12}$$

where $\mathrm{Re}_c(=v_w/ch)$ the cross-flow Reynolds number.

For small values of Re (stretching Reynolds number), the regular perturbation technique for f and A can be expressed in the following form:

$$f=\sum_{n=0}\mathrm{Re}^n f_n, \qquad A=\sum_{n=0}\mathrm{Re}^n A_n. \tag{13}$$

Substituting Eq. (8) in Eq. (11) and comparing like powers of Re, we have

$$f_0'''-\mathrm{M}^2 f_0'=A_0, \tag{14}$$

$$f_1'''-\mathrm{M}^2 f_1'=A_1+({f_0'}^2-f_0 f_0''). \tag{15}$$

The corresponding boundary conditions are obtained from Eq. (12) as

$$\begin{aligned} y=0: \qquad & f_0=0, && f_0'=1, && f_n=f_n'=0, && n>1, \\ y=1: \qquad & f_0=\mathrm{Re}_c, && f_n=0, && f_n'=-\phi f_n'', && n\geq 0. \end{aligned} \tag{16}$$

Through straight forward algebra, the solution of f_0, f_1 are obtained from Eqs. (14) and (15) using Eqs. (16) and given by

$$\begin{aligned} f_0 &= c_1+c_2e^{\mathrm{M}y}+c_3e^{-\mathrm{M}y}-\frac{A_0}{\mathrm{M}^2}y, \\ f_1 &= c_4+c_5e^{\mathrm{M}y}+c_6e^{-\mathrm{M}y}-\frac{A_1}{\mathrm{M}^2}y-\frac{R_1}{\mathrm{M}^2}y-\frac{R_2e^{\mathrm{M}y}}{2\mathrm{M}^2}y \\ &\quad +\frac{R_3e^{\mathrm{M}y}}{2\mathrm{M}^2}\left(\frac{y^2}{2}-\frac{3}{2M}y\right)+\frac{R_4e^{-\mathrm{M}y}}{2\mathrm{M}^2}y+\frac{R_5e^{-\mathrm{M}y}}{2\mathrm{M}^2}\left(\frac{y^2}{2}+\frac{3}{2M}y\right), \end{aligned} \tag{17}$$

where c_1 to c_6; A_1; R_1 to R_5 are constants (see Appendix).

The velocity profile can now be written as

$$u(x,y)=\frac{\mathrm{Re}}{\mathrm{Re}_{\mathrm{ent}}}\,x(f_0'+\mathrm{Re}\,f_1') \qquad \text{and} \qquad v(y)=-\frac{1}{\mathrm{Re}_c}(f_0+\mathrm{Re}\,f_1),$$

where $\mathrm{Re}_{\mathrm{ent}}=u_0h/\nu$ is the entrance Reynolds number.

The most important physical quantities are Skin friction coefficient C_f defined as

$$C_f=\frac{(\tau_{xy})_{y^*=0,h}}{\rho c^2h^2}=\frac{x}{\mathrm{Re}}\,(f'')_{y=0,1}\,. \tag{18}$$

2.2. Mass transfer analysis. It is assumed that the diffusion in the axial direction is neglected in comparison to diffusion in the transverse direction since in all tangential flow membrane system, $v_w \ll u_0$. Thus two-dimensional convection-diffusion equation describing the transfer of mass at steady state of such a system is given by

$$u^* \frac{\partial c^*}{\partial x^*} + v^* \frac{\partial c^*}{\partial y^*} = D \frac{\partial^2 c^*}{\partial y^{*2}}\,, \tag{19}$$

where D is the diffusion coefficient of the solute and c^* denotes the concentration of the solute. Eq. (19) along with the boundary conditions given below constitute a complete description of mass transfer in a membrane system.

$$\begin{aligned} \frac{\partial c^*}{\partial y^*} &= 0 \qquad \text{at} \qquad y^* = 0, \\ D\frac{\partial c^*}{\partial y^*} &= v^* c_w \qquad \text{at} \qquad y^* = h, \\ c^* &= c_0 \qquad \text{at} \qquad x^* = 0. \end{aligned} \tag{20}$$

No-flux boundary condition at the solid wall is imposed (see the first of above relations) and the second one is the boundary condition for a perfectly rejecting membrane, i. e., no solute passes through the porous interface. Hence, at steady state the convective transport of solute towards the porous wall is balanced by diffusive back transport of material in the side of the flow continuum. This dynamic exchange of material results in a steady concentration boundary layer thickness c_w represents the unknown solute concentration at the porous wall and c_0 is a free stream uniform concentration.

2.3. Numerical solution of the mass transfer problem. We now introduce the following non-dimensional variables:

$$u = \frac{u^*}{u_0}\,, \qquad v = \frac{v^*}{v_w}\,, \qquad C = \frac{c^*}{c_0}\,, \qquad x = \frac{x^*}{h}\,, \qquad y = \frac{y^*}{h}\,. \tag{21}$$

Using Eq. (21) in Eq. (19) and rearranging to get in dimensionless form as follows,

$$u \frac{\partial C}{\partial x} + \frac{v_w}{u_0} v \frac{\partial C}{\partial y} = \frac{D}{u_0 h} \frac{\partial^2 C}{\partial y^2}\,. \tag{22}$$

The boundary conditions (20) are also expressed in dimensionless form as

$$\begin{aligned} C &= 1 \qquad \text{at} \qquad x = 0, \qquad \forall\, y, \\ \frac{\partial C}{\partial y} &= 0 \qquad \text{at} \qquad y = 0, \qquad \forall\, x, \\ \frac{\partial C}{\partial y} &= v\, \frac{v_w h}{D}\, \frac{c_w}{c_0} \qquad \text{at} \qquad y = 1, \qquad \forall\, x. \end{aligned} \tag{23}$$

Let the channel inlet and exit be denoted by $m = 1$ and $m = m_{\max}$ respectively; the solid and porous walls are represented by $j = 1$ and $j = j_{\max}$. Introduce the backward difference approximation for the derivatives in Eq. (22) and rearrange the finite difference equation:

$$A_j C_{j-1,m} + B_j C_{j,m} + E_j C_{j+1,m} = F_j \qquad \text{for} \qquad 2 \le j \le j_{\max} - 1, \tag{24}$$

where

$$A_j = -v_j \frac{v_w}{u_0} \frac{1}{\Delta\lambda} - \frac{D}{u_0 h} \frac{1}{(\Delta y)^2} ,$$

$$B_j = \frac{u_j}{\Delta x} + v_j \frac{v_w}{u_0} \frac{1}{\Delta y} + 2\frac{D}{u_0 h} \frac{1}{(\Delta y)^2} ,$$

$$E_j = -\frac{D}{u_0 h} \frac{1}{(\Delta y)^2} ,$$

$$F_j = \frac{u_j}{\Delta x} C_{j,m-1} .$$

These coefficient are valid for all the interior points. At the porous and solid boundaries we use the second and the third boundary conditions of Eq. (23) and simplify to get the finite-difference equation valid at the solid wall as follows:

$$B_1 c_{1,m} + E_1 c_{2,m} = 0 \qquad \text{for} \qquad j = 1. \tag{25}$$

The coefficients B_1 and E_1 are

$$B_1 = v_1 \frac{v_w}{u_0} \frac{1}{\Delta y} + \frac{D}{u_0 h} \frac{1}{(\Delta y)^2} ,$$

$$E_1 = -v_1 \frac{v_w}{u_0} \frac{1}{\Delta y} - \frac{D}{u_0 h} \frac{1}{(\Delta y)^2} .$$

The finite-difference equation at the porous wall can be obtained similarly as

$$A_{j_{\max}} C_{j_{\max}-1,m} + B_{j_{\max}} C_{j_{\max} m} = F_{j_{\max}} \qquad \text{for} \qquad j = j_{\max}. \tag{26}$$

The coefficients are as given below:

$$A_{j_{\max}} = -v_{j_{\max}} \frac{v_w}{u_0} \frac{1}{\Delta y} - 2\frac{D}{u_0 h} \frac{1}{(\Delta y)^2} ,$$

$$B_{j_{\max}} = \frac{u_{j_{\max}}}{\Delta x} - v_{j_{\max}} \frac{v_w}{u_0} \frac{1}{\Delta y} + 2\frac{D}{u_0 h} \frac{1}{(\Delta y)^2} ,$$

$$F_{j_{\max}} = \frac{u_{j_{\max}}}{\Delta x} C_{j_{\max} m-1} ,$$

These cofficients constitute a tridiagonal system of the form

$$\begin{bmatrix} B_1 & E_1 & & & & & \\ A_2 & B_2 & E_2 & & & & \\ & A_3 & B_3 & E_3 & & & \\ & \cdots & \cdots & \cdots & \cdots & \cdots & \cdots \\ & & & A_i & B_i & E_i & \\ & \cdots & \cdots & \cdots & \cdots & \cdots & \cdots \\ & & & & A_{j_m-1} & B_{j_m-1} & E_{j_m-1} \\ & & & & & A_{j_m} & B_{j_m} \end{bmatrix} \begin{bmatrix} C_1 \\ C_2 \\ C_3 \\ . \\ . \\ . \\ C_{j_m-1} \\ C_{j_m} \end{bmatrix} = \begin{bmatrix} F_1 \\ F_2 \\ F_3 \\ . \\ . \\ . \\ F_{j_m-1} \\ F_{j_m} \end{bmatrix}, \tag{27}$$

where $F_{j_m-1} = F_{j_{\max}-1}$, $F_{j_m} = F_{j_{\max}}$.

The system of linear equations (24), (25) and (26) is then solved more effectively using Thomas algorithm for tridiagonal matrix.

3. Results and Discussions

Analytical and numerical solutions of the flow and mass transfer characteristics of Newtonian fluid in a horizontal channel bounded below by stretching sheet and above with a porous wall are presented. The effects of various physical parameters on velocity and mass transfer are analyzed with the help of graphs and tables.The variation of velocity distribution with y for different values of the porous parameter ϕ in the boundary layer are shown in Fig. 2. It is seen that the velocity distribution in the boundary layer decreases with increasing the value of porous parameter. The effect of porous parameter ϕ on variation of transverse velocity in the boundary layer for fixed values of M, Re and Re_c is shown in Fig. 3. It is interesting to note that the effect of ϕ is to decrease the transverse velocity in the boundary layer. This is due to the fact that the presence of porous medium is to increase the resistance to the flows which causes the horizontal fluid velocity to decrease. The variation of horizontal and vertical velocity profiles for different values of Re_c in the boundary layer are shown in Figs. 4 and 5, respectively. From these figures, it is clearly seen that horizontal and vertical velocity decreases with decreasing the value of the parameter Re_c.

Fig. 6 shows that the variation of horizontal velocity with y for various values of M. It is seen that horizontal velocity increases with increase in the values of M closer to the stretching sheet whereas it decreases near to the porous wall. It is interesting to note that the effect of M is to increase vertical velocity in the boundary layer and this effect is more prominent close to the wall as shown in Fig. 7. The variation of horizontal and vertical velocities for various values of Re is depicted in Figs. 8 and 9. It is clearly seen from these figures that the increasing the value of Re, the vertical velocity increases in the channel. The effect is more significant near the porous boundary. Fig. 10 shows that the horizontal fluid velocity increases due to increase in stretching Reynolds number Re and on the other hand it decreases with increase in Hartmann number near to the porous wall and reverse trend is seen closer to the stretching sheet. Further, it is observed that the longitudinal velocity increases with cross-flow Reynolds number Re_c near the lower stretching plate and the reverse effect is noted near the upper porous plate for a fixed porous parameter $\phi = 0.001$. From Fig. 11 it is seen that the transverse velocity distribution across the boundary layer increases due to increase in Hartmann number M and cross-flow Reynolds number Re_c for small values of porous parameter ϕ.

Fig. 12 depicts the variation of concentration distribution in the channel for different values of Hartmann number. From this figure it is observed that the concentration decreases with Hartmann number. This is due to the fact that by increasing the value of Hartmann number, there is increase in the vertical velocity of the fluid in the channel. Fig. 13 is the plot of concentration distribution in the channel for various values of porous permeability parameter ϕ. It is interesting to note that the concentration increases with increase in the porous permeability parameter because the velocity of the fluid decreases in presence of porous medium since resistance is offered to the fluid by the porous medium.

In Fig. 14 the variation of the concentration distribution with y for various values of cross-flow Reynolds number is shown. It is clearly seen from this figure that the concentration increases with increase in Re_c. Fig. 15 depicts the concentration distribution in the channel in x-direction for various values of porous permeability parameter ϕ. It is observed that concentration increases with increase in the porous permeability parameter along the channel, this is due to the fact the presence of the porous medium opposes the fluid motion which results in lower value of concentration. Fig. 16 illustrates the concentration distribution in the channel in x-direction for various values of Hartmann number M. It is clearly seen from this figure that concentration decreases with M along the channel. Fig. 17 displays the concentration distribution in the channel in x-direction for various

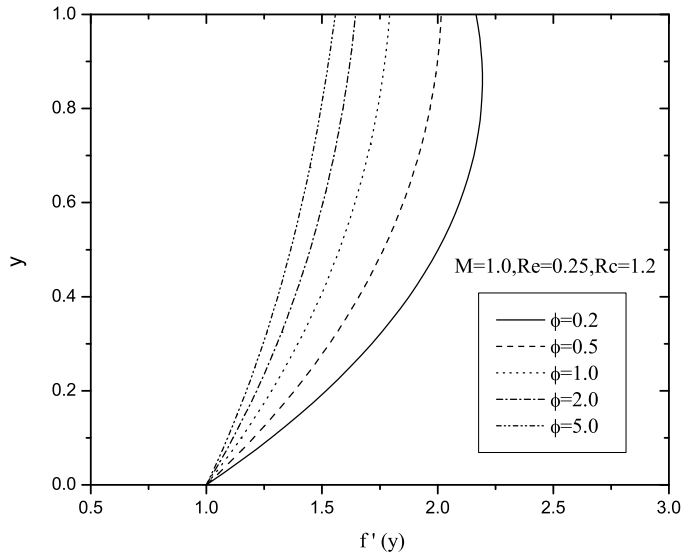

Fig. 2. Variation of $f'(y)$ with y for various porous parameter ϕ.

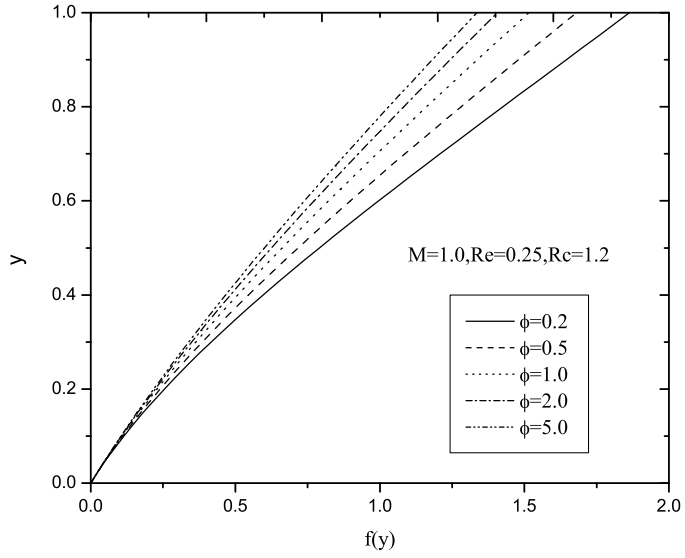

Fig. 3. Variation of transverse velocity with y for different values of ϕ.

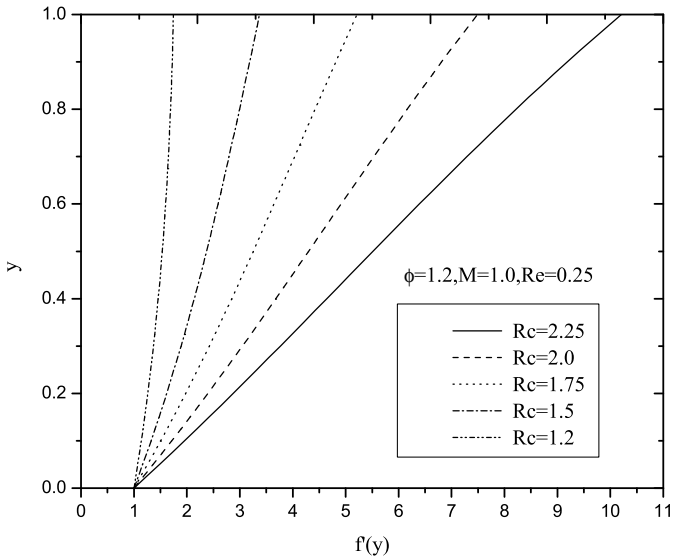

Fig. 4. Variation of $f'(y)$ with y for different values of Re_c .

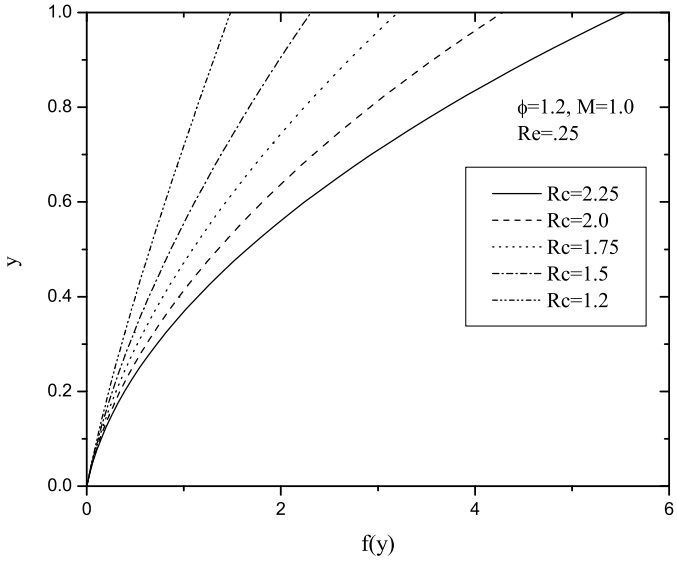

Fig. 5. Variation of transverse velocity with y for different values of Re_c .

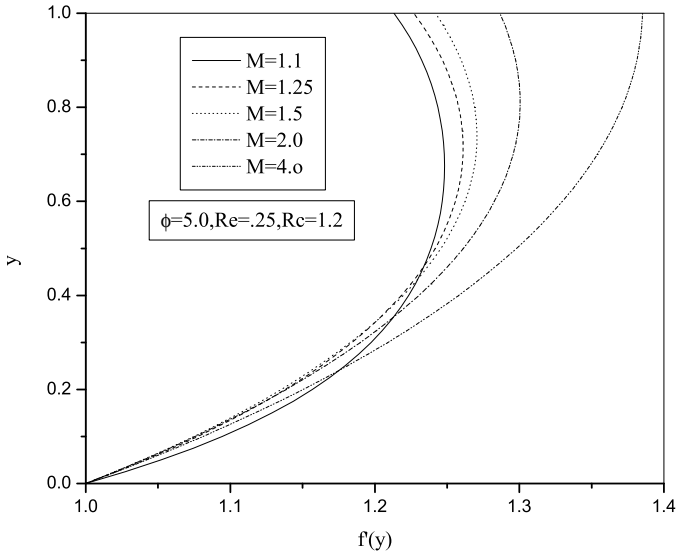

Fig. 6. Variation of $f'(y)$ with y for various values of M.

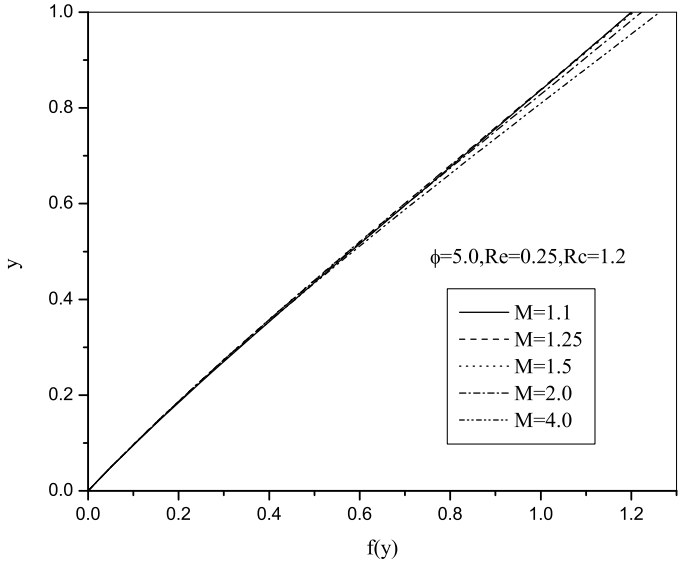

Fig. 7. Variation of $f(y)$ with y for different values of M.

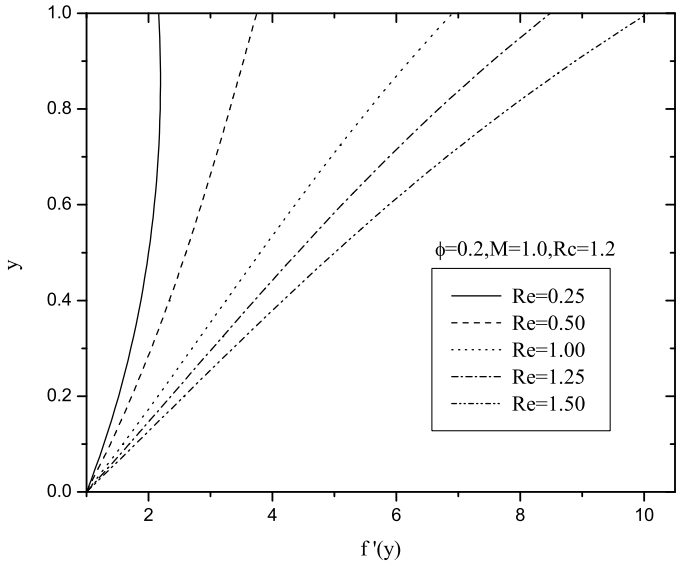

Fig. 8. Variation of $f'(y)$ with y for different values of Re.

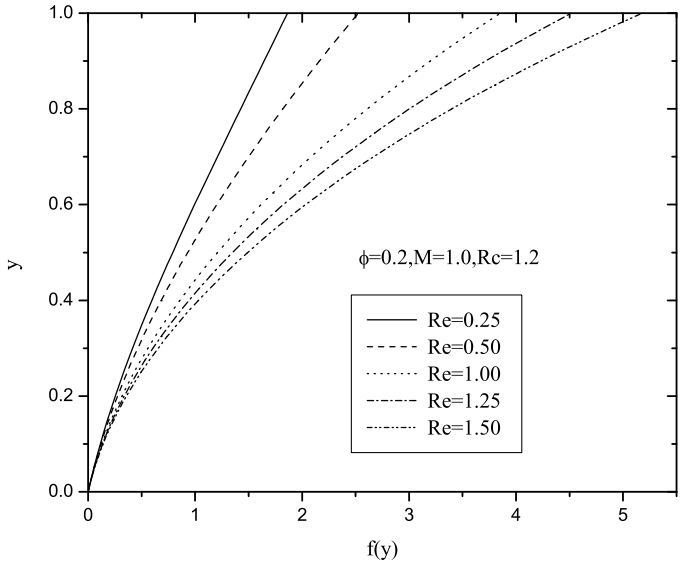

Fig. 9. Variation of $f(y)$ with y for different values of Re.

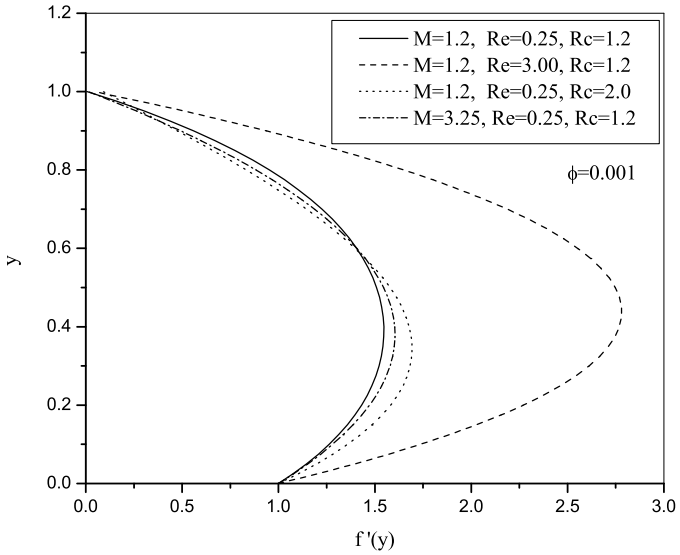

Fig. 10. Variation of $f'(y)$ with y for various values of M, Re and Re_c when $\phi = 0.001$.

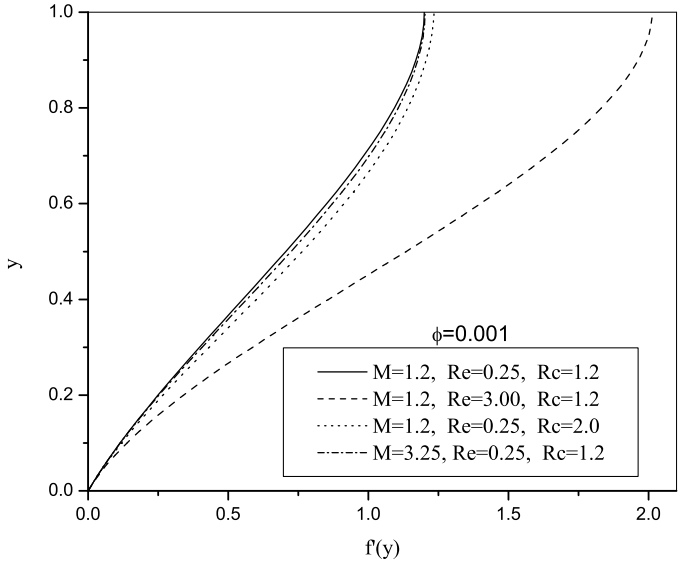

Fig. 11. Variation of $f(y)$ with y for various values of M, Re and Re_c when $\phi = 0.001$.

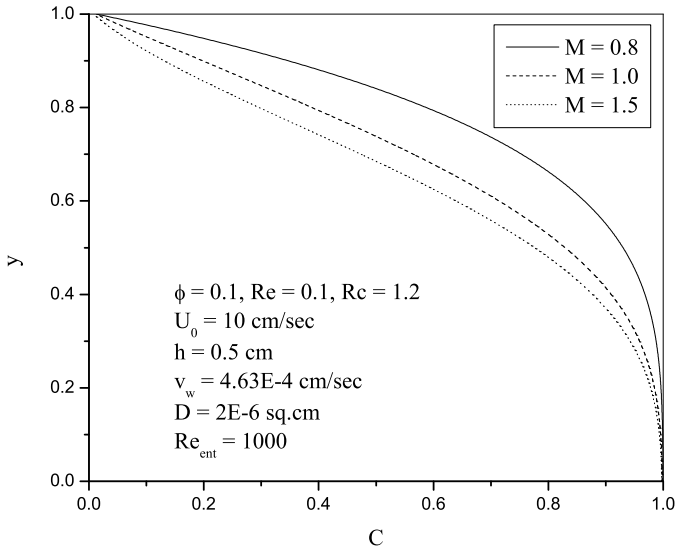

Fig. 12. Variation of concentration distribution with y for different values of Hartmann number M for $x = 0.002$.

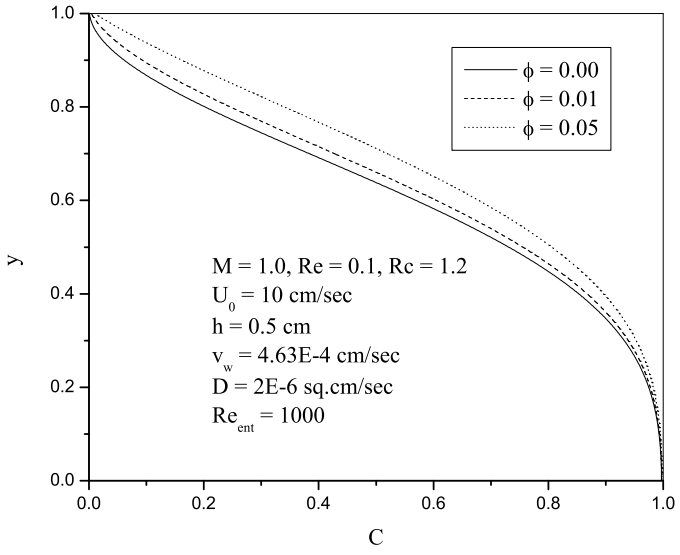

Fig. 13. Variation of concentration distribution with y for different values of porous parameter ϕ for $x = 0.002$.

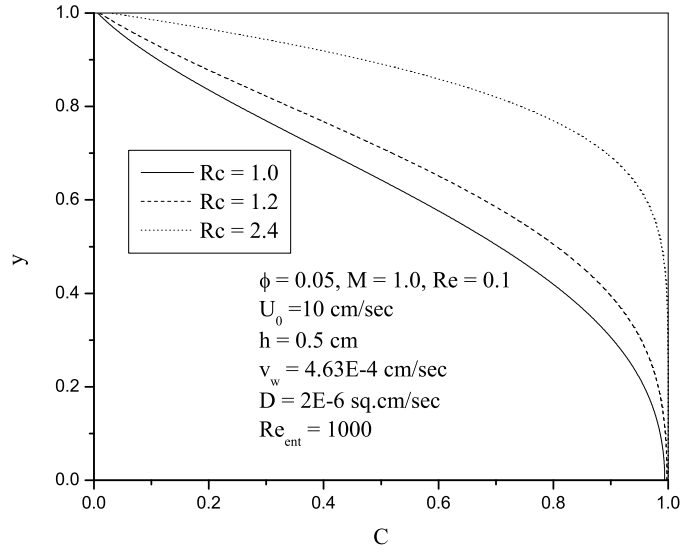

Fig. 14. Variation of concentration distribution with y for different values of Re_c for $x = 0.002$.

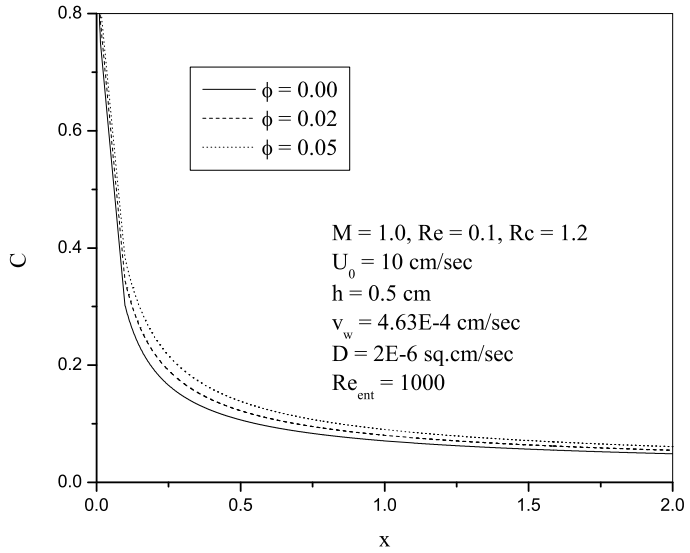

Fig. 15. Variation of concentration distribution with dimensionless horizontal distance x for different values of porous parameter ϕ for $y = 2$.

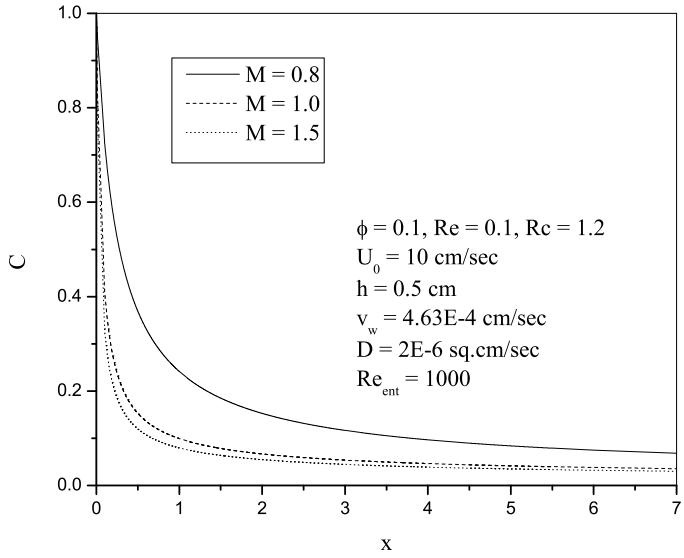

Fig. 16. Variation of concentration distribution with dimensionless horizontal distance x for different values of Hartmann number M for $y = 2$.

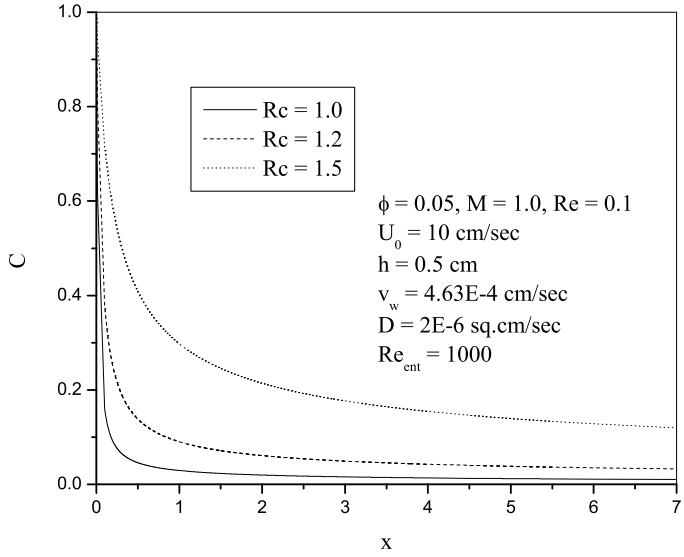

Fig. 17. Variation of concentration distribution with dimensionless horizontal distance x for different values of Re_c for $y = 2$.

Table 1.
The values of skin friction coefficient at the stretching sheet and porous plate when $x = 2.0$

ϕ	M	Re	Re_c	$(C_f)_0$	$(C_f)_1$
0.0	1	0.25	1	$0.1615920 \cdot 10^2$	$-0.3253400 \cdot 10^2$
	1	0.25	3	$0.1202659 \cdot 10^3$	$-0.1224411 \cdot 10^3$
	1	0.50	1	$0.8288509 \cdot 10^1$	$-0.1600749 \cdot 10^2$
	3	0.25	1	$0.1447954 \cdot 10^2$	$-0.4004126 \cdot 10^2$
0.5	1	0.25	1	$0.7243129 \cdot 10^1$	$-0.5437709 \cdot 10^1$
	1	0.25	3	$0.1838811 \cdot 10^3$	$0.2513435 \cdot 10^3$
	1	0.50	1	$0.4675885 \cdot 10^1$	$-0.4713058 \cdot 10^{-1}$
	3	0.25	1	$0.4111741 \cdot 10^1$	$-0.1144079 \cdot 10^2$
1.0	1	0.25	1	$0.4182364 \cdot 10^1$	$-0.3656477 \cdot 10^1$
	1	0.25	3	$0.1551348 \cdot 10^3$	$0.2132638 \cdot 10^3$
	1	0.50	1	$0.2648602 \cdot 10^1$	$-0.4359565 \cdot 10^0$
	3	0.25	1	$0.2395215 \cdot 10^1$	$-0.6671242 \cdot 10^1$
2.0	1	0.25	1	$0.2226558 \cdot 10^1$	$-0.2275541 \cdot 10^1$
	1	0.25	3	$0.1335308 \cdot 10^3$	$0.1811183 \cdot 10^3$
	1	0.50	1	$0.1376890 \cdot 10^1$	$-0.4914478 \cdot 10^0$
	3	0.25	1	$0.1305270 \cdot 10^1$	$-0.3637773 \cdot 10^1$
5.0	1	0.25	1	$0.9171192 \cdot 10^0$	$-0.1070040 \cdot 10^1$
	1	0.25	3	$0.1176574 \cdot 10^3$	$0.1568785 \cdot 10^3$
	1	0.50	1	$0.5537134 \cdot 10^0$	$-0.3069777 \cdot 10^0$
	3	0.25	1	$0.5518624 \cdot 10^0$	$-0.1538701 \cdot 10^1$

values of cross-flow Reynolds number Re_c. It is observed that concentration increases with Re_c along the channel.

The results for skin friction coefficient for various values of physical parameter are tabulated in Table 1. It is noted from this Table that skin friction coefficient $(C_f)_0$ at the stretching plate increases with the increase of cross-flow Reynolds number Re_c, while it decreases with the increase of stretching Reynolds number Re and Hartmann number M. It is interesting to note that skin friction coefficient $(C_f)_1$ at the porous plate decreases with the increases of cross-flow Reynolds number Re_c and Hartmann number M, while it increases with increase in the stretching Reynolds number Re. It is also noted from the table that skin friction coefficient $(C_f)_0$ at the stretching plate and skin friction coefficient $(C_f)_1$ at the porous plate both decreases with increase in the porous parameter ϕ.

Conclusion

Mathematical analysis has been performed to study the influence of uniform magnetic field applied vertically in a Newtonian fluid flow over an acceleration stretching sheet bounded above by a porous medium and flow is subjected to blowing through porous boundary. Analytical solution of the governing boundary layer partial differential equations, which are highly non-linear and in coupled form, have been obtained by perturbation method. Numerical solution is obtained using finite-difference method with Thomas algorithm for dimensionless concentration distribution ϕ. The specific conclusions derived from this study can be listed as follows.

- The effect of magnetic parameter M is to decrease horizontal velocity near the stretching sheet whereas is it increases closer to the porous wall.
- The effect of porous permeability parameter is to decrease horizontal as well as vertical velocities throughout the channel but its effect is more significantly seen near the porous wall.
- The effect of cross-flow Reynolds number is to decrease the horizontal as well as transverse velocities in the channel but more effecting closer to the porous boundary.
- The effect of stretching sheet Reynolds number is to increase both horizontal and vertical velocities in the channel its effect is more prominently seen away from the stretching wall when porous permeability $\phi = 0.2$.
- The effect of transverse uniform magnetic field is to decrease concentration in flow field in y-direction within the channel where as reverse trend is seen by increasing the value of porous permeability parameter ϕ and cross-flow Reynolds number Re_c.
- There is significant enhancement in the value of concentration distribution along the channel (x-direction) by increasing the value of porous parameter ϕ and Re_c at $y = 2$.
- There is significant reduction in the value of concentration due to increasing the transverse uniform magnetic field.

Acknowledgement

One of the authors (Dulal Pal) wishes to thank the University Grants Commission, New Delhi, India for financial support to enable conducting this research work under UGC-SAP (DRS-Phase-I), Grant No. F.510/8/DRS/2004(SAP-I).

REFERENCES

1. Sakiadis, B. C., Boundary-Layer Behavior on Continuous Solid Surface. I. Boundary-Layer Equations for Two-Dimensional and Axisymmetric Flow, *AIChE J.*, 1961, **7**, pp. 26–28.
2. Crane, L. J., Flow Past a Stretching Plate, *ZAMP*, 1970, **21**, pp. 645–647.
3. Banks, W. H. H., Similarity Solutions of the Boundary-Layer Equations for a Stretching Wall, *J. Mech. Theor. Appl.*, 1983, **2**, pp. 375–392.
4. Banks, W. H. H. and Zaturska, M. B., Eigen Solutions in Boundary Layer Flow Adjacent to a Stretching Wall, *IMA J. Appl. Math.*, 1986, **36**, pp. 263–273.
5. Grubka, L. J. and Bobba, K. M., Heat Transfer Characteristics of a Continuous Stretching Surface with Variable Temperature, *ASME J. Heat Transfer*, 1985, **107**, pp. 248–250.
6. Ali, M. E., Heat Transfer Characteristics of a Continuous Stretching Surface, *Wärme Stoffübertrag*, 1994, **29**, pp. 227–234.
7. Areil, P. D., Generalized Three-Dimensional Flow Due to a Stretching Sheet, *ZAMM*, 2003, **83**, pp. 844–852.
8. Erickson, L. E., Fan, L. T., and Fox, V. G., Heat and Mass Transfer on a Moving Continuous Flat Plate with Suction or Injection, *Ind. Eng. Chem.*, 1966, **5**, pp. 19–25.
9. Gupta, P. S. and Gupta, A. S., Heat and Mass Transfer on a Stretching Sheet with Suction or Blowing, *Can. J. Chem. Eng.*, 1977, **55**, pp. 744–746.
10. Chen, C. K. and Char, M. I., Heat and Mass Transfer of a Continuous Stretching Surface with Suction or Blowing, *J. Math. Anal. Appl.*, 1988, **135**, pp. 568–580.

11. Chaudhary, M.A., Merkin, J. H., and Pop, I., Similarity Solutions in the Free Convection Boundary-Layer Flows Adjacent to Vertical Permeable Surface in Porous Media, *Eur. J. Mech. B: Fluids*, 1995, **14**, pp. 217–237.
12. Elbashbeshy, E. M. A., Heat Transfer Over a Stretching Surface with Variable Surface Heat Flux, *J. Phys. D: Appl. Phys.*, 1998, **31**, pp. 1951–1955.
13. Magyari, E. and Keller, B., Exact Solutions for Self-Similar Boundary Layer Flows Induced by Permeable Stretching Wall, *Eur. J. Mech. B: Fluids*, 2000, **19**, pp. 109–122.
14. Hartmann, J. and Lazarus, F., Experimental Investigations on the Flow of Mercury in an Homogeneous Magnetic Field, *Kgl. Danske Videnskab. Selskab Mat. Phys. Medd.*, 1937, **15**, No. 7, pp. 1–45.
15. Borkakoti, A. K. and Bharali, A., Hydromagnetic Flow and Heat. Transfer Between Two Horizontal Plates, the Lower Plate Being a Stretching Sheet, *Quart. Appl. Math.*, 1983, **41**, pp. 461–467.
16. Banerjee, B., Magnetohydrodynamic Flow Between Two Horizontal Plates in a Rotating System, the Lower Plate Being a Stretched Sheet, *Trans. ASME. J. Appl. Mech.*, 1983, **50**, pp. 470–471.
17. Vajravelu, B. and Kumar, B. V. R., Analytical and Numerical Solutions of a Coupled Non-Linear System Arising in a Three-Dimensional Rotating Flow, *Int. J. Non-Linear Mech.*, 2004, **39**, pp. 13–24.
18. Berman, A. S., Laminar Flow in Channels with Porous Walls, *J. Appl. Phys.*, 1953, **524**, pp. 1232–1235.
19. Beavers, G. S. and Joseph, D. D., Boundary Conditions at a Naturally Permeable Walls, *J. Fluid Mech.*, 1967, **30**, pp. 197–207.
20. Blythe, P. A. and Simpkins, P. G., Convection in a Porous Layer for a Temperature Dependent Viscosity, *Int. J. Heat Mass Transfer*, 1981, **24**, pp. 497–506.
21. Richardson, S., A Model for the Boundary Condition of Porous Material, Part II, *J. Fluid Mech.*, 1971, **49**, pp. 327–336.
22. Saffman, P. G., On the Boundary Conditions at the Surface of a Porous Medium, *Stud. Appl. Math.*, 1971, **50**, pp. 93–101.
23. Roa, I. J. and Rajagopal, K. R., The Effect of Slip Boundary Conditions on the Flow of Fluids in a Channel, *Acta Mech.*, 1999, **135**, pp. 113–126.
24. Singh, R. and Laurence, R. L., Influence of Slip Velocity at a Membrane Surface on Ultrafiltration Performance – I. Channel Flow System, *Int. J. Heat Mass Transfer*, 1979, **12**, pp. 721–729.
25. Rudraiah, N. and Musuoka, T., Asymptotic Analysis of Natural Convection Through Horizontal Porous Layer, *Int. J. Eng. Sci.*, 1982, **20**, pp. 27–39.
26. Rudraiah, N., Dulal Pal, and Shivakumara, P. N., Effects of Slip and Magnetic Field on Composite System, *Fluid Dyn. Res.*, 1988, **4**, pp. 255–270.
27. Sutton, G. W. and Sherman, A., *Engineering Magnetohydrodynamics*, McGraw-Hill, New York, 1965.
28. Chakraborty, A. and Gupta, A. S., Hydromagnetic Flow and Heat Transfer Over a Stretching Sheet, *Quart. Appl. Math.*, 1979, **37**, pp. 73–78.

Appendix

$$R_1 = \frac{A_0^2}{\mathrm{M}^4} - 4c_2c_3\mathrm{M}^2, \qquad R_2 = \frac{2c_2A_0}{\mathrm{M}} + c_1c_2\mathrm{M}^2, \qquad R_3 = c_2A_0,$$

$$R_4 = \frac{2c_3A_0}{\mathrm{M}} - c_1c_3\mathrm{M}^2, \qquad R_5 = c_3A_0,$$

$$A_0 = (c_2\mathrm{M} - c_3\mathrm{M} - 1)\mathrm{M}^2,$$

$$B = 2\mathrm{M}e^{-\mathrm{M}} + \mathrm{M}^2e^{-\mathrm{M}} - 4\mathrm{M} + 2\mathrm{M}e^{\mathrm{M}} - \mathrm{M}^2e^{\mathrm{M}},$$

$$B_1 = -\phi(\mathrm{M}^3e^{\mathrm{M}} + \mathrm{M}^2e^{-\mathrm{M}} + \mathrm{M}^3e^{-\mathrm{M}} - \mathrm{M}^2e^{\mathrm{M}}),$$

$$c_1 = -(c_2 + c_3), \qquad c_2 = \frac{c_{21} + c_{22} + c_{23}}{B + B_1}, \qquad c_3 = \frac{c_{31} - c_{32} + c_{33}}{B + B_1},$$

$$c_4 = -(c_5 + c_6), \qquad c_5 = \frac{c_{51} + c_{52} - c_{53} + c_{54}}{B + B_1}, \qquad c_6 = \frac{c_{61} + c_{62} + c_{63} + c_{64}}{B + B_1},$$

$$c_{21} = \mathrm{Re}_c(\mathrm{M} - \mathrm{M}e^{-\mathrm{M}}), \qquad c_{22} = e^{-\mathrm{M}} - \mathrm{M}e^{-\mathrm{M}} - 1, \qquad c_{23} = \phi\mathrm{M}^2e^{-\mathrm{M}}(\mathrm{Re}_c - 1),$$

$$c_{31} = \mathrm{Re}_c(\mathrm{M} - \mathrm{M}e^{\mathrm{M}}), \qquad c_{32} = \mathrm{M} - \mathrm{M}e^{\mathrm{M}} - 1, \qquad c_{33} = -\phi\mathrm{M}^2e^{\mathrm{M}}(\mathrm{Re}_c - 1),$$

$$c_{51} = c_{511} + c_{512}, \qquad c_{52} = c_{521} + c_{522}, \qquad c_{53} = c_{531} + c_{532}, \qquad c_{54} = c_{541} + c_{542},$$

$$c_{61} = c_{611} + c_{612}, \qquad c_{62} = c_{621} + c_{622}, \qquad c_{63} = c_{631} + c_{632}, \qquad c_{64} = c_{641} + c_{642},$$

$$c_{511} = \frac{R_2}{2\mathrm{M}^2}\left(e^{-\mathrm{M}} + \mathrm{M}e^{-\mathrm{M}} - \mathrm{M}^2e^{\mathrm{M}} + \mathrm{M}e^{\mathrm{M}} + e^{\mathrm{M}} - 2\mathrm{M} - 2\right),$$

$$c_{512} = -\frac{\phi R_2}{2\mathrm{M}^2}\left(2\mathrm{M} + \mathrm{M}^2e^{-\mathrm{M}} - 2\mathrm{M}e^{\mathrm{M}} + \mathrm{M}^2e^{\mathrm{M}} + \mathrm{M}^3e^{\mathrm{M}}\right),$$

$$c_{521} = \frac{R_3}{4\mathrm{M}^3}\left(\mathrm{M}e^{\mathrm{M}} + 3\mathrm{M}e^{-\mathrm{M}} - 3\mathrm{M}^2e^{\mathrm{M}} + \mathrm{M}^3e^{\mathrm{M}} + 3e^{\mathrm{M}} + 3e^{-\mathrm{M}} + 2\mathrm{M}^2 - 4\mathrm{M} - 6\right),$$

$$c_{522} = -\frac{\phi R_3}{4\mathrm{M}^3}\left(4\mathrm{M} - 4\mathrm{M}^2 + 3\mathrm{M}^2e^{-\mathrm{M}} - 4\mathrm{M}e^{\mathrm{M}} + 5\mathrm{M}^2e^{\mathrm{M}} - \mathrm{M}^4e^{\mathrm{M}}\right),$$

$$c_{531} = \frac{R_4}{2\mathrm{M}^2}\left(\mathrm{M}^2e^{-\mathrm{M}} + 2e^{-\mathrm{M}} - 2e^{-2\mathrm{M}} - 1\right),$$

$$c_{532} = \frac{\phi R_4}{2\mathrm{M}^2}\left(2\mathrm{M}^2e^{-\mathrm{M}} - \mathrm{M}^3e^{-\mathrm{M}} + 2\mathrm{M}e^{-2\mathrm{M}} - 2\mathrm{M}e^{-\mathrm{M}}\right),$$

$$c_{541} = \frac{R_5}{4\mathrm{M}^3}\left(2\mathrm{M}e^{-2\mathrm{M}} - 2\mathrm{M}e^{-\mathrm{M}} - \mathrm{M}^2e^{-\mathrm{M}} - \mathrm{M}^3e^{-\mathrm{M}} - 6e^{-\mathrm{M}} + 3e^{-2\mathrm{M}} + 3\right),$$

$$c_{542} = -\frac{\phi R_5}{4\mathrm{M}^3}\left(2\mathrm{M}^3e^{-\mathrm{M}} + 4\mathrm{M}^2e^{-2\mathrm{M}} - \mathrm{M}^4e^{-\mathrm{M}} - 4\mathrm{M}e^{-2\mathrm{M}} - 4\mathrm{M}e^{-\mathrm{M}}\right),$$

$$c_{611} = \frac{R_2}{2\mathrm{M}^2}\left(\mathrm{M}^2 e^{\mathrm{M}} + 2e^{\mathrm{M}} - e^{2\mathrm{M}} - 1\right),$$

$$c_{612} = \frac{\phi R_2}{2\mathrm{M}^2}\left(2\mathrm{M}^2 e^{\mathrm{M}} + \mathrm{M}^3 e^{\mathrm{M}} - 2\mathrm{M}e^{2\mathrm{M}} + 2\mathrm{M}e^{\mathrm{M}}\right),$$

$$c_{621} = \frac{R_3}{4\mathrm{M}^3}\left(\mathrm{M}^2 e^{\mathrm{M}} - \mathrm{M}^3 e^{\mathrm{M}} + 2\mathrm{M}e^{2\mathrm{M}} - 2\mathrm{M}e^{\mathrm{M}} + 6e^{\mathrm{M}} - 3e^{2\mathrm{M}} - 3\right),$$

$$c_{622} = -\frac{\phi R_3}{4\mathrm{M}^3}\left(2\mathrm{M}^3 e^{\mathrm{M}} + \mathrm{M}^4 e^{\mathrm{M}} + 4\mathrm{M}e^{2\mathrm{M}} - 4\mathrm{M}^2 e^{2\mathrm{M}} - 4\mathrm{M}e^{\mathrm{M}}\right),$$

$$c_{631} = \frac{R_4}{2\mathrm{M}^2}\left(\mathrm{M}^2 e^{-\mathrm{M}} - e^{\mathrm{M}} + \mathrm{M}e^{\mathrm{M}} - 2\mathrm{M} - e^{-\mathrm{M}} + \mathrm{M}e^{-\mathrm{M}} + 2\right),$$

$$c_{632} = \frac{\phi R_4}{2\mathrm{M}^2}\left(\mathrm{M}^2 e^{-\mathrm{M}} - \mathrm{M}^3 e^{-\mathrm{M}} - 2\mathrm{M} + \mathrm{M}^2 e^{\mathrm{M}} + 2\mathrm{M}e^{-\mathrm{M}}\right),$$

$$c_{641} = \frac{R_5}{4\mathrm{M}^3}\left(\mathrm{M}^2 e^{-\mathrm{M}} + \mathrm{M}^3 e^{-\mathrm{M}} - 4\mathrm{M} - 2\mathrm{M}^2 + \mathrm{M}e^{-\mathrm{M}} + 3\mathrm{M}e^{\mathrm{M}} - 3e^{\mathrm{M}} - 3e^{-\mathrm{M}} + 6\right),$$

$$c_{642} = \frac{\phi R_5}{4\mathrm{M}^3}\left(5\mathrm{M}^2 e^{-\mathrm{M}} - \mathrm{M}^4 e^{-\mathrm{M}} - 4\mathrm{M} - 4\mathrm{M}^2 + 3\mathrm{M}^2 e^{\mathrm{M}} + 4\mathrm{M}e^{-\mathrm{M}}\right),$$

□◆◆◆□

Characterization of Sealing Ring Cavitation in Centrifugal Pumps with Water and Viscous Oil[†]

K. Gangadharan Nair and **T. P. Ashok Babu**

National Institute of Technology Karnataka
Karnataka (St.), India
E-mail: gnkssr@gmail.com

This research paper presents characterization of sealing ring cavitation in centrifugal pumps with water and viscous oil. The paper discusses development of theoretical formulation for sealing ring cavitation and simulation using software model along with experimental validation. The pump performance test results and its standard clearance for the sealing ring are used to simulate the theoretical model. The study is extended for pumps with SAE-30 lubricating oil. The simulation results present the variation of downstream pressure with different sealing ring dimensions in pumps. The value of downstream pressure determines the possibility of occurrence of cavitation at the clearance. The theoretical formulation developed is validated by using a venturi cavitation test set up. Clearances equivalent to various sealing ring dimensions are made at the test section using different hemispherical models. Theoretical formulation for downstream pressure at the clearance of venturi test section is derived using the test set up details and pump specification. The clearance cavitation coefficients as per K. K. Shelneves equation are obtained from theory as well as from experimentation and compared. The phenomena of cavitation damages the sealing ring which results a fall in performance of the pump. However this research work lead to the prediction of sealing ring cavitation in centrifugal pumps handling water and oil enabling the replacement of sealing ring before affecting cavitation damage.

* * *

Nomenclature

B	radial clearance $[\mathrm{m}]$;
C	average velocity of fluid in the clearance $[\mathrm{m/s}]$;
C_r	peripheral velocity at the sealing ring $[\mathrm{m/s}]$;
C_1	peripheral velocity at the inlet of the impeller $[\mathrm{m}]$;

[†]Received 07.01.2009

ISSN 1064-2277
© 2010 Begell House, Inc.

C_2 peripheral velocity at the outlet of the impeller [m];
D diameter of impeller at inlet [m];
d_1 leakage joint diameter [m];
d_2 diameter of impeller at outlet [m];
D_s diameter of suction pipe [m];
f friction factor for pipe from Blasius relation [dimensionless];
H total head of the pump [m];
K volute design constant [dimensionless];
K_{c1} clearance cavitation coefficient from venturi cavitation test set up;
K_{c2} clearance cavitation coefficient from sealing ring of a $5\ \mathrm{hp}$ pump;
L length of clearance [m];
l_{es} equivalent length of suction pipe [m];
N speed of the pump [rpm];
P pressure [$\mathrm{N/m^2}$];
P_{us} upstream pressure of clearance [$\mathrm{N/m^2}$];
P_{ts} pressure at the test section [$\mathrm{N/m^2}$];
P_1/γ downstream pressure of clearance [m of fluid];
P_2/γ upstream pressure of clearance [m of fluid];
P_v/γ vapour pressure of fluid [m of fluid];
P_a/γ atmospheric pressure [m of fluid];
Q discharge of the pump [$\mathrm{m^3/s}$];
Q^1 sum total of discharge and leakage discharge [$\mathrm{m^3/s}$];
Q_L leakage flow through clearance [$\mathrm{m^3/s}$];
Q_{LC} critical leakage flow through clearance [$\mathrm{m^3/s}$];
x_d static level of delivery gauge from datum.

Greek Symbols

η_v volumetric efficiency of the pump [$\%$];
γ specific weight of the fluid [$\mathrm{N/m^3}$];
λ friction factor for clearance [dimensionless].

Introduction

The phenomena of formation of vapour bubbles in a fluid due to low pressure, their growth, movement and collapse is called as cavitation.In the case of centrifugal pumps, a small clearance exists between impeller and casing. The leakage through this joint is controlled by the sealing ring. If the pressure at the clearance reaches vapour pressure of fluid, cavitation will occur called sealing ring cavitaton. Sealing rings are essential to prevent leakage, but the clearance provided at the sealing ring should be in such a way that it is free from cavitation. The ring wears and radial clearance increases after certain years of operation. The photographic method enables the measurement of radial clearance at the sealing ring. This research is for the prediction of sealing ring cavitation in centrifugal pumps. For this, the volumetric efficiency range is obtained from the pump manufacturer's catalogue. At the same time vapour pressure of fluid varies with the temperature, and in this work temperature variation is not considered, which one limitation of using this approach is. However in pumps working at normal conditions, temperature variation will be negligible for fluids other than cryogenic fluids. In this work, pumps with water and SAE-30 oil are

assumed to operate at normal temperatures.

Present work mainly analyzed the clearance cavitaton for various design and operating conditions of the pump. As per Knapp [1], sealing ring cavitation is of vortex-core type. Satoshi Watanabe and Tatsuya Hidaka [2] analyzed thermodynamic effects on cavitation instabilities. Thermodynamic effects are not considered in this work because the objective is to model and simulate the cavitation in a clearance. Ruggeri R. S. and Moore R. D. [3] developed method for prediction of pump cavitation with performance for various fluids at various temperatures and speeds. They mainly studied the impeller cavitation and this work is specific to sealing ring cavitation. Kumaraswamy [4] studied cavitation in pumps considering noise as parameter. He studied mainly at the impeller due to insufficient NPSH, but not at the sealing ring.

Many studies [5–22] have been done on impeller cavitation with its various aspects, but a little work is concentrated at the clearance space at the sealing ring. Gangadharan Nair K. [13] conducted correlation studies between cavitation in a clearance and cavitation noise related to the sealing ring of a radial flow pump. The prediction of clearance cavitation in centrifugal pumps is of much important but tedious, compared to other types of cavitation. In this work an entirely new method is developed for the prediction and analysis of sealing ring cavitation. A venturi cavitation test set up with proper models at the test section is used for validating the theoretical formulation. Clearance cavitation is generated at the test section and clearance cavitation coefficients are found out for validation of theory.

In the coming sections theoretical formulation, modeling and simulation are discussed. Results between theoretical and experimental values of clearance cavitation coefficients are also discussed for validation. Finally results and conclusion of the work are included.

1. Methodology

Theoretical formulation for sealing ring cavitation is developed for centrifugal pumps handling fluids. Conditions for occurrence of sealing ring cavitation are established theoretically for various sealing ring dimensions with water and SAE-30 oil for various operating conditions. A typical centrifugal pump and its test data and standard clearances are taken for the theoretical simulation analysis. For lubricating oil, viscosity correction factors are applied for head and discharge. The experimental set up and models for the generation of clearance cavitation are designed and fabricated. A venturi test set up with six hemispherical models is used to generate clearance cavitation. The equation for downstream pressure at the venturi test section of the set up is derived and formulated. The experiments are planned with water and SAE-30 oil with various size hemispherical models. But due to practical limitations, experiments are conducted only with water. This is sufficient since, theoretical simulation results follow same trend for water and viscous oil. Hence the trend obtained for clearance cavitation coefficients with water follow in a similar sense for the oil selected. The generated cavitation at the clearance is measured by means of clearance cavitation coefficients and compared that with theoretical value of coefficients.

2. Theoretical Formulation (Developed)

The sealing ring provides an easily and economically removable leakage joint between the impeller and casing. Due to high velocity through the clearance, pressure may reach vapour pressure at that temperature, causing sealing ring cavitation.

Fig. 1 shows the fluid flow in the clearance space in a centrifugal pump between casing and

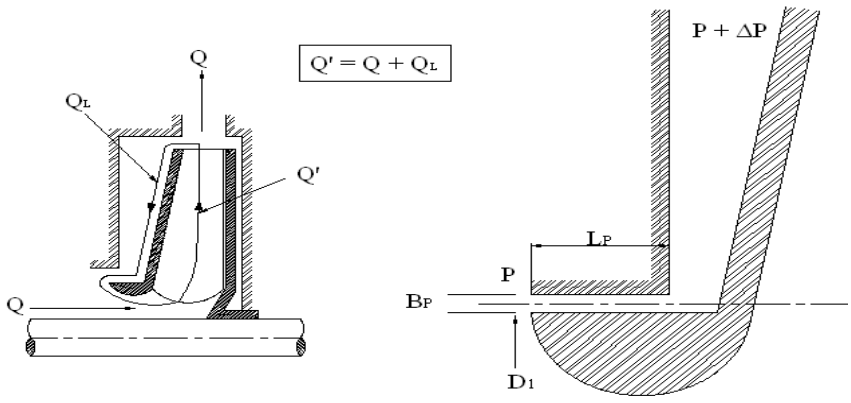

Fig. 1. Fluid flow through clearance.

impeller [19]. Due to a pressure difference of ΔP across the clearance, a leakage flow equal to Q_L occurs towards the eye of the impeller. Due to losses occurring in the clearance, the static pressure of fluid reduces, sometimes reaches the vapour pressure of the fluid, leading to clearance cavitation at or near the downstream side of the clearance. In this work, the following theoretical formulations are developed for critical leakage flow and downstream pressure at the clearance of sealing ring from the fundamentals of fluid flow and cavitation theory.

The head necessary to produce a flow through the slot with an average velocity, C is

$$h_1 = \frac{C^2}{2g}\,. \tag{1a}$$

Head loss for the sharp-edged entry to the slot is

$$h_2 = \frac{C^2}{4g}\,. \tag{1b}$$

Head loss in flow through a slot of width B and length L is given by

$$h_3 = \frac{\lambda L C^2}{d_h 2g}\,, \tag{1c}$$

where λ is friction factor for the clearance. In the case of an annular slot as shown in Fig. 1, the hydraulic diameter d_h will be approximately equal to half of the radial clearance [13]. The total head loss at the clearance is derived and given as

$$\Delta h = \left[1.5 + \frac{2\lambda L}{B}\right]\frac{C^2}{2g}\,. \tag{2}$$

The mean velocity through the slot is given by

$$C = \sqrt{\frac{2g\Delta h}{1.5 + 2\lambda\dfrac{L}{B}}}\,. \tag{3a}$$

The mean velocity through the slot is also equal to

$$C = C_D\sqrt{2g\Delta h}\,. \tag{3b}$$

Comparing the values of C from Eqs. (3a) and (3b) the flow coefficient is given by

$$C_D = \frac{1}{\sqrt{1.5 + 2\lambda\frac{L}{B}}}.$$

Leakage flow is

$$Q_L = AC_D\sqrt{2g\Delta h}. \tag{4}$$

If volumetric efficiency of the pump, η_v is known at the operating point, leakage flow, Q_L can be found using the equation

$$\eta_v = \frac{Q}{Q + Q_L}. \tag{5}$$

Due to the leakage flow through the clearance, the pressure at the downstream end of the slot may be calculated as

$$\frac{P_1}{\gamma} = \frac{P_2}{\gamma} - \Delta h. \tag{6}$$

Hence, the velocity of fluid flowing through the clearance is

$$C = \sqrt{\frac{2g\left(\frac{P_2}{\gamma} - \frac{P_1}{\gamma}\right)}{1.5 + 2\lambda\frac{L}{B}}}. \tag{7}$$

When the downstream pressure is equal to vapour pressure, critical velocity C_c may be calculated as,

$$C_c = \sqrt{\frac{2g\left(\frac{P_2}{\gamma} - \frac{P_v}{\gamma}\right)}{1.5 + 2\lambda\frac{L}{B}}}. \tag{8a}$$

For this condition leakage flow can be calculated as

$$Q_{LC} = \pi DB\sqrt{\frac{2g\left(\frac{P_2}{\gamma} - \frac{P_v}{\gamma}\right)}{1.5 + 2\lambda\frac{L}{B}}}. \tag{8b}$$

Hence, optimum value of leakage flow, Q_{LC} is computed. For the volumetric efficiency of the pump, the leakage flow Q_L also can be computed. If $Q_L \geq Q_{LC}$, sealing ring cavitation will occur.

As per Stepanoff [15], the pressure at the upstream end of sealing ring is given by

$$\frac{P_2}{\gamma} = H_d(1 - K^2) - \frac{C_2^2 - C_r^2}{8g}. \tag{9}$$

The total head for a pump is given by the sum of pressure head, dynamic head and datum head. For the same diameter of suction and delivery pipes dynamic head difference will be zero. Using these guidelines the value of H_d is derived.

As per Stephen Lazarkiewicz and Troskolanski [17], H_d is finally derived and simplified as

$$H_d = \frac{P_d}{\gamma} = H + \frac{P_a}{\gamma} - \left(1 + \frac{fl_{es}}{D_s}\right)\frac{8Q^2}{\pi^2 g D_s^4} - x_d. \tag{10}$$

Using above Eqs. (6), (9) and (10), the downstream pressure equation is developed as

$$\frac{P_1}{\gamma} = \left\{ H + \frac{P_a}{\gamma} - \left(1 + \frac{f l_{es}}{D_s}\right) \left| \frac{8Q^2}{\pi^2 g D_s^4} \right| - x_d \right\} (1 - K^2) \\ - \frac{C_2^2 - C_r^2}{8g} - \left(1.5 + \frac{2\lambda L}{B}\right) \left(\frac{Q_L}{\pi D B}\right)^2 \frac{1}{2g} \,. \tag{11}$$

From the performance test conducted on the pump, the best efficiency point (b. e. p.) is determined. The required dimensions of the pump are taken from the manufacturers supply catalogue. Using Eq. (11), the downstream pressure is calculated and compared with the vapour pressure of fluid to check the occurrence of clearance cavitation at that temperature. Clearance dimension is selected based on the design of the impeller of the pump. For the volumetric efficiency of the pump, the effect of change of length of clearance as well as radial clearance on clearance cavitation are analyzed separately at best efficiency point. In the same manner the clearance cavitation is analyzed above and below the best efficiency point also (at off-design points). Eq. (11) is used for developing software model to compute the downstream pressure to predict and analyze sealing ring cavitation for various operating conditions in any centrifugal pump.

3. Modeling for Simulation with Water and Lubricating Oil

A typical centrifugal pump is selected and performance test is conducted. The best efficiency point is obtained as, Head is 5.1 m, Discharge is 0.5 l/s, at a speed of 2880 rpm. The design chart [13] is used to select the radial clearance corresponding to the leakage joint diameter. From the manufacturing limitations the radial clearance is chosen as 0.15 mm.The length of clearance is selected as 6 mm [13]. The data and other parameters obtained from the pump system are given in Table 1.

For lubricating oil, the thermo physical properties are taken in to account for the computation of data and parameters similar to water. Thermo physical properties of SAE-30 oil at 30°C are taken from [20].

The head x discharge characteristic curve equation for the pump with water is fitted as

$$H = 6.011 + 0.875 \cdot 10^3 Q - 53.89 Q^2,$$

where H is in m and Q is in $\mathrm{m}^3/\mathrm{sec}$.

Using the above data, Eqs. (8b) and (11) are simplified as

$$Q_{LC} = 0.5426 B \sqrt{\frac{10.89 + 0.677Q - 4.42 \cdot 10^6 Q^2}{1.5 + 0.02\dfrac{L}{B}}} \,, \tag{12}$$

$$\frac{P_1}{\gamma} = 11.306 + 0.677 \cdot 10^3 Q - 4.422 \cdot 10^6 Q^2 - \left[5.1 + 0.068\frac{L}{B}\right] \left(\frac{1 - \eta_v}{\eta v}\right)^2 \left(\frac{Q}{B}\right)^2 . \tag{13}$$

If the same pump is used for other oils, the viscosity of oil affects the pump performance. Viscosity correction is done by using performance correction factors for oil obtained from performance correction chart [20] as shown in Table 2.

The ranges for length of clearance, radial clearance, discharge and volumetric efficiency for simulation and computation are selected reasonably. Formulation and modeling similar to Eqs. (12) and (13) are done with SAE-30 oil.

Table 1.
Data from the pump system

Sl. No.	1	2	3	4	5	6	7	8	9	10
Data	D_s	l_{es}	x_d	d_2	$D_1 = D$	C_2	$C_r = C_1$	K	f	l
Water	0.0254	0.89	0.28	0.087	0.039	10.41	4.65	0.475	0.018	0.010
Reference, Remarks	[13]	[13]	[13]	catalog	catalog	pipe velocity	clearance velocity	[13]	Blasius relation	Blasius relation

Table 2.
Performance correction factors for the fluids

Fluid performance correction factor	Water	SAE-30	Reference
Head	1	0.90	[20]
Discharge	1	0.80	[20]

4. Simulation Results (C-Program)

Taking standard clearance, the value of critical leakage flow is $0.171\ \mathrm{l/s}$ and leakage flow for volumetric efficiency of $60\ \%$ is $0.333\ \mathrm{l/s}$ at best efficiency point. The downstream pressure is $-27.54\ \mathrm{m}$ of water. At the operating point less than b. e. p. ($5.97\ \mathrm{m}$, $0.2\ \mathrm{l/s}$), critical leakage flow and downstream pressure are given by $0.178\ \mathrm{l/s}$ and $5.17\ \mathrm{m}$ of water respectively. At the operating point greater than b. e. p. ($3.26\ \mathrm{m}$, $0.8\ \mathrm{l/s}$), the critical leakage flow is $0.157\ \mathrm{l/s}$ and downstream pressure is $-88.33\ \mathrm{m}$ of water with a volumetric efficiency of $60\ \%$. The length of clearance is changed from 6 to 4, 8, 10, and $12\ \mathrm{mm}$, keeping radial clearance as constant at $0.15\ \mathrm{mm}$ for three operating points. Similarly radial clearance is changed from 0.15 to 0.125, 0.175, 0.2, and $0.225\ \mathrm{mm}$, keeping length of clearance as constant. Tabulation for downstream pressure and critical leakage flow for various length of clearance is given in Tables 3 (tabulation for radial clearance is not shown here). The variation of downstream pressure and volumetric efficiency with change of length of clearance and radial clearance are given in Fig. 2 and 3 respectively.

The tabulations for downstream pressure with oil is also prepared and given below. The variation of downstream pressure and volumetric efficiency with radial clearance values with SAE-30 oil is shown in Fig. 4.

5. Experimental Validation of Theoretical Formulation

The theoretical formulation for sealing ring cavitation is validated by using a venturi cavitation experimental set up. A schematic representation of test set up is shown in Fig. 5. It consisted of: pump of $3\ \mathrm{kw}/2880\ \mathrm{rpm}/30\ \mathrm{m}/5\ \mathrm{l/s}$; venturi; model; chamber for hydrophone; oil sump; support; support for pump; foot valve; stay rods.

For validation of theory, a comparison is made between the clearance cavitation coefficients obtained from theory and experimentation.

K. K Shelneves [13] equation for clearance cavitation coefficient is given as

$$K_c = \frac{2(P_{us} - P_{ts})}{\rho C^2}\,, \tag{14}$$

where K_{c1} is taken as the clearance cavitation coefficient from theoretical formulation and K_{c2} the coefficient obtained using experimentation.

Theoretical formulation for downstream pressure at the clearance of venturi test section is derived separately (derivation not shown here) using all data of the test set up and pump used. In the case of piping and fittings, equivalent length calculation is adopted. Pump specification is used for getting the upstream pressure of the clearance. The downstream pressure is computed for any operating point of the pump for all above mentioned sealing ring clearances. The test section pressure is approximated using the computed value of downstream pressure from the derived equation and upstream pressure. Downstream pressure at the venturi test section is derived as [13]

$$\frac{P_1}{\gamma} = H + 9.35 - \left[5.164 \cdot 10^{-3}\,\frac{1.5 + 0.036(L/B)}{(d_1 B)^2} + 31144\right] Q^2. \tag{15}$$

With the upstream pressure and test section pressure (computation not shown here), the clearance cavitation coefficient is computed theoretically.

The measurement of pressure at the sealing ring clearance is difficult and complicated. Hence clearances equivalent to sealing ring clearances of various size pumps are made at the test section

Table 3.
Simulation results with change of length of clearance for water

Operating conditions	H	Q	η_v	Q_L	Q_{LC}	P_1/γ	P_v/γ	Clearance cavitations
	M	l/s	%	l/s	l/s	M	m	Yes/No
$L = 4$ mm, $B = 0.15$ mm								
$Q < Q_{bep}$	5.971	0.2	50	0.2	0.188	-1.05	0.42	Y
$Q = Q_{bep}$	5.1	0.5	50	0.5	0.182	-66.12	0.42	Y
$Q > Q_{bep}$	3.262	0.8	50	0.8	0.168	-185.3	0.42	Y
$L = 6$ mm, $B = 0.15$ mm								
$Q < Q_{bep}$	5.971	0.2	60	0.133	0.178	5.17	0.42	N
$Q = Q_{bep}$	5.1	0.5	60	0.333	0.171	-27.54	0.42	Y
$Q > Q_{bep}$	3.262	0.8	60	0.533	0.157	-88.33	0.42	Y
$L = 8$ mm, $B = 0.15$ mm								
$Q < Q_{bep}$	5.971	0.2	70	0.085	0.167	8.56	0.42	N
$Q = Q_{bep}$	5.1	0.5	70	0.342	0.149	-7.24	0.42	Y
$Q > Q_{bep}$	3.262	0.8	70	0.342	0.149	-34.08	0.42	Y
$L = 10$ mm, $B = 0.15$ mm								
$Q < Q_{bep}$	5.971	0.2	80	0.050	0.159	10.21	0.42	N
$Q = Q_{bep}$	5.1	0.5	80	0.125	0.154	3.93	0.42	N
$Q > Q_{bep}$	3.262	0.8	80	0.200	0.142	-8.23	0.42	Y
$L = 12$ mm, $B = 0.15$ mm								
$Q < Q_{bep}$	5.971	0.2	90	0.022	0.152	11.04	0.42	N
$Q = Q_{bep}$	5.1	0.5	90	.0.056	0.147	9.12	0.42	N
$Q > Q_{bep}$	3.262	0.8	90	0.089	0.135	5.38	0.42	N

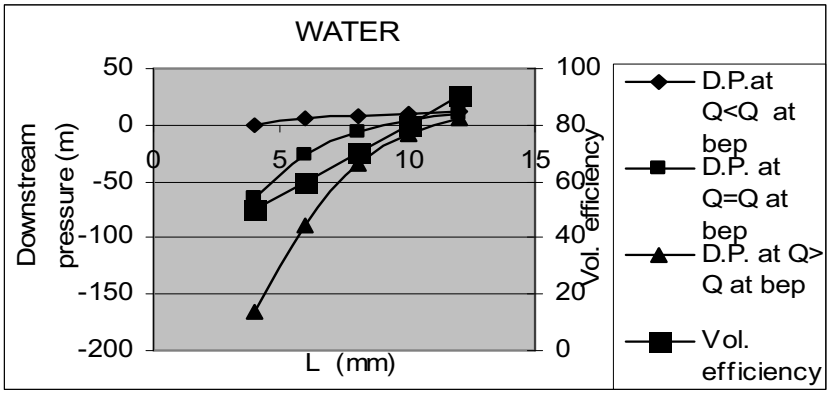

Fig. 2. Influence of length of clearances on sealing ring cavitation with water.

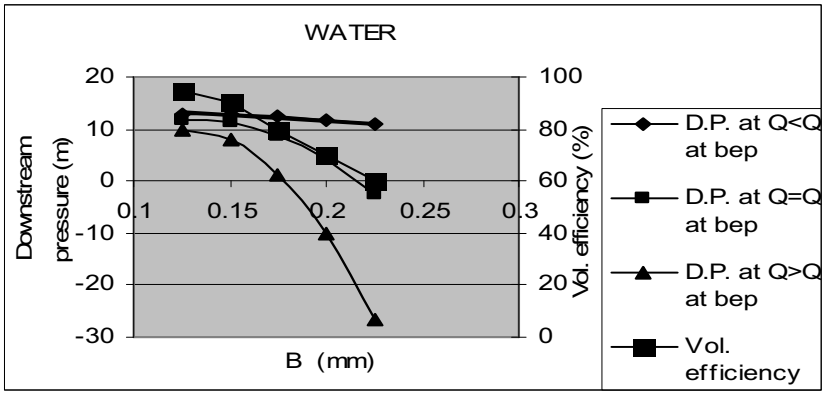

Fig. 3. Influence of radial clearances on sealing ring cavitation with water.

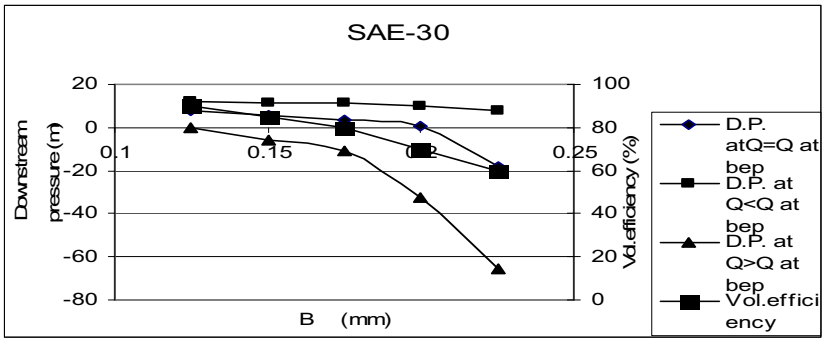

Fig. 4. Influence of radial clearances on sealing ring cavitation with SAE-30 oil.

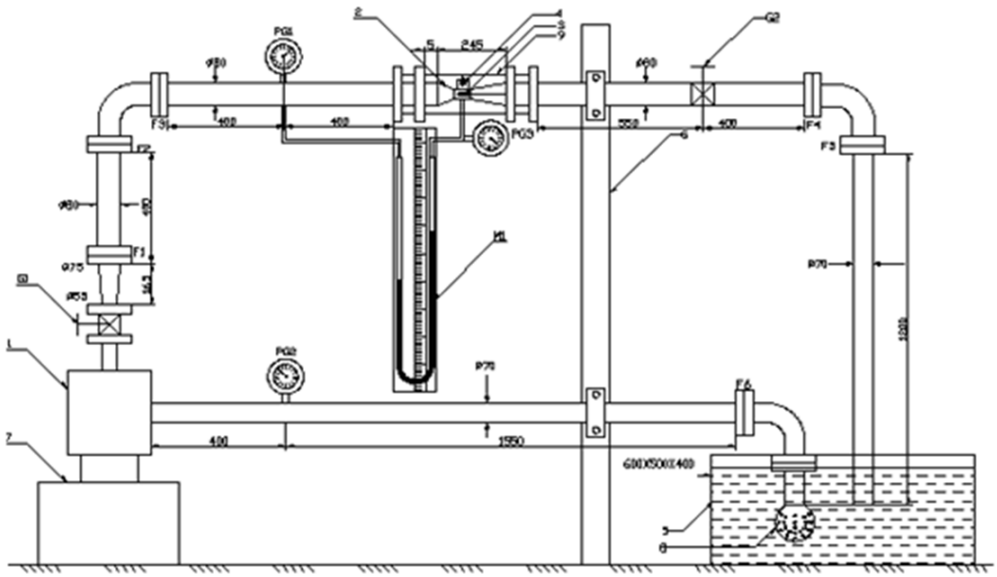

Fig. 5. Experimental set up for clearance cavitation studies
(PG1 is pressure gauge for upstream pressure; PG2 is suction pressure gauge;
PG3 is pressure gauge for test section; M1 is manometer; G1–G2 are gate valves; F1–F6 are flanges).

by the design and assembly of various hemispherical models. The models used at the test section make the clearances of 1.6, 1.8, 2, 2.2, 2.4, and 2.6 mm ($L = 55$ mm) corresponding to various size models. The clearance cavitation is generated at the test section at the concentric clearances and measured using clearance cavitation coefficients (observation not shown here).

The theoretical and experimental values of clearance cavitation coefficients for different discharge values are found, plotted and compared. Such plots for clearance cavitation coefficients K_{c1} and K_{c2} with radial clearance B (mm) are prepared at various discharges 2, 2.5, 3, 3.5, and $4\,\mathrm{l/s}$. The comparison shows that a little deviation, only about an average of $4\ \%$ exist between the two coefficients for theory and experiments.

The variation of K_{c1} and K_{c2} with radial clearance for a discharge of $4\,\mathrm{l/s}$ (constant) is shown in Fig. 6. The results show that similar trend is followed in the case of other discharge values. The simulation results (same trend for all oil) reveal that same kind of validation results are expected with SAE-30 oil as that with water.

6. Results and Discussion

Referring to Fig. 2, the result is that, as the length of clearance is increased the down stream pressure is increased. Referring to Fig. 3, it is found that as the radial clearance is increased, the down stream pressure is decreased. It is also observed that the value of downstream pressure reduces much for discharge higher than that at best efficiency point. The trends obtained for downstream pressure in the case of oil considered here are similar to that obtained with water. This is explained in Fig. 4. The theoretical and experimental values of clearance cavitation coefficients obtained show that the two coefficients have a little deviation, of an average of $4\ \%$ for the same values of clearance velocities as shown in Fig. 6.

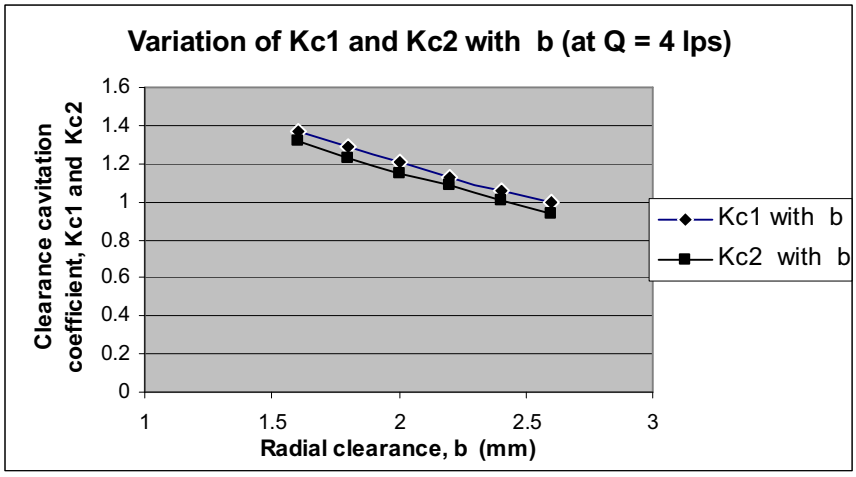

Fig. 6. Variation of clearance cavitation coefficients with radial clearance.

Conclusions

The influence of sealing ring dimensions on sealing ring cavitation is studied. The theoretical modeling is validated with the experimentation results using a venturi cavitation test set up. The following conclusions are made.

1. A method for prediction and analysis of sealing ring cavitation in centrifugal pump is developed.

2. For discharge higher than b. e. p., possibility of occurring sealing ring cavitation is more.

3. If the radial clearance increases, the possibility of occurring sealing ring cavitation is more.

4. If the length of clearance increases, the possibility of occurring sealing ring cavitation is less.

5. The wear of sealing ring lead to increase in radial clearance which will lead to severe sealing ring cavitation.

6. The investigation results lead to the prediction of sealing ring cavitation in centrifugal pumps handling water and oil so that the pump engineer can replace the sealing ring in time without affecting cavitation damage.

Acknowledgements

I express my sincere gratitude to Dr. S. Kumaraswamy, Professor, Hydroturbomachines laboratory, IIT Madras, India for his valuable guidance on the field of cavitation. I also express extreme gratitude to the scientists of Fluid Control Research Institute, Palghat, India for their valuable suggestions for the completion of my work.

REFERENCES

1. Knapp, R. T., Daily, J. W., and Hammitt, F. G., *Cavitation*, McGraw-Hill, New York, 1970, pp. 3–210.
2. Satoshi Watanabe, Tatsuya Hidaka, Hironori Horiguchi, Akinori Furukawa, and Yoshinobu Tsujimoto, Analysis of Thermodynamic Effects on Cavitation Instabilities, In: *ASME J. Fluids Eng.*, 2007, **129**, No. 9, pp. 1123–1130.
3. Ruggeri, R. S. and Moore, R. D., Method for Prediction of Pump Cavitation, Performance for Various Liquids, Liquid Temperatures, Rotative Speeds, *NACA TN*, D-5292, 1969.
4. Kumaraswamy, S., *Cavitaion Studies of Centrifugal Pumps,* Ph. D. Thesis, Hydroturbomachines Laboratory, IIT Madras, 1986, pp. 5–211..
5. Rahmeyer, W. J., Miller, H. L., and Sherikar, Sanjay V., Cavitation Testing Results for a Tortuous Path Control Valve, *ASME FED*, 1995, **210**, pp. 63–67.
6. *Cavitation*, Mechanical Engineering Publications for I. Mech, E., London, 1974, pp. 2–91.
7. Kato, H., Thermodynamic Effect on Incipient and Development of Sheet Cavitation, *ASME FED*, 1984, **16**, pp. 127–136.
8. Tagaya, Y., Kato, H., Yamaguchi, H., and Maeda, M., *Thermodynamic Effect on a Sheet Cavitation*, ASME Pap. No. FEDSM 99-6772, 1999.
9. Horiguchi, H., Watanabe, S., Tsujimoto, Y., and Aoki, M., A Theoretical Analysis of Alternate Blade Cavitation in Inducers, *ASME J. Fluids Eng.*, 2000, **122**, pp. 156–163.
10. Ahuja, V., Hosangadi, A., and Arunajatesan, S., Simulation of Cavitating Flows Using Hybrid Unstructured Meshes, *ASME J. Fluids Eng.*, 2001, **123**, pp. 331–338.
11. Iga, Y., Nonmi, N., Goto, A., Shin, B. R., and Ikohagi, T., Numerical Study of Sheet Cavitation Breakoff Phenomenon on a Cascade Hydrofoil, *ASME J. Fluids Eng.*, 2003, **125**, pp. 643–650.
12. Singhal, A. K., Athavale, M. M., Li, H., and Jiang, Y., Mathematical Basis and Validation of the Full Cavitation Model, *ASME J. Fluids Eng.*, 2002, **124**, pp. 617–624.
13. Gangadharan Nair, K., *Analysis of Sealing Ring Cavitation and Correlation Studies Between Cavitation in a Clearance and Cavitation Noise,* M. Tech. Thesis, Hydroturbomachines Laboratory, IIT Madras, 1997.
14. Karrassik, I. J. et al., *Pump Handbook*, McGraw-Hill, New York, 1976, pp. 4–312.
15. Stepanoff, A. J., *Centrifugal and Axial Flow Pump*, John Wiley & Sons, New York, 1957, pp. 2–285.
16. Scheer, W., *Introduction to Turbo Machines*, IIT Madras, India, 1992, pp. 3–89.
17. Lazarkiewicz, S. and Troskolanski, A. T., *Impeller Pumps*, Pergoman Press, Oxford, 1965, pp. 4–264.
18. Tyler, G., Hicks, P. E., and Edwards, T. W., *Pump Application Engineering*, McGraw-Hill, New York, 1971, pp. 3–206.
19. Balabaskaran, V., Mechanical Design and Construction of Centrifugal Pump, In: *One-Day Workshop at PSG College of Technology*, Coimbatore, India, 1996, pp. 1–98.
20. Gangadharan Nair, K. and Ashok Babu, T. P., Influence of Sealing Ring Dimensions on Clearance Cavitation in a Radial Flow Pump, In: *Int. Conf.*, CIT, Coimbatore, India, 2007.
21. Gangadharan Nair, K. and Ashok Babu, T. P., Improved Grades of Lubricating Oils for the Cavitation-Free Operation of Journal Bearings, In: *Int. Conf.*, GCE, Trissur, India, 2008.
22. Gangadharan Nair, K. and Ashok Babu, T. P., Energy Efficient Centrifugal Pumps on Cavitation Point of View, In: *Nat. Conf. on Energy, Economy and Environment*, NITC, Calicut, India, 2008.

□◆◆◆□

Thermo-Solutal Convection in Water Isopropanol Mixtures in the Presence of Soret Effect[†]

M. A. Rahman and **M. Z. Saghir**

Department of Mechanical and Industrial Engineering, Ryerson University,
Toronto, ON, Canada, M5B 2K3
E-mail: zsaghir@ryerson.ca

In the present study, the onset of thermo-solutal convection in a liquid layer overlaying a porous layer where the system is being laterally heated is investigated. The non-linear two-dimensional Navier – Stokes equations, the energy equation, the mass balance equation and the continuity equation are solved for the liquid layer and the Brinkman model is used for the porous layer. The partial differential equations are solved numerically using the finite element technique. Two different cases are analyzed in this study. In the case of the thermo-solutal convection without thermodiffusion or Soret effect, multi-convective cells appear in the liquid layer and as the thickness of the liquid layer decreases (i. e. higher thickness ratio), the flow covers the entire cavity. In the presence of Soret effect, it has been found that the isopropanol component goes either towards the hot or cold walls depending on the Soret sign.

* * *

Nomenclature

c	mass fraction of the fluid $[-]$;
C	non-dimensional concentration of the fluid;
d	thickness ratio, d_2/L $[-]$;
d_1	liquid layer thickness $[\mathrm{m}]$;
d_2	porous layer thickness $[\mathrm{m}]$;
D_M	solutal diffusion coefficient $[\mathrm{m}^2/\mathrm{s}]$;
D_T	thermal diffusion coefficient $[\mathrm{m}^2/(\mathrm{s\,K})]$;
g	gravitational acceleration $[\mathrm{m}/\mathrm{s}^2]$;
G	non-dimensional overall thermal conductivity;
H	length of the cavity $[\mathrm{m}]$;
k_e	effective thermal conductivity $[\mathrm{W}/(\mathrm{m\,K})]$;
k_f	conductivity of the fluid $[\mathrm{W}/(\mathrm{m\,K})]$;

[†]Received 30.01.2009

ISSN 1064-2277
© 2010 Begell House, Inc.

k_s conductivity of the solid glass beads $[\mathrm{W}/(\mathrm{m\,K})]$;
L height of the cavity $[\mathrm{m}]$;
p pressure $[\mathrm{Pa}]$;
P non-dimensional pressure;
q separation ratio $[-]$;
S_T Soret coefficient, D_T/D_M $[1/\mathrm{K}]$;
t time $[\mathrm{s}]$;
T temperature $[\mathrm{K}]$;
Δc concentration difference $[-]$;
ΔT temperature difference, $(T_H - T_C)$ $[\mathrm{K}]$;
u velocity component in the x-direction $[\mathrm{m/s}]$;
U non-dimensional velocity component in the X-direction
u_o characteristic velocity, $\sqrt{g\beta_T \Delta T L}$ $[\mathrm{m/s}]$;
v velocity component in the y-direction $[\mathrm{m/s}]$;
V non-dimensional velocity component in the Y-direction;
V_t total volume $[\mathrm{m}^3]$;
V_f volume occupied by the fluid $[\mathrm{m}^3]$;
V_s volume occupied by the solid $[\mathrm{m}^3]$.

Non-Dimensional Numbers

Da Darcy number, $\dfrac{\kappa}{L^2}$;

Pr Prandtl number, $\dfrac{\nu}{\alpha}$;

Ra_{LC} solutal Rayleigh number for liquid layer, $\dfrac{g\beta_C \Delta C d_1^3}{\nu\alpha}$;

Ra_{LL} thermal Rayleigh number for liquid layer, $\dfrac{g\beta_T \Delta T d_1^3}{\nu\alpha}$;

Ra_{PC} solutal Rayleigh number for porous layer, $\dfrac{g\beta_C \Delta C d_2 \kappa}{\nu\alpha}$;

Ra_{PL} thermal Rayleigh number for porous layer, $\dfrac{g\beta_T \Delta T d_2 \kappa}{\nu\alpha}$;

Re Reynolds number, $\dfrac{\rho_o u_o L}{\mu}$;

Sc Schmidt number, $\dfrac{\nu}{D_M}$.

Greek Symbols

α thermal diffusivity $[\mathrm{m}^2/\mathrm{s}]$;
α_T thermal diffusion factor, TS_T $[-]$;
β_C solutal expansion $[-]$;
β_T thermal volume expansion $[1/\mathrm{K}]$;
θ non-dimensional temperature, $(T - T_C)/\Delta T$;
κ permeability $[\mathrm{m}^2]$;
τ non-dimensional time;
μ dynamic viscosity $[\mathrm{kg}/(\mathrm{m\,s})]$;
ν kinematic viscosity $[\mathrm{m}^2/\mathrm{s}]$;

ρ_o density of the fluid at reference temperature T_o $[\mathrm{kg/m^3}]$;
ϕ porosity $[-]$.

Subscripts

C cold;
e effective;
f fluid;
H hot;
o reference;
s solid.

Introduction

The thermo-solutal or double-diffusive convection is the heat and species transfer due to the presence of both temperature and concentration gradients. The thermodiffusion effect or the Soret effect is the mass flux in a mixture due to a temperature gradient [1]. This effect is very weak but can be important in the analysis of compositional variation in hydrocarbon reservoirs [2–7].

A liquid layer superimpose a porous layer, with heat and mass transfer taking place through the interface is related to many natural phenomena and various industrial applications [8]. Nield and Bejan [9] collected number of works in the area of convection in porous media. They defined a porous medium as a material consisting of a solid matrix with an interconnected void. The solid matrix is either rigid or undergoes small deformations. The interconnectedness of the void (the pores) allows the flow of one or more fluids through the material. They defined the porosity ϕ, as the fraction of total volume of the medium that is occupied by void space, or the liquid in this present case. So, $(1-\phi)$ is the fraction occupied by the solid beads. Within V_t, let V_f represent the volume occupied by the fluid and V_s represent the volume occupied by the solid, so that $V_t = V_f + V_s$. Then the porosity of the porous medium can be defined as $\phi = V_f/V_t$.

Saghir et al. [10] found that the double diffusive convection plays a major role in the intrusion of the salted water into fresh water and the temperature and salinity induce a strong convection. Benano-Melly et al. [11] modeled a thermo-gravitational experiment in a laterally heated porous medium. They showed that, when solutal and thermal buoyancy forces oppose each other, multiple convection-roll flow patterns develop.

Jiang et al. [12] further studied thermo-gravitational convection for a binary mixture of methane and n-butane in a vertical porous column. Their numerical results revealed that the lighter fluid component migrated to the hot side of the cavity. They explained the convection effect on the thermodiffusion in a hydrocarbon binary system in terms of the characteristic times. When the characteristic time of the convective flow is larger than the characteristic time of the thermodiffusion, the Soret effect is the dominant force for the composition separation in the cavity, and maximum separation is reached when the characteristic time is equal to the time of thermodiffusion. And when the characteristic time is less than the time of thermodiffusion, the buoyancy convection becomes dominant and that corresponds to permeability greater than $10\ \mathrm{md}$.

In the present paper the thermo-solutal convection for the water – isopropanol binary mixtures in the presence of thermodiffusion is investigated. Section 1 presents the governing equation in a non dimensional form. Section 2 shows the numerical procedure followed by Section 3 where the mesh sensitivity is discussed. Section 4 presents the thermodiffusion phenomenon and finally Section 5 highlights the discussion.

1. Governing Equations and Boundary Conditions

The schematic diagram of the model for this study is illustrated in Fig. 1. It represents a two-dimensional square cavity splitted into a liquid layer and a porous layer. The incompressible liquid layer, whose solutal expansion coefficient is β_C and thermal expansion coefficient is β_T, has a height of $d_1 = 0.005$ m and a width of $H = 0.01$ m. The physical properties of the liquid are assumed constant. The liquid layer overlays a homogeneous and rectangular porous layer that is saturated with the same liquid. It is assumed that the liquid and the porous layer are in thermal equilibrium. The porous matrix has a porosity $\phi = 0.39$, which corresponds to a glass bead of diameter 3.25 mm. The Darcy number in this study is $\mathrm{Da} = 10^{-5}$. The porous layer has the same width of H and a height of $d_2 = 0.005$ m. The total thickness is defined by $L = d_1 + d_2$. For the entire analysis, the height of the cavity is set as $L = 0.01$ m. The gravitational acceleration term is set to act in the negative y-direction.

The flow under consideration is assumed laminar and incompressible. The complete continuity, momentum balance, energy balance and mass balance equations are solved simultaneously in order to study the convection patterns. Using the finite element technique, the equations are solved numerically for both the liquid layer and the porous layer of the cavity. The governing equations were rendered dimensionless by using the following non-dimensional groups:

$$\begin{aligned} U &= \frac{u}{u_o}, \qquad V = \frac{v}{u_o}, \qquad X = \frac{x}{L}, \qquad Y = \frac{y}{L}, \qquad P = \frac{pL}{\mu u_0}, \\ \tau &= \frac{tu_o}{L}, \qquad \theta = \frac{T - T_C}{\Delta T}, \qquad C = \frac{c - c_o}{\Delta c}, \qquad L = d_1 + d_2. \end{aligned} \tag{1}$$

Following are the nondimensional governing equations and boundary conditions used for the various cases in this study.

1.1. Liquid layer.

Conservation of mass. The equation of continuity is a partial differential equation which represents the conservation of mass for an infinitesimal control volume. The continuity equation for an incompressible fluid is given by

$$\frac{\partial U}{\partial X} + \frac{\partial V}{\partial Y} = 0. \tag{2}$$

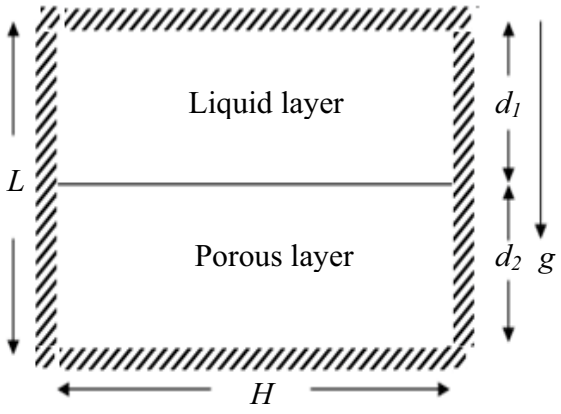

Fig. 1. Geometrical model of the two-dimensional cavity.

Mass transfer equation. If the fluid consists of more than one component, the principle of mass conservation applies to each individual component (or species) in the mixture as well as to the mixture whole. For each component, the principle of mass conservation of species in non-dimensional form is given by

$$\frac{\partial C}{\partial \tau} + U\,\frac{\partial C}{\partial X} + V\,\frac{\partial C}{\partial Y} = \frac{1}{\mathrm{Sc}}\sqrt{\frac{\mathrm{Pr}}{\mathrm{Ra}_{LL}}}\left(1+\frac{d_2}{d_1}\right)^{-3/2} \times\left\{\frac{\partial^2 C}{\partial X^2}+\frac{\partial^2 C}{\partial Y^2}+\alpha_T\left[\frac{\partial^2 \theta}{\partial X^2}+\frac{\partial^2 \theta}{\partial Y^2}\right]\right\}, \tag{3}$$

where τ is the non-dimensional time, Sc is the Schmidt number, Pr is the Prandtl number and Ra_{LL} is the thermal Raleigh number for the liquid layer.

Momentum equation. For the liquid layer, the momentum balance equation is represented by the Navier – Stokes equations. The flow model is Newtonian, incompressible and transient. In the X-direction, the momentum conservation equation is expressed as

$$\mathrm{Re}\left[\frac{\partial U}{\partial \tau}+U\,\frac{\partial U}{\partial X}+V\,\frac{\partial U}{\partial Y}\right] = -\frac{\partial P}{\partial X}+\frac{\partial^2 U}{\partial X^2}+\frac{\partial^2 U}{\partial Y^2}\,. \tag{4}$$

In the Y-direction, the momentum conservation equation is written as

$$\mathrm{Re}\left[\frac{\partial V}{\partial \tau}+U\,\frac{\partial V}{\partial X}+V\,\frac{\partial V}{\partial Y}\right] = -\frac{\partial P}{\partial Y}+\frac{\partial^2 V}{\partial X^2}+\frac{\partial^2 V}{\partial Y^2} -\frac{1}{\mathrm{PrRe}}\left(1+\frac{d_2}{d_1}\right)^3\left[\mathrm{Ra}_{LL}\theta-\mathrm{Ra}_{LC}C\right], \tag{5}$$

where Re is the Reynolds number, Ra_{LL} is the thermal Raleigh number for the liquid layer, Ra_{LC} is the solutal Raleigh number for the liquid layer, θ is the non-dimensional temperature and C is the non-dimensional concentration.

Energy equation. The thermal energy equation for the liquid layer is expressed as

$$\mathrm{Re}\,\mathrm{Pr}\left[\frac{\partial \theta}{\partial \tau}+U\,\frac{\partial \theta}{\partial X}+V\,\frac{\partial \theta}{\partial Y}\right] = \frac{\partial^2 \theta}{\partial X^2}+\frac{\partial^2 \theta}{\partial Y^2}\,. \tag{6}$$

1.2. Porous layer.

Conservation of mass and mass transfer equation. The equation of continuity for the porous layer and the mass transfer equation are the same as for the liquid layer.

Momentum equation. Darcy was the first to formulate the basic equation of flow in porous media based on the proportionality between the flow rate and the applied pressure difference that was revealed from experiment. Conventionally, Darcy's law was used as the momentum balance equation in a porous medium. However, as noted by Desaive et al. [13], it suffers from mathematical inaccuracy due to the inability to impose a no-slip boundary condition. Consequently, in this study, the Brinkman equation is used to represent the momentum equation. In the X-direction, the momentum conservation equation is written as follows,

$$\frac{\mathrm{Re}}{\phi}\,\frac{\partial U}{\partial \tau}+\frac{1}{\mathrm{Da}}\,U = -\frac{\partial P}{\partial X}+\frac{\partial^2 U}{\partial X^2}+\frac{\partial^2 U}{\partial Y^2}\,. \tag{7}$$

In the Y-direction, the momentum conservation equation is represented by

$$\frac{\mathrm{Re}}{\phi}\frac{\partial V}{\partial \tau}+\frac{1}{\mathrm{Da}}V=-\frac{\partial P}{\partial Y}+\frac{\partial^2 V}{\partial X^2}+\frac{\partial^2 V}{\partial Y^2}-\frac{1}{\mathrm{Pr}\,\mathrm{Re}\,\mathrm{Da}}\left(1+\frac{d_2}{d_1}\right)^3\left[\mathrm{Ra}_{PL}\theta-\mathrm{Ra}_{PC}C\right], \quad (8)$$

where ϕ is the porosity, Ra_{PL} is the thermal Rayleigh number for the porous layer and Ra_{PC} is the solutal Rayleigh number for the porous layer.

Energy equation. The thermal energy equation for the porous layer is given by

$$\mathrm{Re}\,\mathrm{Pr}\left[\frac{\partial \theta}{\partial \tau}+U\frac{\partial \theta}{\partial X}+V\frac{\partial \theta}{\partial Y}\right]=G\left[\frac{\partial^2 \theta}{\partial X^2}+\frac{\partial^2 \theta}{\partial Y^2}\right], \quad (9)$$

where

$$G=\frac{k_e}{k_f}=\frac{\phi k_f+(1-\phi)k_s}{k_f}=\phi+(1-\phi)\frac{k_s}{k_f};$$

k_e is the effective thermal conductivity; k_f is conductivity of the fluid; k_s is the conductivity of the solid; G is the ratio between k_e and k_f.

In the above equations, an appropriate relationship between the thermal liquid Rayleigh number and the thermal porous Rayleigh number has been obtained which can be expressed as:

$$\mathrm{Ra}_{PL}=\mathrm{Ra}_{LL}\,\mathrm{Da}\left(1+\frac{d_1}{d_2}\right)^2\frac{d_2}{d_1}. \quad (10)$$

In order to analyze the fluid motion properly, the basic conservation laws have to be applied along with the appropriate boundary conditions on each segment of the boundary. In the present case, the cavity is laterally heated and the left vertical wall is fixed at a cold temperature T_C, while the right vertical wall is maintained at a hot temperature T_H. The top and the bottom surfaces are insulated. The boundary conditions for the four walls of the cavity are presented in Fig. 2. As noted by Kozak et al. [8], at the liquid-porous interface, the continuities of the velocities, the temperature and the mass flux are imposed.

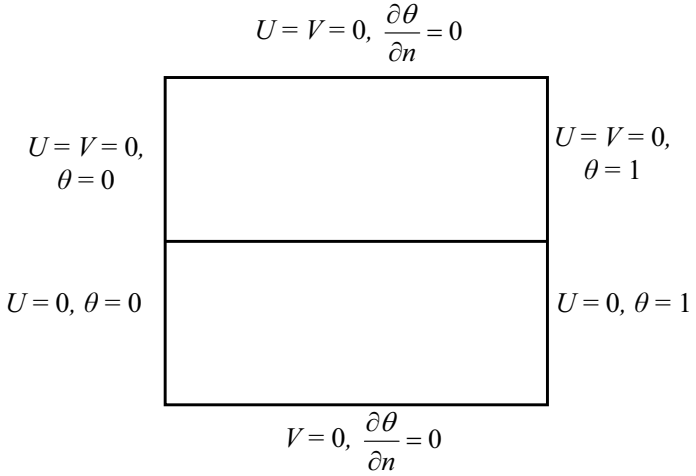

Fig. 2. Lateral heating boundary condition.

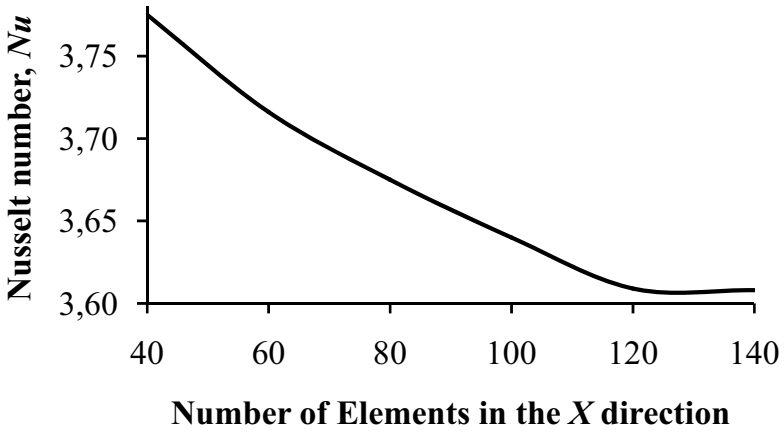

Fig. 3. Calculated Nusselt numbers for mesh sensitivity.

2. Numerical Procedure

The numerical procedure consisted of solving the non-dimensional Eqs. (2) to (9) using the finite element technique [14]. To achieve greater accuracy in the results, a finer mesh was applied to the vertical walls of the square cavity and at the upper surface where the driving force of the flow is located. The five degrees of freedom (velocities, temperature, pressure and species) are unknown and are numerically calculated at each node in the meshed cavity. The convergence criterion for the iterative solution of symmetric and non-symmetric linear equation systems is $1.0 \cdot 10^{-6}$.

3. Mesh Sensitivity Analysis

Since a lateral heating scheme was employed for this study, it was assumed that a high temperature gradient occurs parallel to the upper surface. So, for the mesh sensitivity analysis, the number of elements in the Y-axis was kept constant at 120 and the mesh was varied from 40 to 140 elements in the X-direction in increments of 20. Then the Nusselt number is calculated at the hot and cold wall. The equations are expressed as follows,

$$\mathrm{Nu}_H = \int_0^L \frac{\partial\theta}{\partial Y}\Big|_{X=1} dY, \qquad \mathrm{Nu}_C = \int_0^L \frac{\partial\theta}{\partial Y}\Big|_{X=0} dY. \tag{11}$$

The overall averaged Nusselt number is

$$\mathrm{Nu} = \frac{\mathrm{Nu}_H + \mathrm{Nu}_C}{2}\,. \tag{12}$$

The Nusselt number is compared for the various mesh gradients. The results for the analysis are given in Fig. 3. From this figure one can notice that, when the number of elements in the X-axis is more than 120, the Nusselt number remains unchanged. Thus for the present study a mesh of 120 elements in the X-axis by 120 elements in the Y-axis is selected.

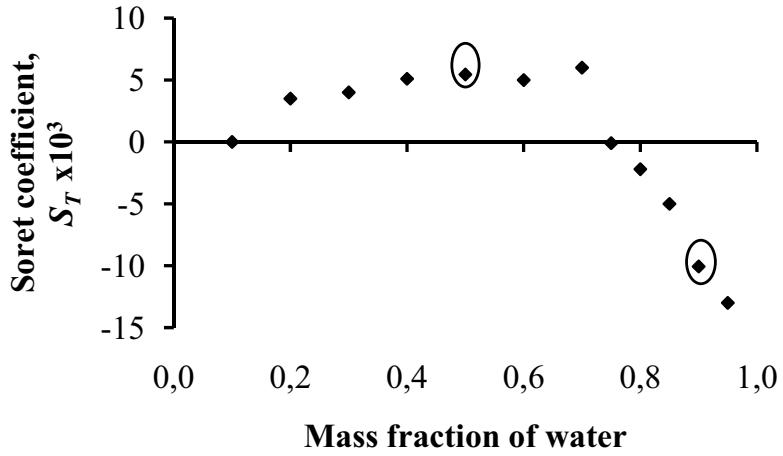

Fig. 4. Dependence of the Soret coefficient on the mass fraction of water in water – isopropanol mixture at 298.15 K [16].

4. Thermodiffusion

The separation of the components of a mixture subjected to a temperature difference is measured by the Soret coefficient $S_T = D_T/D_M$. For the water – isopropanol binary mixture, the sign of the Soret coefficient is strongly dependent on the concentration. Fig. 4 shows the Soret coefficients for the water – isopropanol binary mixtures. From Fig. 4, it can be seen that the Soret coefficient is positive ($S_T > 0$) if the water content is less than 75 %, otherwise the Soret coefficient is negative. So, to analyze the effect of thermodiffusion or the Soret on thermo-solutal convection, two water – isopropanol mixtures having negative and positive Soret coefficient have been chosen. One of the liquid mixtures is 90 % water – 10 % isopropanol and another one is 50 % water – 50 % isopropanol. The physical properties of water – isopropanol mixtures are given in Table 1.

5. Results and Discussion

Two different cases are studied in this paper. In the first case, the thermo-solutal convection is studied separately for two different water – isopropanol mixtures. Then, the thermo-solutal convection with the thermodiffusion or Soret effect is studied.

5.1. Thermo-solutal convection. As noted by Saghir et al. [10], when heat and species transfer exist within a fluid layer, the temperature and concentration gradients create a convection mode. This convection is called thermo-solutal or double diffusive convection. To see the effects of thermo-solutal convection with respect to time, transient condition has been used for this present study. To solve the problems using the finite element method in the transient condition, we used the backward Euler time integration method with a variable time increment option. The first 5 time steps have been kept as fixed with a time step increment $dt = 1.0 \cdot 10^{-6}$ s. After 5 time steps, the calculation switches from the fixed time increment method to the variable time increment method.

Fig. 5 represents the streamlines and isotherms for the time step $t = 975$ s and the thickness ratio $d = 0.50$. Fig. 5a shows the streamlines and isotherms for the case with 90 % water – 10 % isopropanol in the entire cavity. For this case, the calculated thermal Rayleigh number Ra_{LL} is

Table 1.
Physical properties of water – isopropanol
for two different mass fraction compositions

Physical properties		Symbol	90 % water – 10 % isopropanol	50 % water – 50 % isopropanol
Viscosity	$[\mathrm{m}^2/\mathrm{s}]$	ν	$1.41 \cdot 10^{-6}$	$4.18 \cdot 10^{-6}$
Thermal diffusivity	$[\mathrm{m}^2/\mathrm{s}]$	α	$1.30 \cdot 10^{-7}$	$8.50 \cdot 10^{-8}$
Diffusion coefficient	$[\mathrm{m}^2/\mathrm{s}]$	D_M	$8.70 \cdot 10^{-10}$	$1.80 \cdot 10^{-10}$
Density	$[\mathrm{kg}/\mathrm{m}^3]$	ρ	984	905
Soret coefficient	$[1/\mathrm{K}]$	S_T	$-1.06 \cdot 10^{-2}$	$5.45 \cdot 10^{-3}$
Thermal expansion	$[1/\mathrm{K}]$	β_T	$3.10 \cdot 10^{-4}$	$7.70 \cdot 10^{-4}$
Solutal expansion	$[-]$	β_c	0.14	-0.25
Concentration of water	$[-]$	c	0.90	0.50
Pr	$[-]$	ν/α	10.846	49.165
A	$[-]$	Gr/g	1559.278	440.906
Sc	$[-]$	ν/D	1620.690	23216.667
Thermal conductivity	$[\mathrm{W}/(\mathrm{m\,K})]$	k	0.522	0.2866

$1.036 \cdot 10^4$ and solutal Rayleigh number $\mathrm{Ra}_{LC} = 9.36 \cdot 10^5$. As in the present case $\mathrm{Ra}_{LC} > \mathrm{Ra}_{LL}$, multicells appear in the liquid layer. However, the streamlines for the case with 50 % water – 50 % isopropanol, reveal a single cell in the liquid layer. For this case, the calculated thermal Rayleigh number is $\mathrm{Ra}_{LL} = 1.062 \cdot 10^5$ and the solutal Rayleigh number is $\mathrm{Ra}_{LC} = 8.62 \cdot 10^5$. As, the two different Rayleigh numbers are close to each other, only a single cell appears in the liquid layer. For both liquid mixtures, we can also see that the flow in the porous layer is not negligible but too weak as compared to the flow in the liquid layer. It is clearly observed from the isotherms in the porous layer which are slightly distorted from their vertical positions.

Fig. 6 shows the streamlines and isotherms for the liquid mixture of 90 % water – 10 % isopropanol for the thickness ratio $d = 0.90$. Now, the flow dominates the porous layer of the cavity with the cell within the porous layer itself. This phenomenon was predicted by the linear stability analysis of Desaive et al. [13]. If one compares Figs. 5 and 6, it is observed that as the thickness ratio increases, the streamline values decrease since the flow covers the entire cavity.

5.2. Thermodiffusion effect. In the previous section, the thermo-solutal convection was studied. A further study is performed to investigate the convection in the presence of thermodiffusion or the Soret effect. It is known that in the earth gravity condition, the buoyancy effect dominates the convection [15]. So, to investigate the thermodiffusion effect, a microgravity condition ($g = 9.8 \cdot 10^{-7}\ \mathrm{m/s^2}$) is used.

Fig. 7 reflects the isopropanol distribution for different time steps along the horizontal direction of the cavity. From Fig. 7a, we can see that, at the initial time step $t = 0$ s, the concentration of isopropanol is 0.1. But as the time increases, the concentration near the cold wall (at $H = 0$ m) increases and the concentration near the hot wall (at $H = 0.01$ m) decreases. For all the time steps, the concentration varies linearly with distance. Fig. 7b shows the isopropanol distribution for the liquid mixture having 50 % water – 50 % isopropanol. From this figure it can be seen that, at $t = 0$ s, the concentration of isopropanol is 0.5. But as the time increases, the concentration near the cold wall ($H = 0$ m) decreases and the concentration near the hot wall ($H = 0.01$ m) increases. For both liquid mixtures, at the time $t = 500000$ s the isopropanol distribution line appears completely linear.

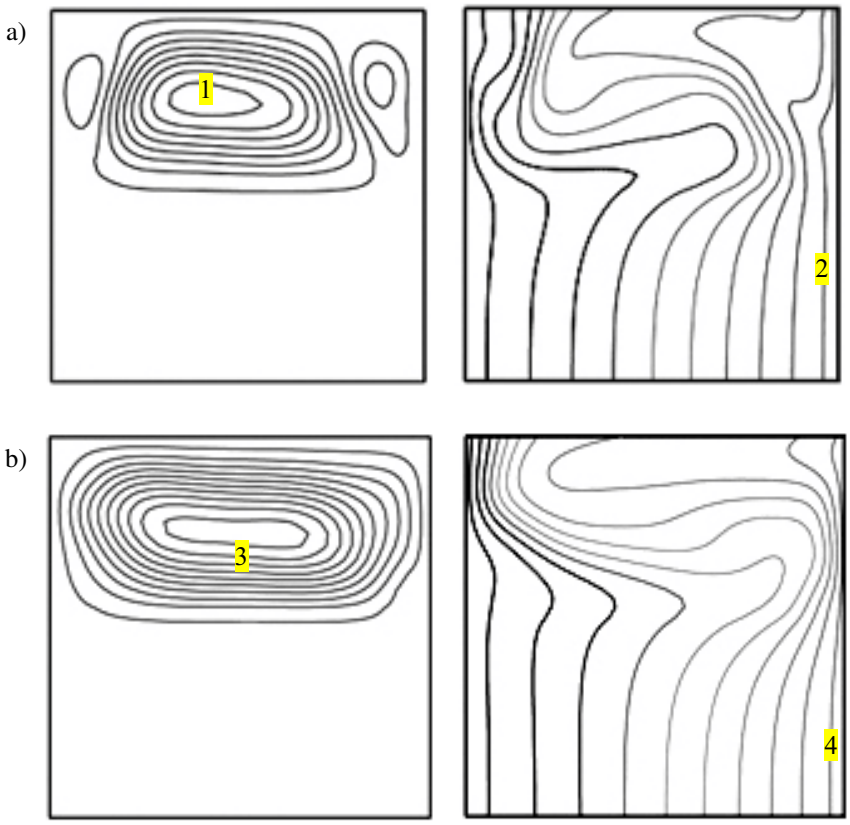

Fig. 5. Streamlines (left) and isotherms (right) for the thermo-solutal convection ($d = 0.5$):
a) 90 % water-10 % isopropanol, b) 50 % water-50 % isopropanol;
1) $\Psi = 1.66 \cdot 10^{-2}$, $\Delta\Psi = 2.28 \cdot 10^{-3}$; 2) $T = 302.75$ K, $\Delta T = 0.5$ K;
3) $\Psi = 6.10 \cdot 10^{-3}$, $\Delta\Psi = 6.48 \cdot 10^{-4}$; 4) $T = 302.75$ K, $\Delta T = 0.5$ K .

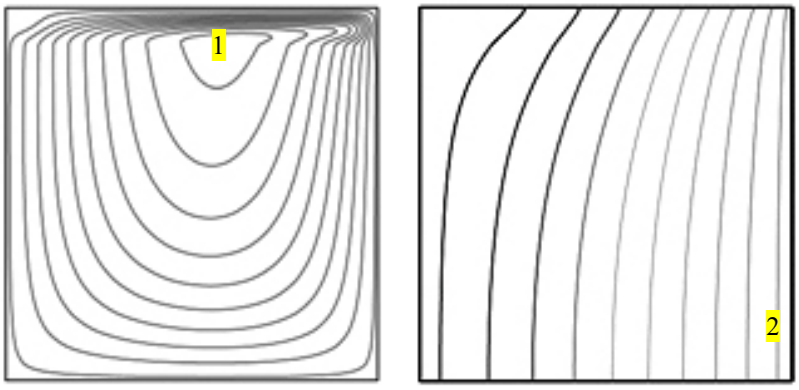

Fig. 6. Streamlines (left) and isotherms (right) for the thermo-solutal convection ($d = 0.5$):
1) $\Psi = 1.06 \cdot 10{-}4$, $\Delta\Psi = 1.14 \cdot 10{-}5$; 2) $T = 302.75$ K, $\Delta T = 0.5$ K.

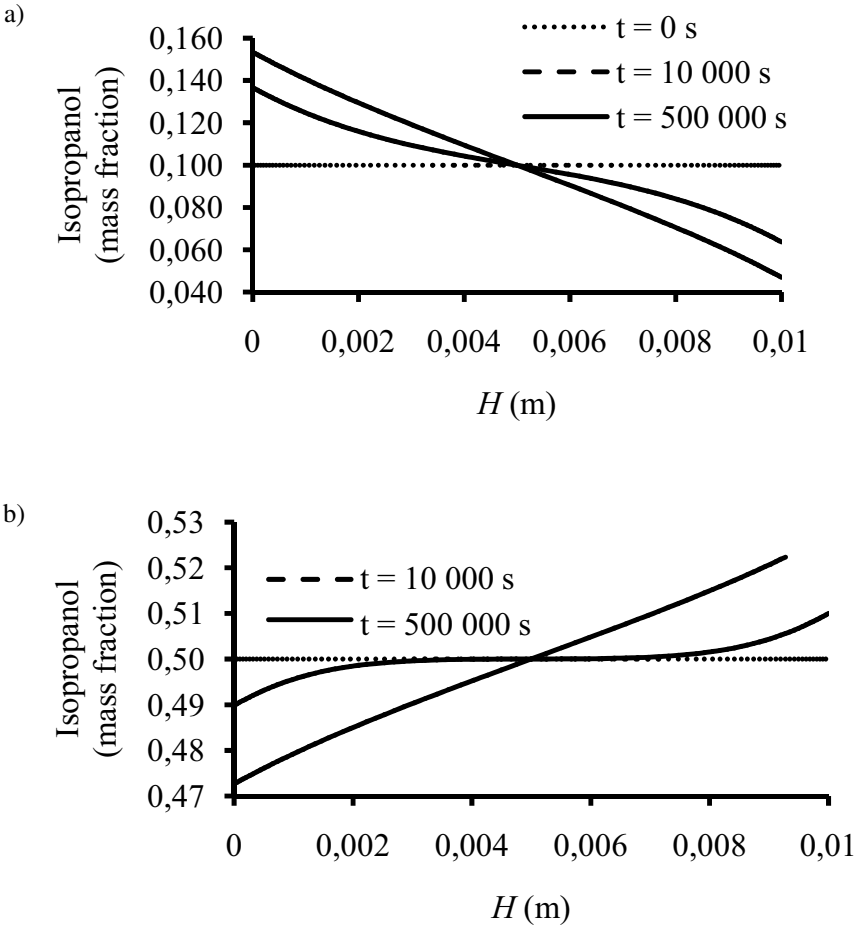

Fig. 7. Isopropanol distributions along the horizontal direction of the cavity at height 0.003 m ($d = 0.5$): a) 90 % water – 10 % isopropanol, b) 50 % water – 50 % isopropanol.

By comparing Figs. 7a and b, one can see that two figures have quite opposite behaviours. For the thermodiffusion with liquid 90 % water – 10 % isopropanol, the isopropanol component migrates to the cold side wall. But for the thermodiffusion with liquid 50 % water – 50 % isopropanol, the isopropanol component migrates to the hot side wall. The reason is that the two liquid mixtures have two opposite Soret coefficients. The Soret coefficient of 90 % water – 10 % isopropanol is negative but the Soret coefficient of 50 % water – 50 % isopropanol is positive.

5.3. Separation ratio. To measure the thermodiffusion effect on binary mixture, the separation ratio is calculated. The separation ratio is a very good indicator of the mass transfer process due to the thermodiffusion convection. The separation ratio of each component can be defined as follows,

$$q = \frac{(c/(1-c))_{\max}}{(c/(1-c))_{\min}}, \tag{13}$$

where c is the mass fraction of the species.

Fig. 8 shows the calculated separation ratios for different gravitational accelerations at the time step $t = 500000$ s. This figure clearly shows that the separation ratio decreases with increasing

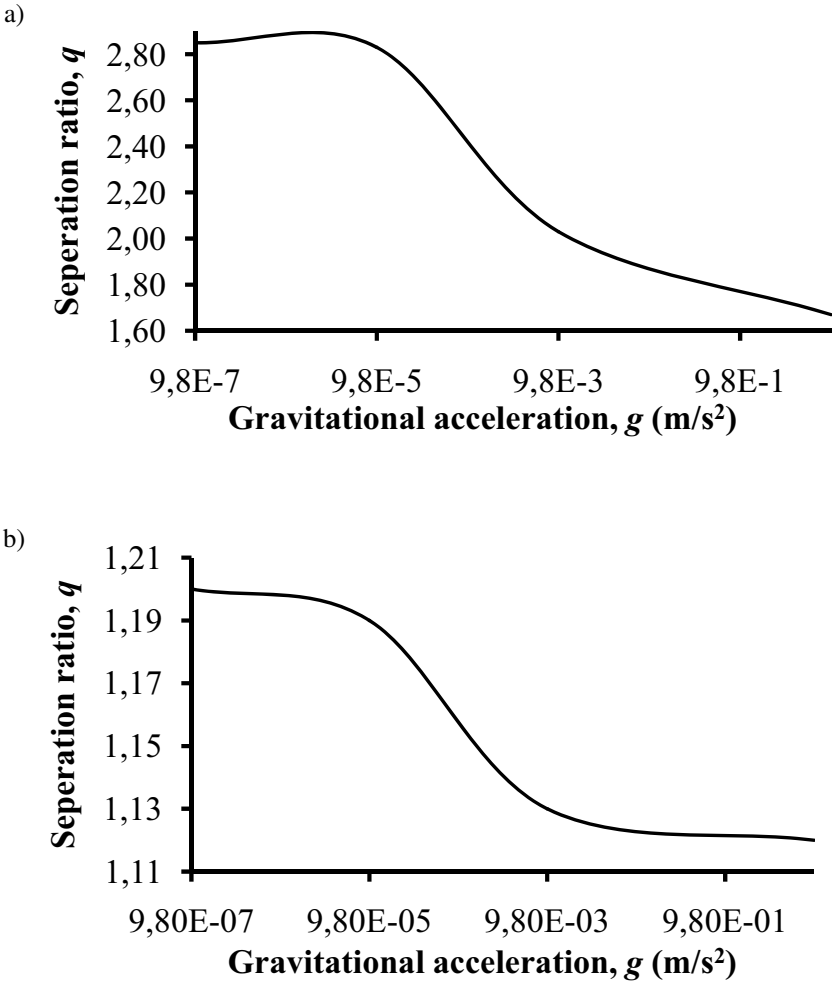

Fig. 8. Separation ratios for different gravity levels:
a) 90 % water – 10 % isopropanol, b) 50 % water – 50 % isopropanol.

gravitational acceleration whereas the minimum separation appears at the earth gravity condition ($g = 9.8\ \mathrm{m/s^2}$) due to mixing. As we know, the gravitational force is the main accelerating factor for the buoyancy body force term. Therefore, the buoyancy force increases with increasing gravitational acceleration and reduces the thermodiffusion effect. However, the separation ratio of the liquid mixture having negative S_T (90 % water – 10 % isopropanol) is more sensitive to the gravitational force than that of the liquid mixture having positive S_T (50 % water – 50 % isopropanol).

Conclusions

In this paper, thermo-solutal convection is studied in detail. For the thermo-solutal convection with the thickness ratio 0.5, multi cells are observed in the liquid layer for the liquid mixture having 90 % water – 10 % isopropanol. However, for the same thickness ratio, single cell is found for the

liquid mixture having 50 % water – 50 % isopropanol. Also, for the case with the thickness ratio 0.9, the flow penetrates into the porous layer. In the presence of thermodiffusion or the Soret effect, it is found that isopropanol components migrate either to the hot or to the cold wall, depending on the sign of the Soret coefficient of the liquid mixtures. In addition, gravitational acceleration is shown to have a strong effect on thermodiffusion convection.

Acknowledgement

The authors acknowledge the full support of the Natural Sciences and Engineering Research Council (NSERC), Canada.

REFERENCES

1. De Groot, S. R. and Mazur, P., *Non-Equilibrium Thermodynamics*, Dover, New York, 1984.
2. Firoozabadi, A., *Thermodynamics of Hydrocarbon Reservoirs*, McGraw-Hill, New York, 1991.
3. Khawaja, M., Jiang, G., Van-Vaerenberg, S., and Saghir, M. Z., Theoretical Analysis and Comparison with Experimentation of the Molecular and Thermal Diffusion Coefficients for Ternary Hydrocarbon Mixture, *J. Non-Equilibr. Thermodyn.*, 2005, **30**, pp. 359–374.
4. Pan, S., Jiang, G., Yan, Y., Kawaji, M., Saghir, Z., Theoretical Prediction of Thermal Diffusion in Water – Methanol, Water – Ethanol, and Water – Isopronol Mixtures Using the PC-SAFT Equation of State, *J. Non-Equilibr. Thermodyn.*, 2006, **31**, pp. 47–71.
5. Yan, Y., Blanco, P., Saghir, M. Z., and Bou-Ali, M. M., An Improved Theoretical Model for Thermal Diffusion Coefficient in Liquid Hydrocarbon Mixtures: Comparison between Experimental and Numerical Results, *J. Chem. Phys.*, 2008, **129**, pp. 194507.1–7.
6. Eslamian, M. and Saghir, M. Z., A Critical Review of Thermodiffusion Models: Role and Significance of the Heat of Transport and the Activation Energy of Viscous Flow, *J. Non-Equilibr. Thermodyn.*, 2009, **34**, pp. 97–131.
7. Van Vaerenbergh, S., Srinivasan, S., and Saghir, M. Z., Thermodiffusion in Multicomponent Hydrocarbon Mixtures: Experimental Investigations and Computational Analysis, *J. Chem. Phys.*, 2009, **131**, pp. 114505-1–8.
8. Kozak, R., Saghir, M. Z., and Viviani, A., Marangoni Convection in a Liquid Layer Overlying a Porous Layer with Evaporation at the Free Surface, *Acta Astronaut.*, 2004, **55**, pp. 189–197.
9. Nield, D. A. and Bejan, A., *Convection in Porous Media*, Springer-Verlag, New York, 1992.
10. Saghir, M. Z., Hennenberg, M., and Islam, M. R., Double Diffusive and Marangoni Convection in a Multi-Cavity System, *Int. J. Heat Mass Transfer*, 1998, **41**, No. 14, pp. 2157–2174.
11. Benano-Melly, L. B., Caltagirone, J.-P., Faissat, B., Montel, F., and Costeseque, P., Modeling Soret Coefficient Measurement Experiments in Porous Media Considering Thermal and Solutal Convection, *Int. J. Heat Mass Transfer*, 2001, **44**, pp. 1285–1297.
12. Jiang, C. G., Saghir, M. Z., Kawaji, M., Ghorayeb, K., Two-Dimensional Numerical Simulation of Thermo-Gravitational Convection in a Vertical Porous Column Filled with a Binary Fluid Mixture, *Int. J. Thermal Sci.*, 2004, **43**, pp. 1057–1065.
13. Deasaive, Th., Lebon, G., and Hennenberg, M., Coupled Capillary and Gravity-Driven Instability in a Liquid Film Overlying a Porous Layer, *Phys. Rev. E*, 2001, **64**, pp. 066304-1–8.
14. *FIDAP User Manual*, ver. 8.7.0, 1999.

15. Van Vaerenbergh, S. and Legros, J. C., Soret Coefficients of Organic Solutions Measured in the Microgravity SCM Experiment and by the Flow and the Bernard Cells, *J. Phys. Chem.*, 1998, **102**, pp. 4426–4431.
16. Shevtsova, V., Melnikov, D., Legros, J. C., Yan, Y., Saghir, M. Z., Lyubimova, T., Sedelnicov, G., and Roux, B., Influence of Vibrations on Thermodiffusion in Binary Mixture: A Benchmark of Numerical Solutions, *Phys. Fluids*, 2007, **19**, pp. 017111-1–15.

□◆◆◆□

Oscillatory MHD Couette Flow in a Rotating System[†]

R. R. Patra, S. L. Maji, S. Das, and **R. N. Jana**[*]

Department of Applied Mathematics, Vidyasagar University
Paschim Medinipur, West Bengal-721102, India
[*]E-mail: jana261171@yahoo.co.in

Unsteady oscillatory Couette flow between two infinite horizontal parallel plates in a rotating system has been studied when one of the plate is held at rest and the other oscillates in its own plane .The effects of rotation and frequency parameter on the velocities and the shear stresses for steady and unsteady flow have been studied. It is found that the unsteady shear stress due to primary flow has a phase lag for $2K^2 \leq \lambda$ and a phase lead for $\lambda < 2K^2$ over the plate oscillation. On the other hand, the unsteady shear stress due to secondary flow has a phase lag over the oscillations of the plate either for $2K^2 \leq \lambda$ or $\lambda < 2K^2$, where K^2 is the rotation parameter and λ is the frequency parameter.

* * *

Introduction

The study of fluid flow in a rotating environment has considerable bearing on the problems of geophysial, astrophysical and fluid engineering applications. An extensive literature exists on the flow of fluids in a rotating frame. Nanda and Mohanty [1] have studied the hydromagnetic steady flow in a rotating channel with constant pressure gradient. Majumder [2] has studied the effect of wall conductances on the hydromagnetic flow in a rotating system. Datta and Jana [3] have discussed the effect of rotation and Hall current on the hydromagnetic flow using non-conducting walls. Jana et al. [4] have studied the MHD Couette flow in rotating frame of referance when the fixed plate of the channel was a perfect conductor, the moving one was non-conducting . Recently Nagy and Demendy [5] have studied the hydromagnetic flow under general wall conditions. The combined effects of Hall current and rotation on the flow structure and heat transfer in a generalised hydromagnetic flow have been studied by Nagy and Demendy [6]. Guria et al. [7] have studied the hydromagnetic flow in a rotating channel in the presence of inclined magnetic field. The unsteady Couette flow in a rotating system have been studied by Guria et al. [8]. The unsteady hydromagnetic Couette flow in a rotating system under boundary layer approximation has been studied by Majumder [9], Ganapaty [10] and Guria et al. [11].

[†]Received 15.03.2009

ISSN 1064-2277
© 2010 Begell House, Inc.

The present investigation is devoted to study the hydromagnetic Couette flow through a horizontal channel when one of the plate is oscillating about the mean velocity and the other is held at rest in a rotating system under boundary layer approximations. It is found that the unsteady part of the primary velocity increases while that part of the secondary velocity decreases with increase in Hartmann number M. It is also found that phase of the shear stress due to unsteady part of the primary flow at the plate $\eta = 0$ has always a phase lead for $2k^2 < \lambda$ and a phase lag for $2K^2 > \lambda$. On the other hand, phase of the shear stress due to the unsteady secondary secondary has a phase lead over the plate oscillation.

1. Mathematical Formulation and its Solution

Consider the unsteady viscous incompressible electrically conducting fluid bounded by two infinitely long horizontal parallel plates separated by a distance d, the lower plate is held at rest and the upper plate is oscillating in its own plane with a velocity $U(t)$ about a constant mean velocity U_0 in the direction of x-axis where x-axis is taken on the lower plate in the direction of the flow. The y-axis is normal to the plates and the z-axis perpendicular to the xy-plane. A uniform magnetic field H_0 is applied perpendicular to the plates. Since the plates are infinitely long, all physical variables, except pressure, depend on y and t only.

We shall assume that the induced magnetic field produced by the motion of the conducting fluid is negligible so that $\boldsymbol{H} \equiv (0, H_0, 0)$. In the absence of an external electric field the effect of polarisation of the fluid is negligible.We shall also assume that the electric field $\boldsymbol{E} = 0$, Mayer [12].

The Navier – Stokes equations of motion for a conducting fluid are

$$\frac{\partial v_x}{\partial t} - 2\Omega v_y = -\frac{1}{\rho}\frac{\partial p}{\partial x} + \nu\frac{\partial^2 v_x}{\partial y^2} - \frac{\sigma B_0^2}{\rho} v_x, \tag{1}$$

$$\frac{\partial v_y}{\partial t} + 2\Omega v_x = -\frac{1}{\rho}\frac{\partial p}{\partial x} + \nu\frac{\partial^2 v_y}{\partial y^2} - \frac{\sigma B_0^2}{\rho} v_y, \tag{2}$$

$$0 = -\frac{1}{\rho}\frac{\partial p}{\partial z}, \tag{3}$$

where ρ, ν, Ω and p are respectively the fluid density, kinematic viscosity, angular velocity and fluid pressure.

The boundary conditions are

$$\begin{aligned} v_x = 0, \quad v_y = 0 \quad \text{at} \quad y = 0, \\ v_x = U(t), \quad v_y = 0 \quad \text{at} \quad y = d. \end{aligned} \tag{4}$$

Under usual boundary layer approximations, Eqs. (1) and (2) become

$$\frac{\partial v_x}{\partial t} - 2\Omega v_y = \frac{\partial U}{\partial t} + \nu\frac{\partial^2 v_x}{\partial y^2} - \frac{\sigma B_0^2}{\rho}(v_x - U), \tag{5}$$

$$\frac{\partial v_y}{\partial t} + 2\Omega(v_x - U) = -\frac{1}{\rho}\frac{\partial p}{\partial x} + \nu\frac{\partial^2 v_y}{\partial y^2} - \frac{\sigma B_0^2}{\rho} v_y. \tag{6}$$

Introducing non-dimensional variables

$$\eta = \frac{y}{d}, \qquad u = \frac{v_x}{U_0}, \qquad v = \frac{v_y}{U_0}, \qquad U = U_0 f(\tau),$$
$$\tau = \frac{\nu t}{d^2}, \qquad M^2 = \frac{\sigma \mu_e^2 H_0^2 d^2}{\rho \nu} \qquad K^2 = \frac{\Omega d^2}{\nu}, \tag{7}$$

Eqs. (5) and (6) become

$$\frac{\partial u}{\partial \tau} - 2K^2 v = \frac{\partial f}{\partial \tau} + \frac{\partial^2 u}{\partial \eta^2} - M^2(u - f), \tag{8}$$

$$\frac{\partial v}{\partial \tau} + 2K^2(u - f) = \frac{\partial^2 v}{\partial \eta^2} - M^2 v. \tag{9}$$

The boundary conditions Eq. (4) reduce to

$$\begin{aligned} u = 0, \quad v = 0 \quad \text{at} \quad \eta = 0 \\ u = f(\tau), \quad v = 0 \quad \text{at} \quad \eta = 1. \end{aligned} \tag{10}$$

We assume the plate velocity in the form of a Fourier series as

$$f(\tau) = U_0 + \sum_{n=1}^{\infty} \left[U_n \cos n\lambda\tau + U_n^* \sin n\lambda\tau \right] = U_0 + \mathbf{Re} \sum_{n=1}^{\infty} \bar{U}_n \exp(in\lambda\tau), \tag{11}$$

where $\bar{U}_n = U_n - iU_n^*$ and $\mathbf{Re}$ denotes the real part.

The coefficients U_0, U_n, U_n^* are the dimensionless Fourier constants of the function $f(\tau)$ when expressed in its fundamental period $2\pi/\lambda$, where $\lambda = \omega d^2/\nu$ being the dimensionless frequency of the oscillations. These may be interpreted as dimensionless constants representing the amplitudes of the oscillating plate velocity superposed upon the constant mean velocity U_0.

In view of Eq. (11), solution of the Eqs. (8) and (9) can be written in the following form:

$$u = u_0(\eta) + \mathbf{Re} \sum_{n=1}^{\infty} u_n(\eta) \exp(in\lambda\tau), \tag{12}$$

$$v = v_0(\eta) + \mathbf{Re} \sum_{n=1}^{\infty} v_n(\eta) \exp(in\lambda\tau). \tag{13}$$

On the use of Eqs. (11) – (13), Eqs. (8) and (9) become

$$in\lambda u_n - 2K^2 v_n = in\lambda \bar{U}_n + u_n'' - M^2(u_n - \bar{U}_n), \tag{14}$$

$$in\lambda v_n + 2K^2(u_n - \bar{U}) = v_n'' - M^2 v_n, \tag{15}$$

where $n = 0, 1, 2, \ldots$.

The boundary conditions Eq. (10) become

$$\begin{aligned} u_n = 0, \quad v_n = 0 \quad \text{at} \quad \eta = 0 \\ u_n = \bar{U}_n, \quad v_n = 0 \quad \text{at} \quad \eta = 1. \end{aligned} \tag{16}$$

Eqs. (14) and (15) subjected to the boundary conditions Eq. (16) can easily be solved and the solution for the primary and secondary velocities can be written as

$$u(\eta,\tau) = u_0(\eta) + \mathbf{Re}\sum_{n=1}^{\infty}\bar{U}_n\Bigg[1-\frac{1}{2}\Bigg\{\cosh(\alpha_1\pm i\beta_1)\eta+\cosh(\alpha_2+i\beta_2)\eta \\ -\frac{\cosh(\alpha_1\pm i\beta_1)}{\sinh(\alpha_1\pm i\beta_1)}\sinh(\alpha_1\pm i\beta_1)\eta-\frac{\cosh(\alpha_2+i\beta_2)}{\sinh(\alpha_2+i\beta_2)}\sinh(\alpha_2+i\beta_2)\eta\Bigg\}\Bigg]e^{i\lambda\tau}, \tag{17}$$

$$v(\eta,\tau) = v_0(\eta) + \mathbf{Re}\sum_{n=1}^{\infty}\frac{i}{2}\bar{U}_n\Bigg[\cosh(\alpha_1\pm i\beta_1)\eta-\cosh(\alpha_2+i\beta_2)\eta \\ -\frac{\cosh(\alpha_1\pm i\beta_1)}{\sinh(\alpha_1\pm i\beta_1)}\sinh(\alpha_1\pm i\beta_1)\eta+\frac{\cosh(\alpha_2+i\beta_2)}{\sinh(\alpha_2+i\beta_2)}\sinh(\alpha_2+i\beta_2)\eta\Bigg]e^{i\lambda\tau}, \tag{18}$$

where the upper sign for $n\lambda > 2K^2$ and the lower sign for $n\lambda < 2K^2$.

Further, $u_0(\eta)$ and $v_0(\eta)$ are the velocity components corresponding to the steady uniform velocity U_0 and are given by

$$u_0 + iv_0 = U_0\left[1-\cosh(\alpha+i\beta)\eta+\frac{\cosh(\alpha+i\beta)\eta}{\sinh(\alpha+i\beta)}\sinh(\alpha+i\beta)\eta\right], \tag{19}$$

where

$$\alpha\,,\beta\;=\frac{1}{\sqrt{2}}\left[\left(M^4+4K^4\right)^{1/2}\pm M^2\right]^{1/2}, \\ \alpha_1,\beta_1=\frac{1}{\sqrt{2}}\left[\left\{M^4+\left(n\lambda+2K^2\right)^2\right\}^{1/2}\pm M^2\right]^{1/2}, \\ \alpha_2,\beta_2=\frac{1}{\sqrt{2}}\left[\left\{M^4+\left(n\lambda-2K^2\right)^2\right\}^{1/2}\pm M^2\right]^{1/2}. \tag{20}$$

We shall now discuss a few particular cases of interest.

Case I: when $n\lambda \gg 1$, $K^2 \ll 1$ and $M^2 \ll 1$.

When $n\lambda$ is large order of magnitude then one can expect boundary layer type flow near the plates. For $n\lambda \gg 1$, $K^2 \ll 1$ and $M^2 \ll 1$, the velocity distribution are given by

$$u = u_0(\eta) + \sum_{n=1}^{\infty}\Bigg\{\left[U_n\cos n\lambda\tau + U_n^*\sin n\lambda\tau\right] \\ -\frac{1}{2}\Bigg[e^{-\alpha_1\eta}\left[U_n\cos(n\lambda\tau-\beta_1\eta)+U_n^*\sin(n\lambda\tau-\beta_1\eta)\right] \\ +e^{-\alpha_2\eta}\left[U_n\cos(n\lambda\tau-\beta_2\eta)+U_n^*\sin(n\lambda\tau-\beta_2\eta)\right]\Bigg]\Bigg\}, \tag{21}$$

$$v = v_0(\eta) + \frac{1}{2}\sum_{n=1}^{\infty}\Bigg\{e^{-\alpha_1\eta}\left[U_n^*\cos(n\lambda\tau-\beta_1\eta)-U_n\sin(n\lambda\tau-\beta_1\eta)\right] \\ -e^{-\alpha_2\eta}\left[U_n^*\cos(n\lambda\tau-\beta_2\eta)-U_n\sin(n\lambda\tau-\beta_2\eta)\right]\Bigg\}, \tag{22}$$

where

$$\alpha_{1,2} = \left(\frac{n\lambda}{2}\right)^{1/2}\left(1 \pm \frac{K^2}{n\lambda} + \frac{M^2}{2n\lambda}\right), \qquad \beta_{1,2} = \left(\frac{n\lambda}{2}\right)^{1/2}\left(1 \pm \frac{K^2}{n\lambda} - \frac{M^2}{2n\lambda}\right). \tag{23}$$

Eqs. (21) and (22) show the existence of double-decker boundary layers of thicknesses

$$\mathrm{O}\left\{\left(\frac{n\lambda}{2}\right)^{1/2}\left(1 + \frac{K^2}{n\lambda} + \frac{M^2}{2n\lambda}\right)\right\}^{-1} \qquad \text{and} \qquad \mathrm{O}\left\{\left(\frac{n\lambda}{2}\right)^{1/2}\left(1 - \frac{K^2}{n\lambda} + \frac{M^2}{2n\lambda}\right)\right\}^{-1}$$

near the plate $\eta = 0$. These layers may be identified as modified Stokes – Ekman – Hartmann layers as modified by the rotation parameter and magnetic field. It is seen that for each mode of pulsation, i. e. for fixed n, there are two associated layers. The thicknesses of these boundary layers decrease with the increase in n. The boundary layers arising due to higher mode of pulsation ($n > 1$) are confined inside the boundary layer due to fundamental mode of pulsation ($n = 1$).

The exponential terms in the above expressions damp out quickly as η increases. When

$$\eta \geq \left(\frac{n\lambda}{2}\right)^{1/2}\left(1 \pm \frac{K^2}{n\lambda} + \frac{M^2}{2n\lambda}\right),$$

we have

$$u = u_0(\eta) + \sum_{n=1}^{\infty}\left[U_n \cos n\lambda\tau + U_n^* \sin n\lambda\tau\right], \qquad v = v_0(\eta). \tag{24}$$

The above equation shows that for large frequency parameter $n\lambda$, the fluctuating part of the primary flow will be in phase with the plate oscillations while the unsteady part of the secondary flow vanishes.

Case II: when $n\lambda \ll 1$, $M^2 \ll 1$ and $K^2 \gg 1$.

In this case, the velocity components are given by

$$\begin{aligned} u = u_0(\eta) + \sum_{n=1}^{\infty}\Bigg\{ & \left[U_n \cos n\lambda\tau + U_n^* \sin n\lambda\tau\right] \\ & -\frac{1}{2}\Big[e^{-\alpha_1\eta}\left[U_n \cos(n\lambda\tau - \beta_1\eta) + U_n^* \sin(n\lambda\tau - \beta_1\eta)\right] \\ & \quad + e^{-\alpha_2\eta}\left[U_n \cos(n\lambda\tau - \beta_2\eta) + U_n^* \sin(n\lambda\tau - \beta_2\eta)\right]\Big]\Bigg\}, \end{aligned} \tag{25}$$

$$\begin{aligned} v = v_0(\eta) + \frac{1}{2}\sum_{n=1}^{\infty}\Big\{ & e^{-\alpha_1\eta}\left[U_n^* \cos(n\lambda\tau - \beta_1\eta) - U_n \sin(n\lambda\tau - \beta_1\eta)\right] \\ & - e^{-\alpha_2\eta}\left[U_n^* \cos(n\lambda\tau - \beta_2\eta) - U_n \sin(n\lambda\tau - \beta_2\eta)\right]\Big\}, \end{aligned} \tag{26}$$

where

$$\alpha_{1,2} = K\left(1 \pm \frac{n\lambda}{4K^2} + \frac{M^2}{4K^2}\right), \qquad \beta_{1,2} = K\left(1 \pm \frac{n\lambda}{4K^2} - \frac{M^2}{4K^2}\right). \tag{27}$$

It is seen from above Eqs. (25) and (26) that for large rotation, that is for large values of $2K^2$ there exist double-deck boundary layers near the plate $\eta = 0$. The thicknesses of these boundary layers are of order

$$\mathrm{O}\left\{K\left(1+\frac{n\lambda}{4K^2}+\frac{M^2}{4K^2}\right)\right\}^{-1} \text{ and } \qquad \mathrm{O}\left\{K\left(1+\frac{n\lambda}{4K^2}+\frac{M^2}{4K^2}\right)\right\}^{-1}$$

near the plate $\eta = 0$. These layers may be identified as the Ekman layers.

The exponential terms in the above expressions damp out quickly as η increases. When

$$\eta \geq K\left(1 \pm \frac{n\lambda}{4K^2}+\frac{M^2}{4K^2}\right),$$

we get

$$u = u_0(\eta) + \sum_{n=1}^{\infty}\left[U_n \cos n\lambda\tau + U_n^* \sin n\lambda\tau\right], \qquad v = v_0(\eta). \tag{28}$$

Similar to the above Case I, it is observed from the above equation that for large rotation parameter K^2, the fluctuating part of the primary flow will be in phase with the plate oscillations while the unsteady part of the secondary flow vanishes.

Case III: when $M^2 \gg 1$, $K^2 \ll 1$ and $n\lambda \ll 1$.

When $M^2 \gg 1$, $K^2 \ll 1$ and $n\lambda \ll 1$, in this case also the flow field is of boundary layer type and we obtain the velocity distribution as

$$\begin{aligned} u = u_0(\eta) + \sum_{n=1}^{\infty}\Bigg\{ & \left[U_n \cos n\lambda\tau + U_n^* \sin n\lambda\tau\right] \\ & -\frac{1}{2}\Big[e^{-M\eta}\left[U_n \cos(n\lambda\tau - \beta_1\eta) + U_n^* \sin(n\lambda\tau - \beta_1\eta)\right] \\ & \qquad +e^{-M\eta}\left[U_n \cos(n\lambda\tau - \beta_2\eta) + U_n^* \sin(n\lambda\tau - \beta_2\eta)\right]\Big]\Bigg\}, \end{aligned} \tag{29}$$

$$\begin{aligned} v = v_0(\eta) + \frac{1}{2}\sum_{n=1}^{\infty}\Big\{ & e^{-M\eta}\left[U_n^* \cos(n\lambda\tau - \beta_1\eta) - U_n \sin(n\lambda\tau - \beta_1\eta)\right] \\ & -e^{-M\eta}\left[U_n^* \cos(n\lambda\tau - \beta_2\eta) - U_n \sin(n\lambda\tau - \beta_2\eta)\right]\Big\}, \end{aligned} \tag{30}$$

where

$$\beta_1, \beta_2 = \frac{1}{2M}(n\lambda \pm 2K^2).$$

The above expressions show the existence of a single boundary layer of thickness of order of $\mathrm{O}(M)^{-1}$. This layer decreases with increase in M. It is interesting to note that this boundary layer thickness is independent of both M^2 and K^2. It is seen that in certain core $\eta \geq 1/M$, the exponential terms in Eqs. (29) and (30) damp out and the velocity field reduces to

$$u = u_0(\eta) + \sum_{n=1}^{\infty}\left[U_n \cos(n\lambda\tau) + U_n^* \sin(n\lambda\tau)\right], \qquad v = v_0(\eta). \tag{31}$$

Similar to the above Cases I and II, in this case also we observed from above equation that for large Hartmann number M, the fluctuating part of the primary flow will be in phase with the plate oscillations while the unsteady part of the secondary flow vanishes.

2. Single Plate Oscillation

In the limit $d \to \infty$, Eqs. (18) and (19) become

$$\begin{aligned} u = u_0(\eta) + \sum_{n=1}^{\infty} \Bigg\{ & [U_n \cos n\omega t + U_n^* \sin n\omega t] \\ & -\frac{1}{2}\left(U_n^2 + U_n^{*2}\right) \Bigg[e^{-\alpha_1^* y/\sqrt{2\nu}} \cos\left(n\omega t \mp \frac{\beta_1^* y}{\sqrt{2\nu}} - \theta\right) \\ & \quad + e^{-\alpha_2^* y/\sqrt{2\nu}} \left[U_n \cos\left(n\omega t - \frac{\beta_2{}^* y}{\sqrt{2\nu}}\right) + U_n^* \sin\left(n\omega t - \frac{\beta_2{}^* y}{\sqrt{2\nu}}\right) \right] \Bigg] \Bigg\}, \end{aligned} \tag{32}$$

$$\begin{aligned} v = v_0(\eta) + \frac{1}{2}\left(U_n^2 + U_n^{*2}\right) \sum_{n=1}^{\infty} \Bigg\{ & e^{-\alpha_1^* y/\sqrt{2\nu}} \sin\left(n\omega t \mp \frac{\beta_1^* y}{\sqrt{2\nu}} - \theta\right) \\ & - e^{-\alpha_2^* y/\sqrt{2\nu}} \sin\left(n\omega t - \frac{\beta_1^* y}{\sqrt{2\nu}} - \theta\right) \Bigg\}, \end{aligned} \tag{33}$$

where $u_0(\eta)$ and $v_0(\eta)$ are the velocity fields corresponding to the steady uniform velocity U_0 and are given by

$$u_0(\eta) = 1 - e^{\alpha^* y/\sqrt{2\nu}} \cos\left(\frac{\beta^* y}{\sqrt{2\nu}}\right), \qquad v_0(\eta) = -e^{\alpha^* y/\sqrt{2\nu}} \sin\left(\frac{\beta^* y}{\sqrt{2\nu}}\right), \tag{34}$$

where

$$\theta = \tan^{-1}\left(U_n^*/U_n\right),$$

$$\begin{aligned} \alpha^*, \beta^* &= \left\{ \left[\left(\frac{\sigma\mu_e^2 H_0^2}{\rho}\right)^2 + 4\Omega^2 \right]^{1/2} \pm \frac{\sigma\mu_e^2 H_0^2}{\rho} \right\}^{1/2}, \\ \alpha_1^*, \beta_1^* &= \left\{ \left[\left(\frac{\sigma\mu_e^2 H_0^2}{\rho}\right)^2 + (n\omega + 2\Omega)^2 \right]^{1/2} \pm \frac{\sigma\mu_e^2 H_0^2}{\rho} \right\}^{1/2}, \\ \alpha_2^*, \beta_2^* &= \left\{ \left[\left(\frac{\sigma\mu_e^2 H_0^2}{\rho}\right)^2 + (n\omega - 2\Omega)^2 \right]^{1/2} \pm \frac{\sigma\mu_e^2 H_0^2}{\rho} \right\}^{1/2}. \end{aligned} \tag{35}$$

The above Eqs. (32) and (33) represent the velocity components in the presence of a uniform transverse magnetic field in a rotating system when the free-stream velocity oscillates with velocity

$$U_0 + \sum_{n=1}^{\infty} \left(U_n \cos n\omega t + U_n^* \sin n\omega t\right).$$

Eqs. (32) and (33) show that the unsteady velocities consists of two parts, one oscillates with amplitude

$$\frac{1}{2}\left(U_n^2 + U_n^{*2}\right) e^{-\alpha_1^* y/\sqrt{2}\,\nu}$$

and the other with

$$\frac{1}{2}\left(U_n^2 + U_n^{*2}\right) e^{-\alpha_2^* y/\sqrt{2}\,\nu},$$

where α_1^* and α_2^* are given by Eq. (35). The boundary layer corresponding to the amplitude

$$\frac{1}{2}\left(U_n^2 + U_n^{*2}\right) e^{-\alpha_1^* y/\sqrt{2}\nu}$$

at a distance y from the plate oscillates with phase lag of $(\beta_2^* y/\sqrt{2}\nu + \theta)$ for $n\omega > 2\Omega$ and phase advance $(\beta_2^* y/\sqrt{2}\nu - \theta)$ for $n\omega < 2\Omega$ while the layer corresponding to the amplitude

$$\frac{1}{2}\left(U_n^2 + U_n^{*2}\right) e^{-\alpha_2^* y/\sqrt{2}\nu}$$

oscillates with phase lag of $(\beta_2^* y/\sqrt{2}\nu + \theta)$ either for $n\omega > 2\Omega$ or $n\omega < 2\Omega$. If $U_n = U_n^* = 0$, then $u(\eta)$ and $v(\eta)$ are given by Eq. (34). This results are identical with the result obtained by Batchelor [13].

3. Flow Under Harmonic Oscillations of the Plate

In this section, we shall consider the particular case when the plate velocity is given by

$$f(\tau) = U_0 + U_1 \cos\lambda\tau. \tag{36}$$

The flow field is then ccharacterized by

$$\begin{aligned} u(\eta,\tau) = u_0(\eta) + \mathbf{Re}\Bigg\{ U_1 \Bigg[1 - \frac{1}{2}\Bigg\{ &\cosh(\alpha_1 \pm i\beta_1)\eta + \cosh(\alpha_2 + i\beta_2)\eta \\ &- \frac{\cosh(\alpha_1 \pm i\beta_1)}{\sinh(\alpha_1 \pm i\beta_1)} \sinh(\alpha_1 \pm i\beta_1)\eta - \frac{\cosh(\alpha_2 + i\beta_2)}{\sinh(\alpha_2 + i\beta_2)} \sinh(\alpha_2 + i\beta_2)\eta \Bigg\} \Bigg] e^{i\lambda\tau} \Bigg\}, \end{aligned} \tag{37}$$

$$\begin{aligned} v(\eta,\tau) = v_0(\eta) + \mathbf{Re}\Bigg\{ \frac{i}{2} U_1 \Bigg[&\cosh(\alpha_1 \pm i\beta_1)\eta - \cosh(\alpha_2 + i\beta_2)\eta \\ &- \frac{\cosh(\alpha_1 \pm i\beta_1)}{\sinh(\alpha_1 \pm i\beta_1)} \sinh(\alpha_1 \pm i\beta_1)\eta + \frac{\cosh(\alpha_2 + i\beta_2)}{\sinh(\alpha_2 + i\beta_2)} \sinh(\alpha_2 + i\beta_2)\eta \Bigg] e^{i\lambda\tau} \Bigg\}, \end{aligned} \tag{38}$$

where α_1, α_2, β_1, β_2 are obtained from Eq. (21) by putting $n = 1$.

The steady primary velocity u_0 and the secondary velocity v_0 have been drawn against η for different values of M^2 and K^2 in Figs. 1 and 2. It is seen that for fixed M^2, the primary velocity u_0 increases with increase in K^2. It is also seen that secondary velocity v_0 at any point increases for small values of K^2 while for large values of K^2, it increases near the plate $\eta = 0$ and decreases away form the plate $\eta = 0$. It is seen from Fig. 2 that the steady primary velocity u_0 increases with increase in M^2 while the steady secondary velocity v_0 decreases with increase in M^2.

For the discussion of the oscillatory part of the flow, the Figs. 3 – 7 have been drawn against η for the unsteady primary velocity u_{uns} and the secondary velocity v_{uns} for various values of K^2, λ and $\lambda\tau$ with $M^2 = 5$ and $U_1 = 1$. It is observed from Fig. 3 that the unsteady primary velocity at any point increases with increase in rotation parameter K^2. Fig. 4 shows that the unsteady secondary velocity steadily increases for $2K^2 \leq \lambda$ while for $2K^2 > \lambda$ it increases near the plate $\eta = 0$ and decreases away from the plate $\eta = 0$. It is seen from Fig. 5 that for fixed values of M^2, K^2 and

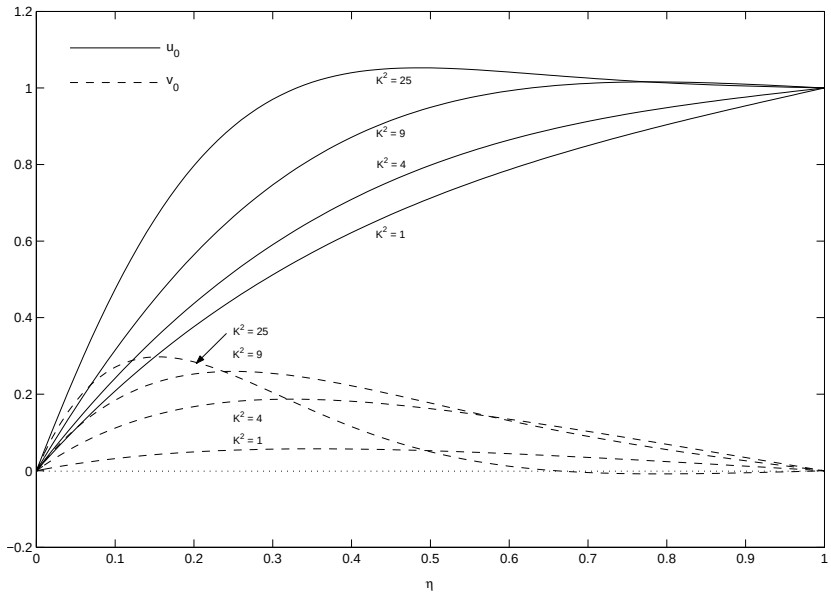

Fig. 1. Steady primary velocity u_0 and steady secondary velocity v_0 corresponding to the steady uniform velocity U_0 for K^2 with $M^2 = 5$.

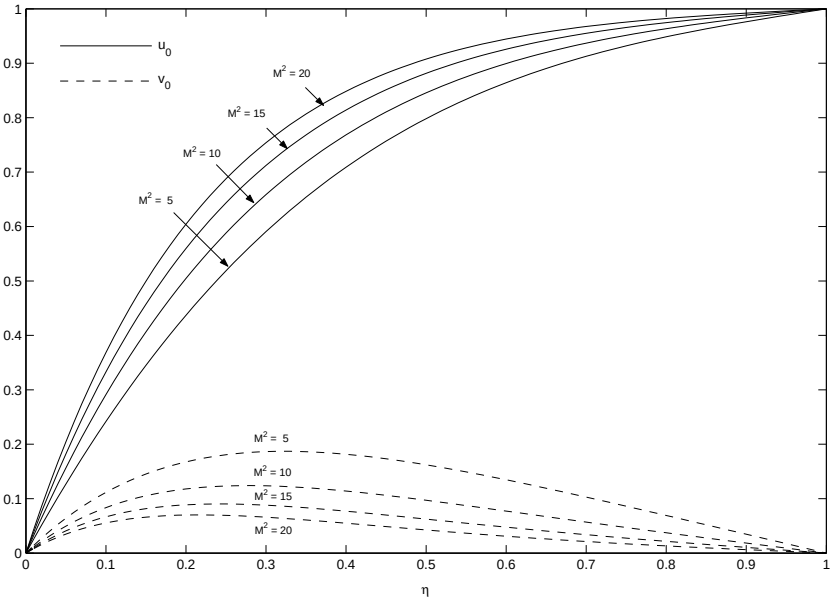

Fig. 2. Steady primary velocity u_0 and steady secondary velocity v_0 corresponding to the steady uniform velocity U_0 for M^2 with $K^2 = 4$.

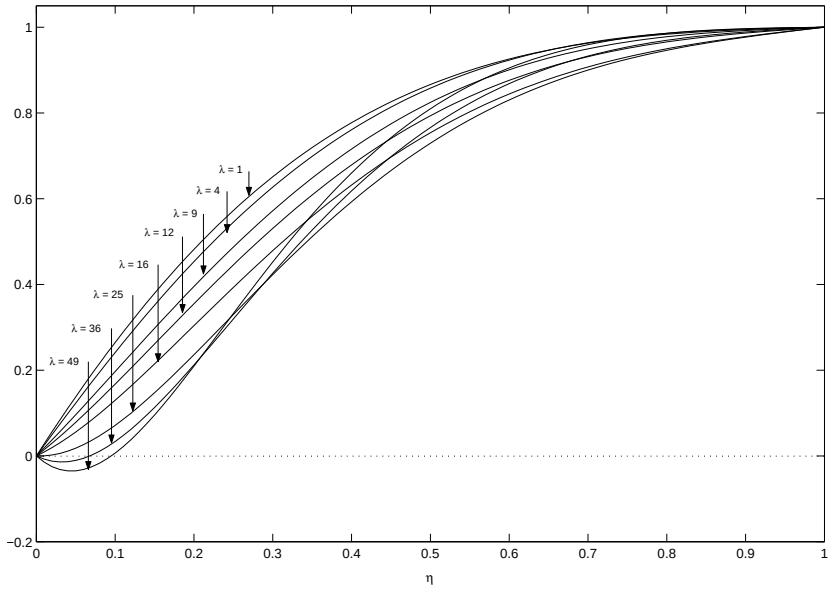

Fig. 3. Unsteady primary velocity $u_{\rm uns}$ for λ with $M^2 = 5$, $K^2 = 4$ and $\lambda\tau = 90^o$.

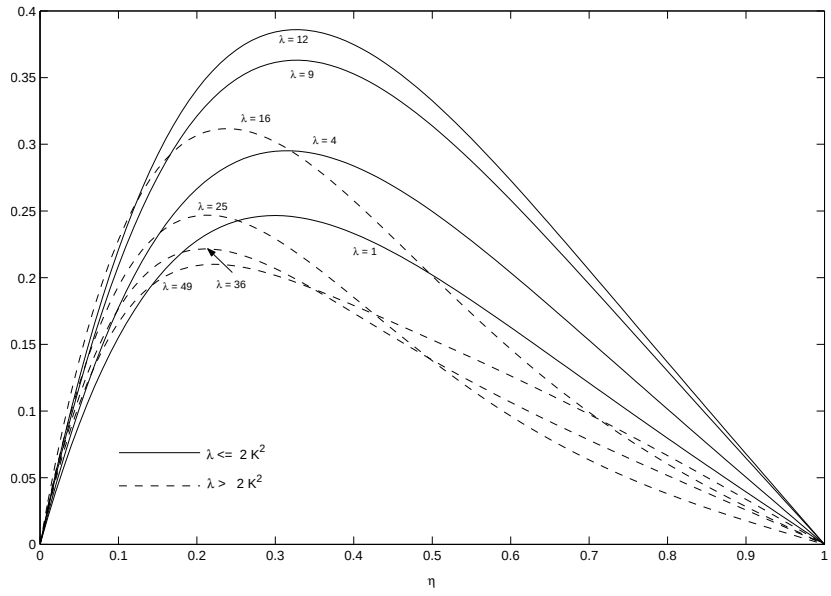

Fig. 4. Unsteady secondary velocity $v_{\rm uns}$ for λ with $M^2 = 5$, $K^2 = 4$ and $\lambda\tau = 90^o$.

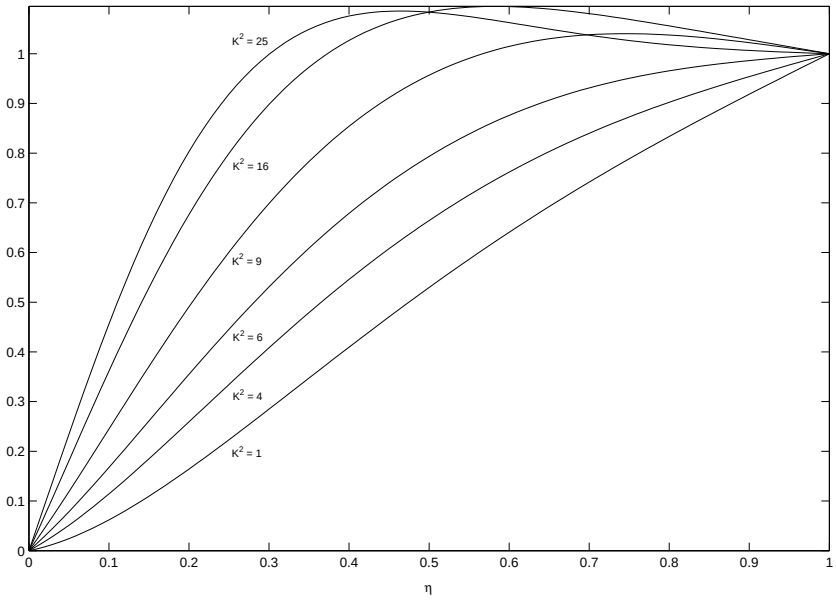

Fig. 5. Unsteady primary velocity u_{uns} for K^2 with $M^2 = 5$, $\lambda = 12$ and $\lambda\tau = 90^o$.

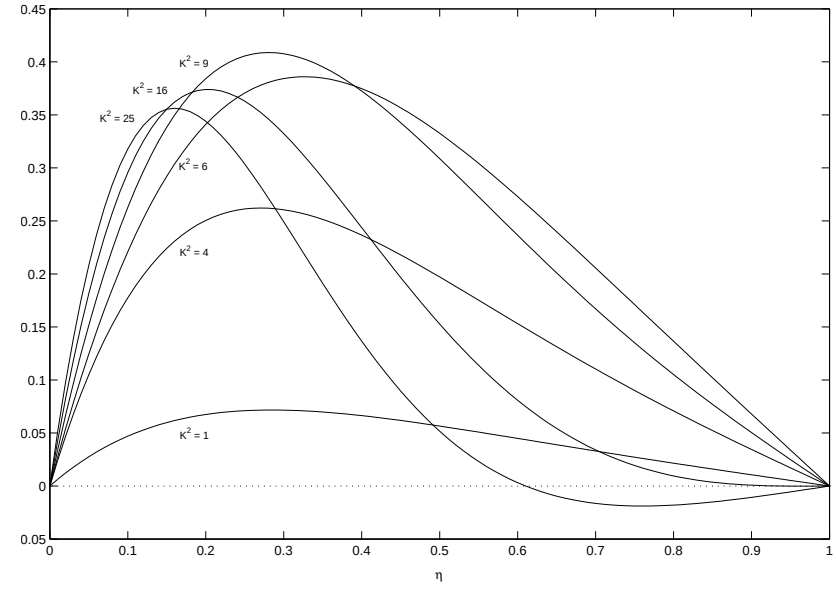

Fig. 6. Unsteady secondary velocity v_{uns} for K^2 with $M^2 = 5$, $\lambda = 12$ and $\lambda\tau = 90^o$.

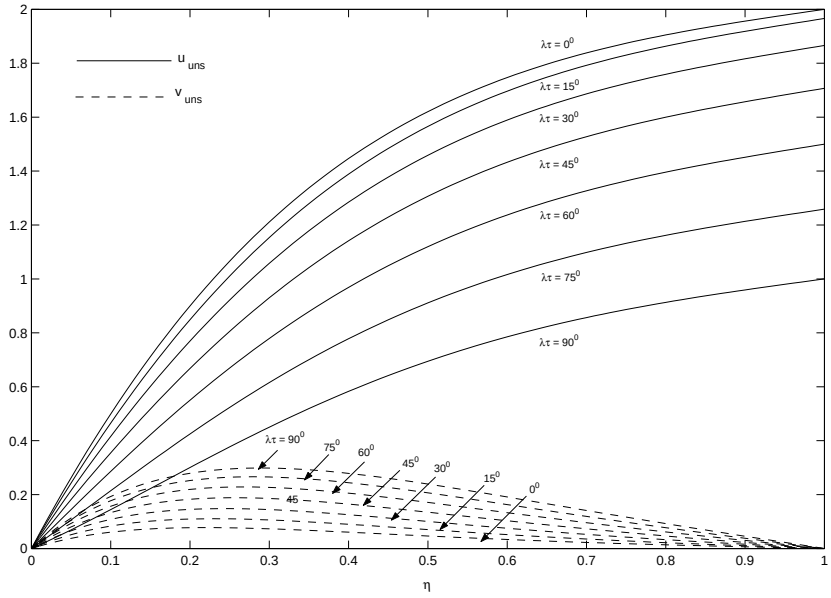

Fig. 7. Unsteady velocity distributions $u_{\rm uns}$ and $v_{\rm uns}$ for $\lambda\tau$ with $M^2 = 5$, $\lambda = 12$ and $K^2 = 4$.

$\lambda\tau$ the unsteady primary velocity decreases with increase in frequency parameter λ. It is observed from Fig. 6 that the unsteady secondary velocity increases with increase in λ for $2K^2 \geq \lambda$. On the other hand, for $\lambda > 2K^2$, it increases near the plate $\eta = 0$ and decreases away from the plate $\eta = 0$. Fig. 7 shows that the unsteady primary velocity decreases while the unsteady secondary velocity increases with increase in $\lambda\tau$.

The non-dimensional components of the shear stresses at the plate $\eta = 0$ are given by

$$\begin{aligned} \tau_u &= \left(\frac{du_0}{d\eta}\right)_{\eta=0} + \epsilon R_1 \cos(\lambda t + \phi_1), \\ \tau_v &= \left(\frac{dv_0}{d\eta}\right)_{\eta=0} + \epsilon R_2 \cos(\lambda t + \phi_2), \end{aligned} \tag{39}$$

where

$$\left[\frac{du_0}{d\eta}\right]_{\eta=0} = \frac{\alpha \sinh 2\alpha + \beta \sin 2\beta}{\cosh 2\alpha - \cos 2\beta}, \qquad \left[\frac{dv_0}{d\eta}\right]_{\eta=0} = \frac{\beta \sinh 2\alpha - \alpha \sin 2\beta}{\cosh 2\alpha - \cos 2\beta},$$

$$R_u = \frac{1}{2}\left[(x_1 + x_2)^2 + (y_2 \pm y_1)^2\right]^{1/2}, \qquad \tan\theta_u = \frac{y_2 \pm y_1}{x_2 + x_1}, \tag{40}$$

$$R_w = \frac{1}{2}\left[(y_1 \mp y_2)^2 + (x_1 - x_2)^2\right]^{1/2}, \qquad \tan\theta_w = \frac{x_1 - x_2}{y_1 \mp y_2},$$

$$x_1 = \frac{\alpha_1 \sinh 2\alpha_1 + \beta_1 \sin 2\beta_1}{\cosh 2\alpha_1 - \cos 2\beta_1}, \qquad y_1 = \frac{\beta_1 \sinh 2\alpha_1 - \alpha_1 \sin 2\beta_1}{\cosh 2\alpha_1 - \cos 2\beta_1}, \tag{41}$$

$$x_2 = \frac{\alpha_2 \sinh 2\alpha_2 + \beta_2 \sin 2\beta_2}{\cosh 2\alpha_2 - \cos 2\beta_2}, \qquad y_2 = \frac{\beta_2 \sinh 2\alpha_2 - \alpha_2 \sin 2\beta_2}{\cosh 2\alpha_2 - \cos 2\beta_2}. \tag{42}$$

Table 1.
Shear stresses at $\eta = 0$ with $\lambda = 9$

	$u_0'(0)$				$v_0'(0)$			
M^2	$K^2 = 1$	$K^2 = 4$	$K^2 = 9$	$K^2 = 16$	$K^2 = 1$	$K^2 = 4$	$K^2 = 9$	$K^2 = 16$
5	2.3163	2.6642	3.8763	4.3255	0.4074	1.4714	2.6243	3.6998
10	3.1875	3.3731	3.5656	4.6661	0.3090	1.1771	2.3041	3.4298
15	3.8845	3.9995	3.0008	5.0175	0.2562	0.9973	2.0539	3.1894
20	4.4788	4.5574	2.5214	5.3731	0.2229	0.8767	1.8585	2.9781

Table 2.
Values of R_1

	Different values of K^2 with $\lambda = 12$					Different values of λ with $K^2 = 6$				
M^2	1	4	6	9	16	1	4	12	16	25
5	3.2172	3.2999	3.4535	3.7957	4.6846	3.1291	3.1967	3.4535	3.6678	4.4000
10	3.7034	3.8331	3.9693	4.2555	5.0633	3.6798	3.7335	3.9693	4.1526	4.6778
15	4.2204	4.3372	4.4550	4.6905	5.3818	4.2066	4.2501	4.4550	4.6064	5.0284
20	4.7157	4.8129	4.9125	5.1082	5.6978	4.7058	4.7407	4.9125	5.0376	5.3888

Table 3.
Values of R_2

	Different values of K^2 with $\lambda = 12$					Different values of λ with $K^2 = 6$				
M^2	1	4	6	9	16	1	4	12	16	25
5	1.0333	1.5221	1.7238	1.9950	2.6026	1.1760	1.3131	1.7238	1.9120	2.0105
10	0.9413	1.3040	1.5131	1.7677	2.2398	0.9131	1.0839	1.5131	1.6849	1.9657
15	0.8305	1.1516	1.3487	1.6014	2.0677	0.7828	0.9452	1.3487	1.5186	1.8394
20	0.7440	1.0387	1.2218	1.4689	1.9418	0.6950	0.8450	1.2218	1.3895	1.7180

Table 4.
Values of $\tan\phi_1$

	Different values of K^2 with $\lambda = 12$					Different values of λ with $K^2 = 6$				
M^2	1	4	6	9	16	1	4	12	16	25
5	0.4055	0.4680	−0.5181	−0.5224	−0.4500	−0.3175	−0.3895	−0.5181	0.5270	0.5644
10	0.2695	0.3440	−0.3815	−0.4174	−0.4393	−0.2454	−0.2915	−0.3815	0.4094	0.4462
15	0.2015	0.2674	−0.3021	−0.3427	−0.3935	−0.1873	−0.2238	−0.3021	0.3316	0.3761
20	0.1596	0.2164	−0.2486	−0.2886	−0.3493	−0.1489	−0.1794	−0.2486	0.2765	0.3241

Table 5.
Values of $\tan\phi_2$

	Different values of K^2 with $\lambda = 12$					Different values of λ with $K^2 = 6$				
M^2	1	4	6	9	16	1	4	12	16	25
5	0.1560	0.4218	0.4910	0.3599	0.2820	0.4844	0.2712	0.4910	0.4944	0.4144
10	0.1146	0.3196	0.3780	0.3016	0.2251	0.0613	0.2021	0.3780	0.3923	0.3469
15	0.0906	0.2519	0.3014	0.2724	0.2058	0.0485	0.1594	0.3014	0.3206	0.3035
20	0.0740	0.2054	0.2481	0.2481	0.1941	0.0397	0.1299	0.2481	0.2686	0.2677

The values of $u_0'(0)$ and $v_0'(0)$ are given in Table 1 for different values of K^2 and M^2. It is observed from Table 1 that $u_0'(0)$ increases with the increase in either K^2 or M^2. On the other hand, $v_0'(0)$ increases with the increase in K^2 but it decreases with increase in M^2.

The values of R_1 and R_2 are entered in Tables 2 and 3 for various values of K^2, λ and M^2. It is seen from Table 2 that for fixed values of K^2 and $2K^2 < \lambda$, R_1 first increases, reaches a maximum and then decreases with increase in M^2 while for $2K^2 \geq \lambda$, it decreases with increase in M^2. It is also seen that for fixed values of M^2 and λ, R_1 decreases with increase in K^2. It is observed from Table 2 that R_2 decreases with increase in M^2 while it increases with increase in K^2. Table 3 shows that the amplitude R_2 increases with increase in either M^2 or λ. On the other hand, R_2 decreases with increase in M^2 but it increases with increase in λ.

The values of $\tan\phi_1$ and $\tan\phi_2$ have been plotted against λ in Tables 4 and 5. It is seen that $\tan\phi_1$ has a phase a lag over the oscillation for $2K^2 \leq \lambda$ and a phase lead over the oscillation for $2K^2 > \lambda$. It is also seen that $\tan\phi_2$ has always a phase lead over the oscillation either for $2K^2 \leq \lambda$ or $2K^2 > \lambda$. Tables 4 and 5 show that the magnitude of $\tan\phi_1$ and $\tan\phi_2$ decreases with increase in M^2. It is observed from Table 4 that that magnitude of $\tan\phi_1$ increases with increase in λ while it decreases with increase in K^2. Table 5 shows that $\tan\phi_2$ increases for $2K^2 \leq \lambda$ and decrease for $2K^2 > \lambda$ with increase in either λ or K^2.

Conclusion

Consider the unsteady viscous incompressible electrically conducting fluid bounded by two infinite long horizontal parallel plates separated by a distance d, the lower plate is held at rest and the upper plate is oscillating in its own plane with a velocity $U(t)$ about a constant mean velocity U_0 in the direction of flow. It is found that either for large frequency parameter $n\lambda$ or rotation parameter K^2, there exists a double-decker boundary layers whereas for large Hartmann number there exists a single-deck boundary layer. Further, for large values of either $n\lambda$ or M^2 or K^2, the fluctuating part of the primary flow will be in phase with the plate oscillations while the fluctuating part of the secondary velocity is identically equal to zero.

REFERENCES

1. Nanda, R. S. and Mohanty, H. K., Hydromagnetic Flow in a Rotating Channel, *Appl. Sci. Res.*, 1977, **24**, pp. 65–72.
2. Mazumder, B. S., Effect of Wall Conductance on Hydromagnetic Flow and Heat Transfer in a Rotating Channel, *Acta Mech.*, 1977, **28**, pp. 85–99.
3. Datta, N. and Jana, R. N., Hall Effect on Hydromagnetic Flow and Heat Transfer in a Rotating Channel, *J. Int. Math. Appl.*, 1977, **19**, pp. 217–229.
4. Datta, N., Jana, R. N., and Mazumder, B. S., Hydromagnetic Couette Flow and Heat Transfer in a Rotating System, *J. Phys. Soc. Japan*, 1978, **44**, pp. 363–370.
5. Nagy, T. and Demendy, Z., Influence of Wall Properties of Hartmann Flow and Heat Transfer in a Rotating System, *Acta Phys., Hungaria*, 1995, **73**, pp. 291–310.
6. Nagy, T. and Demendy, Z., Effects of Hall Currents and Coriolis Force on Hartmann Flow Under General Wall Condition, *Acta Mech.*, 1995, **113**, pp. 77–91.
7. Guria, M., Das, B. K., and Jana, R. N., Oscillatory Couette Flow in the Presence of an Inclined Magnetic Field, *Meccanica*, 2009, **44**, pp. 555–564.

8. Guria, M., Jana, R. N., and Ghosh, S. K., Unsteady Couette Flow in a Rotating System, *Int. J.Non-Linear Mech.*, 2006, **41**, pp. 838–843.
9. Mazumder, B. S., An Exact Solution of Oscillatory Couette Flow in a Rotating System, *ASME J. Appl. Mech.*, 1991, **58**, pp. 1104–1107.
10. Ganapaty, R., A Note on Oscillatory Couette Flow in a Rotating System, *ASME J. Appl. Mech.*, 1994, **61**, pp. 208–209.
11. Guria, M., Das, B. K., and Jana, R. N., Unsteady Couette Flow in a Rotating System, *Mechanica*, 2008, **43**, pp. 517–521.
12. Mayer, R. C., On Reducing Aerodynamic Heat-Transfer Rates by Magnetohydrodynamic Techniques, *J. Aero/Space Sci.*, 1958, **25**, pp. 561–566.
13. Batchelor, G. K., *An Introduction to Fluid Dynamics*, Cambridge Univ. Press, First Indian Edition, 1993, pp. 200.

□◆◆◆□

Analysis of Laminar Flow in a Channel with One Porous Bounding Wall[†]

N. M. Bujurke[1], **N. N. Katagi**[2], and **V. B. Awati** [3]

[1]Department of Mathematics,
Karnatak University
Dharwad-580003, India
E-mail: bujurke@yahoo.com

[2]Department of Mathematics,
Manipal Institute of Technology
Manipal-576104, India

[3]Department of Mathematics,
Government Fist Grade College
K. R. Puram, Bangalore-560036, India

Computer extended series solution is used to analyze the problem of laminar flow in a channel with one porous bounding wall. The objective is to study the effect of non-zero tangential slip velocity on the velocity field, pressure gradient and mass transfer. The problem is also studied using power series method in conjunction with an unconstrained optimization procedure. The domain and rate of convergence of the series so generated are further increased by Padé approximants. The coupled diffusion equation in the boundary layer is solved using a finite difference scheme. The solution presented here is valid for much larger Reynolds number compared with earlier investigation.

* * *

Nomenclature

c	solute concentration;
c_0	inlet solute concentration;
c_w	solute concentration at the membrane surface;
C	c/c_0;
C_p	an integration constant;
h	height of the channel;

[†]Received 20.02.2009

ISSN 1064-2277
© 2010 Begell House, Inc.

x the axial distance from the channel entrance;
y the coordinate axis perpendicular to the channel walls measured from the non-porous wall;
u velocity component in the x-direction;
u_0 average velocity over the channel at channel inlet;
$\overline{u}$ average velocity over the channel at a given value of x, $[1 - (\mathrm{Re}_w/\mathrm{Re}_{\mathrm{ent}})\,(x/h)]$;
u_s^0 normalized slip velocity, $(u/u_0)_{y=h}$;
u_s normalized slip velocity, $(u/\overline{u})_{y=h}$;
U u/u_0;
Re_w wall Reynolds number, $v_w h/\nu$;
$\mathrm{Re}_{\mathrm{ent}}$ Reynolds number for flow entering the channel, $u_0 h/\nu$;
v velocity component in the y-direction;
v_w velocity of the fluid through the membrane;
V v/v_w;

Greek symbols

α surface characteristic of the membrane;
Δp dimensionless pressure drop, $2[p(0,\lambda) - p(x,\lambda)]/(\rho u_0^2)$;
λ dimensionless variable in the y-direction, y/h;
μ viscosity;
ν kinematic viscosity;
ρ solution density;
φ slip coefficient, $\sqrt{k}/\alpha h$;
Ψ stream function;

Subscripts

$'$, $''$, $'''$, $^{\mathrm{iv}}$ 1-st, 2-nd, 3-rd, and 4-th order derivatives.

Introduction

The flow of a viscous fluid confined by porous walls finds applications in a variety of physical situations such as the control of boundary layer separation with suction or injection, filtration, membrane separation process and biological transport in living systems etc. Many research workers have investigated the steady, incompressible laminar flow of fluid in channels with uniformly porous walls. Berman [4] investigated the problem of steady laminar flow of a viscous incompressible fluid through a porous channel and found the solution for a small Reynolds number. Following authors Terrill [17–20], Brady [5], Robinson [14], Zaturska et al. [23], Cox [9] and Cox and King [10] have extended Berman's problem and obtained solution for both small and large Reynolds numbers. King and Cox [11] studied asymptotic analysis of the steady state and time dependent Berman Problem. In the earlier analysis majority have used no slip boundary conditions. But the experimental investigation reveals the existence of slip velocity at the porous bounding surface and is connected with the presence of a thin layer of streamwise moving fluid just below the surface of the porous medium. Beavers and Joseph [1] presented mass efflux experiments and proved the existence of a non-zero tangential (slip) velocity on the surface of a permeable boundary. Saffman [16] used statistical approach to derive the slip velocity. Neild [12] has given the historical background to the Beavers and Joseph condition at the interface of a porous media and a clear fluid. Recently Uri Shevit [21] investigated transport process across the interface between fluid and porous domains.

In the present study, the problem of laminar flow bounded by a rigid horizontal boundary on one side and porous boundary at the other side is considered (Chellam et al. [8]). The present work is an attempt to study the effect of non-zero tangential slip velocity on the velocity field, pressure gradient and concentration polarization using computer extended perturbation series with polynomial coefficient functions. Van Dyke [22] used long series analysis in laminar flow through a heated horizontal pipe. Recently, in the analysis of internal laminar flow separation, Bujurke et al. [6] have used series analysis in conjugation with sophisticated numerical schemes satisfactorily. In this paper we systematically use two new types of semi-analytical numerical techniques for the solution of the above problem and present some useful and interesting results. In the first method, the equations of motion in two dimensions are solved by perturbation method assuming slip velocity at the membrane for moderately large wall Reynolds number, $\mathrm{Re}_w \equiv V_w h/\nu$ and generate large number of universal polynomial coefficient functions for velocity profiles and pressure gradient using MATHEMATICA. Domb – Sykes plot confirms the convergence of the series for much larger parameter. In the second method we use power series method in conjugation with unconstrained optimization procedure and compare these computations. Later, the convection diffusion equation is solved by a finite difference technique incorporating the results of velocity profiles obtained in the earlier section. Padé approximants of various orders (diagonal P_N^N and off diagonal P_{N+1}^N) give converging sum for sufficiently large Re_w.

1. Mathematical Formulation

Consider the laminar flow of an incompressible fluid of density ρ and kinematic viscosity ν in a channel of rectangular cross section having one permeable boundary and another one as rigid. The width of the channel is assumed to be very large relative to the height, thus the flow will be assumed to be two dimensional and steady. The coordinate system used for the description of the problem is shown in Fig. 1. The channel is of length L and height h. The axial coordinate measured from the channel entrance is denoted by x and y the coordinate axis perpendicular to the channel walls measured from the non-porous wall. Values of u and v represent the velocity components in x- and y-directions respectively and p is the pressure.

The Navier – Stokes equations for steady, two dimensional, incompressible fluid motion under

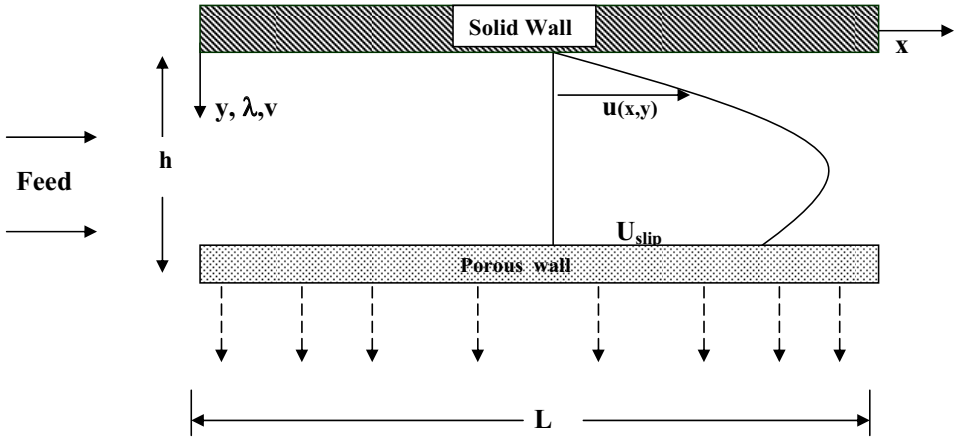

Fig. 1. The coordinate system used in the solution of the 2D steady state Navier – Stokes equations (Chellam et al. [8]).

the assumed conditions (with no external forces) are

$$u\frac{\partial u}{\partial x}+\frac{v}{h}\frac{\partial u}{\partial \lambda}=-\frac{1}{\rho}\frac{\partial p}{\partial x}+\nu\left(\frac{\partial^2 u}{\partial x^2}+\frac{1}{h^2}\frac{\partial^2 u}{\partial \lambda^2}\right), \tag{1}$$

$$u\frac{\partial v}{\partial x}+\frac{v}{h}\frac{\partial v}{\partial \lambda}=-\frac{1}{\rho h}\frac{\partial p}{\partial \lambda}+\nu\left(\frac{\partial^2 v}{\partial x^2}+\frac{1}{h}\frac{\partial^2 v}{\partial \lambda^2}\right), \tag{2}$$

$$\frac{\partial u}{\partial x}+\frac{1}{h}\frac{\partial v}{\partial \lambda}=0. \tag{3}$$

The boundary conditions are

$$u(x,0)=0, \qquad v(x,0)=0, \tag{4}$$

$$u(x,1)=v_w \qquad \text{(constant)}, \tag{5}$$

$$u(x,1)=-\varphi\frac{\partial u}{\partial \lambda}, \tag{6}$$

where $\lambda = y/h$ is the dimensionless variable in the y-direction.

Eqs. (4) are the no-slip boundary conditions for the flow of a viscous fluid past of solid surface. Eq. (5) mathematically describes the assumption of constant permeation rate (denotes suction rate at the permeable wall which is constant along the length of the channel). Eq. (6) is the slip boundary condition (Beavers and Joseph, [1]). The slip velocity at the membrane surface is proportional to the shear rate at the permeable boundary. This slip velocity is connected with the presence of a thin layer of streamwise moving fluid in the boundary region just below the permeable surface. The fluid in this layer is considered to be pulled along by the flow above the porous surface. $\varphi \equiv \sqrt{k}/\alpha h$ is the slip coefficient, where k is the permeability of the membrane material and α is a dimensionless constant dependent on the surface characteristics of the membrane.

By introducing a proper stream function (Berman [4]) of the form

$$\Psi(x,\lambda)=(hu_0-v_w x)f(\lambda) \tag{7}$$

into the Navier – Stokes equations (1), (2) and eliminating p, we get

$$\frac{d}{d\lambda}\left[\frac{v_w}{h}\left[(f')^2-ff''\right]+\frac{\nu}{h^2}f'''\right]=0 \tag{8}$$

or

$$\mathrm{Re}_w[f'f''-ff'''']+f^{\mathrm{iv}}=0. \tag{9}$$

Eq. (9) is one of the Falkner – Skan family of equations.

The new set of boundary conditions are

$$f=0, \qquad f'=0 \qquad \text{at} \qquad \lambda=0, \tag{10}$$

$$f=1, \qquad f'=-\varphi f'' \qquad \text{at} \qquad \lambda=1. \tag{11}$$

2. Mass Transfer Problem

As $v_w \ll u_0$ in all tangential membrane systems, this enables to neglect diffusion in the axial direction in comparison to diffusion in the transverse direction. The steady convection-diffusion equation describing the mass transfer in dimensionless form (Chellam et al. [8])

$$U\frac{\partial C}{\partial X} + V\,\frac{v_w L}{u_0 h}\,\frac{\partial C}{\partial \lambda} = \frac{DL}{u_0 h^2}\,\frac{\partial^2 C}{\partial \lambda^2} \tag{12}$$

and the corresponding boundary conditions are

$$C = 1, \qquad X = 0 \qquad \forall\ \lambda \tag{13}$$

$$\frac{\partial C}{\partial \lambda} = 0, \qquad \lambda = 0 \qquad \forall\ X, \tag{14}$$

$$\frac{\partial C}{\partial \lambda} = \frac{c_w}{c_0}\,\frac{v_w h}{D}, \qquad \lambda = 1 \qquad \forall\ X, \tag{15}$$

where $U = u/u_0$; $V = v/v_w$; $C = c/c_0$; $X = x/L$; $\lambda = y/h$; D is the diffusion coefficient and C denotes the concentration of the solute. Eq. (14) specifies that there is no-flux through the solid wall. Eq. (15) represents the boundary condition for a perfectly rejecting membrane (i. e., at steady state, when concentration profiles are established and invariant, mass transport to and from the boundary layer are equal thus effectively maintaining a dynamic balance). Value of c_0 is the uniform inlet concentration and is assumed to be the boundary condition at constant x, c_w represents unknown solute concentration at the porous wall.

3. Method of Solution

The Eq. (9) is solved by regular perturbation method. Towards this goal we seek a solution of Eq. (9) in the form

$$f(\lambda) = \sum_{n=0}^{\infty} \mathrm{Re}_w^n f_n(\lambda). \tag{16}$$

Substituting Eq. (16) into Eqs. (9) – (11) and equating like powers of Re_w on both sides, we get

$$f_n^{\mathrm{iv}} = \sum_{r=0}^{n-1} \left[f_r f'''_{n-1-r} - f'_r f''_{n-1-r} \right], \qquad n = 1, 2, 3, \ldots \tag{17}$$

with corresponding boundary conditions

$$\begin{aligned} f_n &= 0 \quad \text{at} \quad \lambda = 0 \quad \forall\ n \geq 0, \\ f'_n &= 0 \quad \text{at} \quad \lambda = 0 \quad \forall\ n \geq 0, \\ f_0 = 1,\ f_n &= 0 \quad \text{at} \quad \lambda = 1 \quad \forall\ n \geq 1, \\ f'_n + \varphi f''_n &= 0 \quad \text{at} \quad \lambda = 1 \quad \forall\ n \geq 0. \end{aligned} \tag{18}$$

The solution of the above equations up to the term in Re_w^1 is (Chellam et.al. [8])

$$f_0 = -\frac{2(1+\varphi)}{(1+4\varphi)}\lambda^3 + 3\frac{(1+2\varphi)}{1+4\varphi}\lambda^2,$$

$$f_1 = -\frac{2(1+\varphi)^2}{35(1+4\varphi)^2}\lambda^7 + \frac{(1+3\varphi+2\varphi^2)}{5(1+4\varphi)^2}\lambda^6 - \frac{3(1+2\varphi)^2}{10(1+4\varphi)^2}\lambda^5 \tag{19}$$

$$+\frac{3(9+90\varphi+272\varphi^2+296\varphi^3)}{70(1+4\varphi)^3}\lambda^3 - \frac{2(4+44\varphi+139\varphi^2+162\varphi^3)}{35(1+4\varphi)^3}\lambda^2.$$

4. Computer Extended Series Method

The analysis of the series Eq. (16) for its analyticity requires sufficiently large number of terms. It is difficult to perform this manually but it can be made automatic using MATHEMATICA. We are able to generate universal polynomial functions $f_n(\lambda)$, $n = 1, 2, \ldots, 30$ of Eq. (16) and analyze the series for its sum.

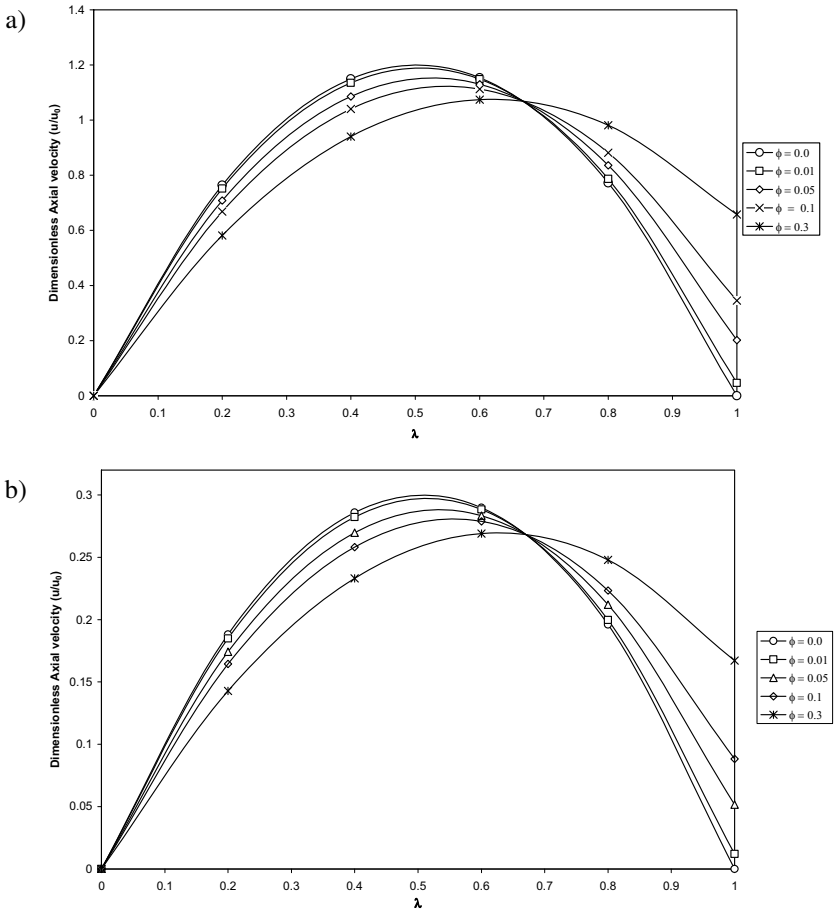

Fig. 2. Effect of the slip coefficient on the mid-channel axial velocity for $\mathrm{Re}_{\mathrm{ent}} = 1000$: a) $\mathrm{Re}_w = 0.1$, b) $\mathrm{Re}_w = 0.4$.

For the velocity profiles, we have

$$U = \frac{u}{u_0} = \left(1 - \frac{\mathrm{Re}_w}{\mathrm{Re}_{\mathrm{ent}}}\,\frac{x}{h}\right)\left(f_0'(\lambda) + \sum_{n=1}^{30} \mathrm{Re}_w^n f_n'(\lambda)\right), \tag{20}$$

$$V = \frac{v}{v_w} = f_0(\lambda) + \sum_{n=1}^{30} \mathrm{Re}_w^n f_n(\lambda), \tag{21}$$

where $\mathrm{Re}_{\mathrm{ent}} = u_0 h/v$ is the entrance Reynolds number. Eqs. (20) and (21) represent mid channel axial and transverse velocities normalized by local maximum values which are shown in Figs. 2 and 3.

The expression for the dimensionless pressure drop ΔP (normalized pressure gradient), along the channel length is given by

$$\Delta p = \frac{p(0,\lambda) - p(x,\lambda)}{0.5\rho u_0^2} = -\frac{2C_P\nu}{h^2 u_0^2}\left(u_0 x - \frac{v_w x^2}{2h}\right), \tag{22}$$

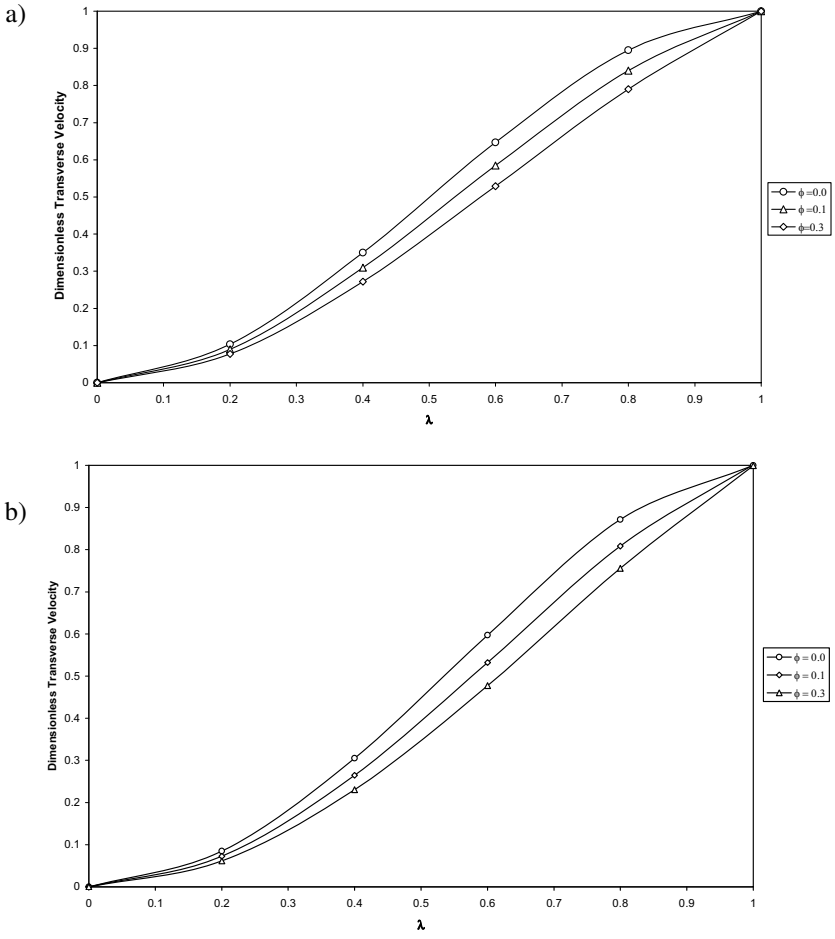

Fig. 3. The effect of slip coefficient on the mid-channel transverse velocity for $\mathrm{Re}_{\mathrm{ent}} = 1000$: a) $\mathrm{Re}_w = 0.1$, b) $\mathrm{Re}_w = 3$.

where C_P (integrating constant) is obtained from the Eq. (8) and is given by

$$C_P = f'''(0) = \sum_{n=0}^{\infty} \mathrm{Re}_w^n f_n'''(0) = \sum_{n=0}^{\infty} \mathrm{Re}_w^n a_n. \tag{23}$$

5. Power Series Method

To confirm the accuracy of the estimated results obtained using computer extended perturbation series, it is proposed to analyze the same problem using power series method. We assume power series solution of Eqs. (9) and (11) in the form

$$f(\lambda) = \sum_{n=1}^{\infty} a_n \lambda^{n+1}, \tag{24}$$

where

$$\sum_{n=1}^{\infty} a_n = 1; \qquad \sum_{n=1}^{\infty} (n+1) a_n = -\varphi \sum_{n=1}^{\infty} (n+1) n a_n; \tag{25}$$

$$\begin{aligned} a_3 &= 0; \\ a_{n+3} &= \frac{\mathrm{Re}_w}{(n+4)(n+3)(n+2)(n+1)} \sum_{m=1}^{n} \left[a_{n-m+1} a_m m(m+1)(2m-n-3) \right]. \end{aligned} \tag{26}$$

Eq. (25) comes from the boundary conditions at $\lambda = 1$ and Eq. (26) is obtained from Eq. (9). If a_1 and a_2 are known then the rest of $\{a_n\}$ can be found from the recurrence equation (26). Effectively, we have transformed a two point boundary value problem into a system of non-linear equations. To solve this system of non-linear equations, we have used both Brown's method(Byrne and Hall [7]) and Powell's method of unconstrained optimization(Press et al. [13]). It is implemented in analysing pressure gradient and other derived quantities.

6. The Finite Difference Solution

The diffusion equation (12), with the velocity obtained from Eqs. (20) and (21), is solved by a finite difference scheme implicit in λ.

The finite difference analogues of derivatives in Eq. (12) are

$$\frac{\partial C}{\partial X} = \frac{C_{j,m} - C_{j,m-1}}{\Delta X}, \tag{27}$$

$$\frac{\partial C}{\partial \lambda} = \frac{C_{j,m} - C_{j-1,m}}{\Delta \lambda}, \tag{28}$$

$$\frac{\partial^2 C}{\partial \lambda^2} = \frac{C_{j+1,m} - 2Cj, m + C_{j-1,m}}{\Delta \lambda^2}, \tag{29}$$

where m is subscript for x direction and j is subscript for the y-direction. Substituting Eqs. (27) – (29) into Eq. (12) gives

$$A_{j-1} C_{j-1,m} + B_j C_{j,m} + E_j C_{j+1,m} = F_j \qquad \text{for} \quad 2 \le j \le nj - 1, \tag{30}$$

where

$$A_{j-1} = -V_j \left(\frac{v_w L}{u_0 h}\frac{1}{\Delta\lambda}\right) - \left(\frac{DL}{u_0 h^2}\right)\frac{1}{\Delta\lambda^2}\,; \tag{31}$$

$$B_j = \frac{U_j}{\Delta X} + V_j \left(\frac{v_w L}{u_0 h}\right)\frac{1}{\Delta\lambda} + 2\left(\frac{DL}{u_0 h^2}\right)\frac{1}{(\Delta\lambda)^2}\,; \tag{32}$$

$$E_j = -\left(\frac{DL}{u_0 h^2}\right)\frac{1}{\delta\lambda}\,; \tag{33}$$

$$F_j = \frac{U_j}{\Delta x} C_{j,m-1}\,. \tag{34}$$

Eq. (30) is implicit in λ. At the non-porous boundary, $j = 1$, from Eq. (14), we have

$$\frac{\partial C}{\partial \lambda} = 0 \quad \Rightarrow \quad \frac{C_{j+1,m} - C_{j-1,m}}{2\Delta\lambda} = 0 \quad \Rightarrow \quad C_{2,m} = C_{0,m}. \tag{35}$$

Therefore from Eq. (30) we have

$$B_1 C_{1,m} + E_1 C_{2,m} = 0, \tag{36}$$

where

$$B_1 = V_1 \left(\frac{v_w L}{u_0 h}\right)\frac{1}{\Delta\lambda} + 2\left(\frac{DL}{u_0 h^2}\right)\frac{1}{\Delta\lambda^2}\,; \tag{37}$$

$$E_1 = -V_1 \left(\frac{v_w L}{u_0 h}\right)\frac{1}{\Delta\lambda} - 2\left(\frac{DL}{u_0 h^2}\right)\frac{1}{\Delta\lambda^2}\,. \tag{38}$$

Similarly, at the porous wall, from Eq. (15) we have

$$C_{nj+1,m} = 2\Delta\lambda \left[V_{nj,m} C_{nj,m}\left(\frac{v_w h}{D}\right)\right] + C_{nj-1,m}. \tag{39}$$

Therefore from Eq. (12), we have

$$A_{nj-1} C_{nj-1,m} + B_{nj} C_{nj,m} = F_{nj} \qquad \text{for} \quad j = nj, \tag{40}$$

where

$$A_{nj-1} = -V_{nj} \left(\frac{v_w L}{u_0 h}\right)\frac{1}{\Delta\lambda} - 2\left(\frac{DL}{u_0 h^2}\right)\frac{1}{\Delta\lambda^2}\,; \tag{41}$$

$$B_{nj} = \frac{U_{nj}}{\Delta X} + V_{nj} \left(\frac{v_w L}{u_0 h}\right)\frac{1}{\Delta\lambda} + 2\left(\frac{DL}{u_0 h^2}\right)\frac{1}{\Delta\lambda^2} - 2\frac{V_{nj} v_w L}{h u_0 \Delta\lambda}\,; \tag{42}$$

$$F_{nj} = \frac{U_{nj}}{\Delta X} C_{nj,m-1}\,. \tag{43}$$

The above system of Eqs. (30), (36) and (40) representing a tridiagonal system and are solved using Thomas algorithm.

7. Results and Discussion

The problem of laminar flow in a channel, one of the walls being porous with velocity slip at the porous medium is studied using computer extended series and also by power series method. The motion of the fluid is governed by a nonlinear ordinary differential equation (9) with boundary conditions (10), (11).

The universal polynomial functions $f_n(\lambda)$, $n = 1, 2, \ldots, 30$ are obtained by a recurrence relation and use MATHEMATICA (ver. 7) to generate them. This enables in obtaining a large number of universal polynomial functions $f_n(\lambda)$, $n = 1, 2, \ldots, 30$ for different slip coefficient φ. The series (20), (21) representing velocity profiles is analyzed using Padé approximants for different Reynolds numbers for its sum. The effect of slip coefficient on the velocity profiles for different Reynolds number is illustrated in Figs. 2, 3. Fig. 2 shows influence of the slip velocity on the mid channel axial velocity profile for an entrance Reynold number $\mathrm{Re}_{\mathrm{ent}} = 1000$ and a longitudinal position $x/h = 500$. These results are the curves plotted in figure for different slip coefficients

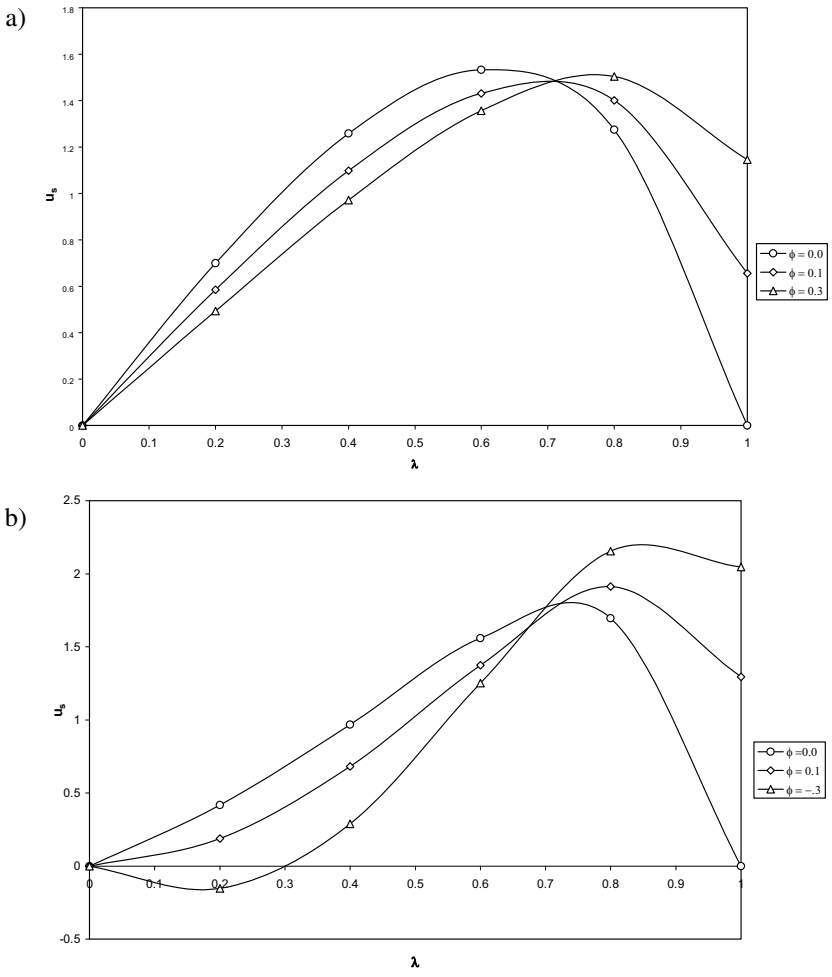

Fig. 4. Velocity profiles for channel flow with suction:
a) $\mathrm{Re}_w = 5$, b) $\mathrm{Re}_w = 10$.

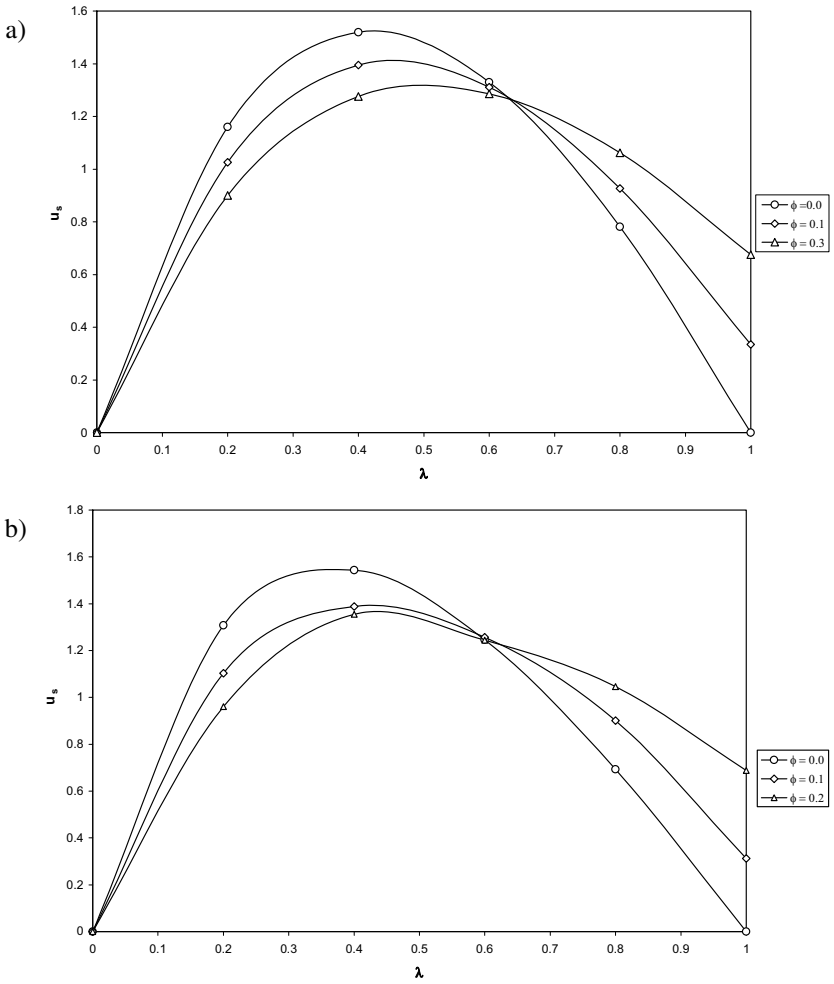

Fig. 5. Velocity profiles for channel flow with injection:
a) $\mathrm{Re}_w = -5,$ b) $\mathrm{Re}_w = -10.$

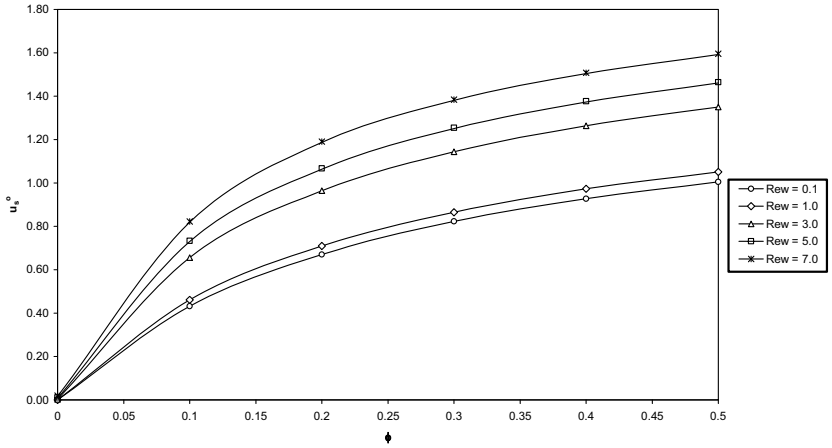

Fig. 6. Effect of slip coefficient on normalized slip velocity for various Re_w.

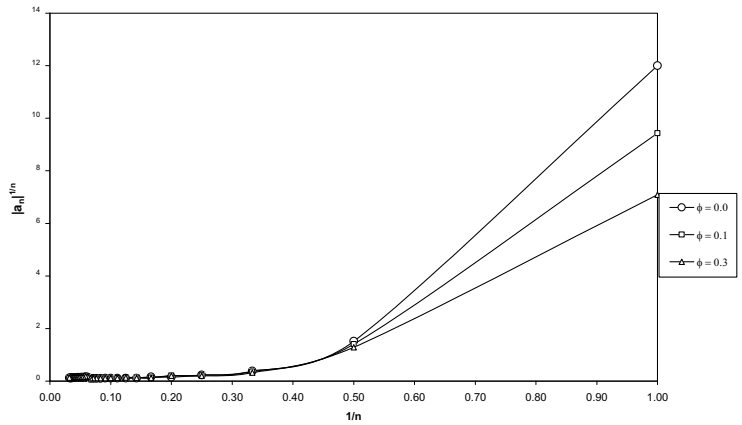

Fig. 7. Domb – Sykes plot for finding singularities of the series (23) representing ΔP for various slip coefficients.

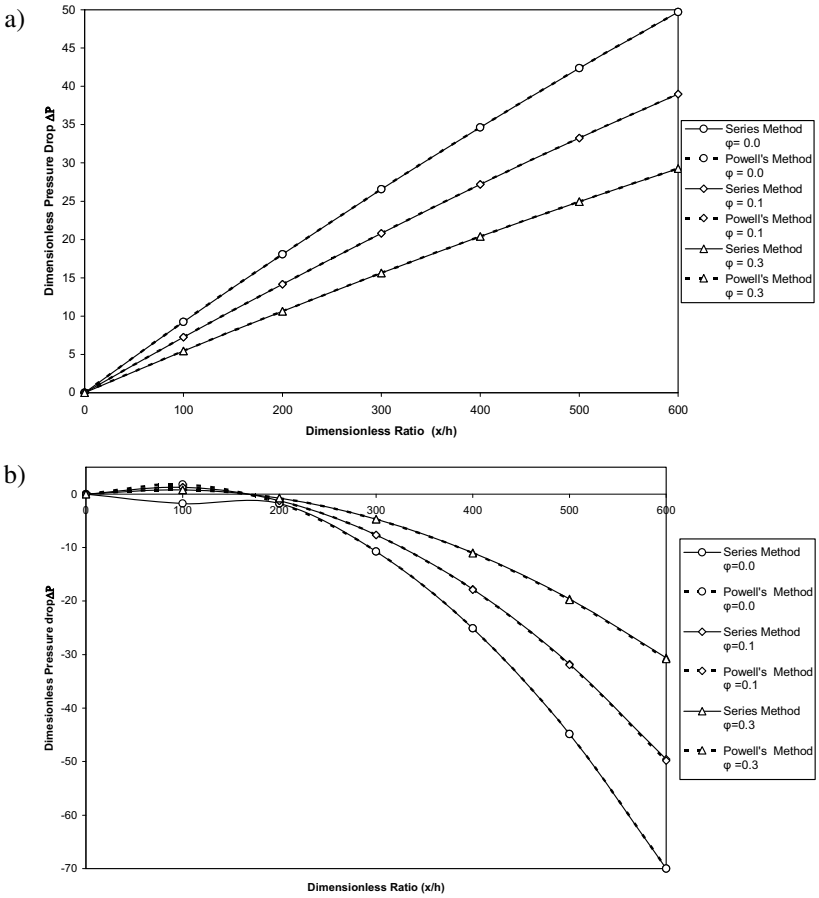

Fig. 8. Variation in the pressure drop in the channel as a function of the slip coefficient for $\mathrm{Re}_{\mathrm{ent}} = 1000$: a) $\mathrm{Re}_w = 0.1,$ b) $\mathrm{Re}_w = 3.$

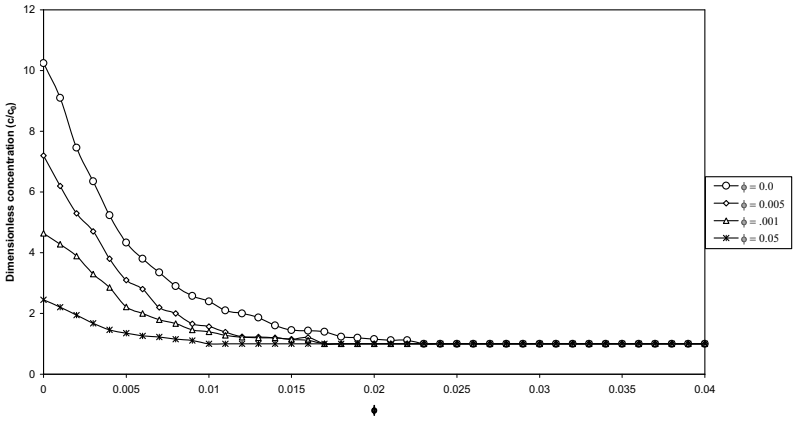

Fig. 9. Effect of fluid slip on concentration profiles near the porous wall at the mid-channel.

$\varphi = 0, 0.01, 0.05, 0.2, 0.3$. No slip case corresponds to $\varphi = 0$. It is seen that increasing slip leads to flattening of profiles and reduced wall shear stresses. Fig. 3 shows the effect of axial slip velocity on the mid channel transverse velocity profile. We calculate the velocity profiles for different Re_w using Padé sum. In Figs. 4 and 5 velocity profiles for channel flow with suction and injection respectively are given. Also, the effect of normalized slip velocity for various Re_w are shown in Fig. 6. u_s^0 increases with φ and approaches asymptotic values.

The coefficients a_n of the series (23) representing pressure gradient ΔP for different slip coefficients are decreasing in magnitude but have no regular sign pattern. Domb – Syke plots (Fig. 7) after extrapolation, confirms radius of convergence of the series (23) to be $\mathrm{Re}_w = 10.99, 10.29, 10.09$ (with an error of 10^{-5}) for $\varphi = 0, 0.1, 0.3$ respectively. The direct sum of the series for ΔP is valid only up to $\mathrm{Re}_w < 10.3$. We use Pade approximants (Bender and Orszag [3]) for summing the series. The Padé approximants for ΔP coincide with the earlier result for $\mathrm{Re}_w = 0.1$ (Chellam et al. [8]). We are able to obtain the values ΔP for sufficiently large Re_w (up to 3.0). To confirm the accuracy and validity of the results obtained, the problem is also solved by power series method. Here we have effectively transformed a two point boundary value problem into a system of nonlinear equations, which are solved by Brown's method as well as Powell's method of unconstrained optimization and the results are shown in Fig. 8 for different Reynolds numbers. Results shown in figures reveal that the magnitude of pressure gradient ΔP, increases with x/h for fixed entrance Reynolds number $\mathrm{Re}_{\mathrm{ent}} = 1000$. The effect of slip coefficient φ, at the porous (membrane) wall is to decrease ΔP, and also the larger the values of φ, the greater the reduction in the value of ΔP. This behavior is connected with the diminution in the shear stress at the membrane surface. Also it is observed that, an increase in Re_w will result in a decrease in ΔP.

The mass transfer equation (12) is analyzed using finite difference scheme and obtain concentration profiles c/c_0. In Fig. 9, we present the solution of the above Eq. (12), plotted for different slip coefficients, $\varphi = 0, 0.005, 0.01, 0.05$. The results agree with the earlier investigation(Chellam et al. [8]) and extend its validity for much larger values of Re_w. It is noted that the presence of a slip velocity reduces concentration polarization. Thus, the value of c/c_0 when $\varphi = 0.05$ is lower as compared to the one corresponding $\varphi = 0$. Also, it is observed that the effect of slip coefficient on the polarization is to promote diffusive transport of solute molecules from the membrane surface to the bulk solution. The net effect of this is to reduce polarization and increase flux rates through the membrane. Hence, the fluid slip will be a useful tool for modeling the fluid mechanics and mass transfer in dynamic membrane systems.

Acknowledgements

Authors thank referee for the valuable comments on the earlier version of the article.

REFERENCES

1. Beavers, G. S. and Joseph, D. D., Boundary Conditions at a Naturally Permeable Wall, *J. Fluid Mech.*, 1967, **30**, pp. 197–207.
2. Beavers, G. S., Sparrow, E. M., and Manguson, R. A., Experiments on Coupled Parallel Flows in a Channel and a Bounding Porous Medium, *ASME J. Basic Eng.*, 1970, **92**, pp. 843–848.
3. Bender, C. M. and Orszag, S. A., *Advanced Mathematical Methods for Scientists and Engineers*, Mc-Graw Hill, New York, 1987.
4. Berman, A. S., Laminar Flow in Channels with Porous Walls, *J. Appl. Phys.*, 1953, **24**, pp. 1232–1235.
5. Brady, J. F., Flow Development in a Porous Channel and Tube, *Phys. Fluids*, 1984, **27**, No. 5, pp. 1061–1067.
6. Bujurke, N. M., Pedley, T. J., and Tutty, O. R., Comparison of Series Expansion and Finite Difference Computations of Internal Laminar Flow Separation, *Phil. Trans. Roy. Soc. Lond.*, 1996, **A354**, pp. 1751–1773.
7. Byrne, G. and Hall, C., *Numerical Solution of Systems of Nonlinear Algebraic Equations*, Academic Press, New York, 1973.
8. Chellam, S., Wiesner, M. R., and Dawson, C., Slip at a Uniformly Porous Boundary: Effect on Fluid Flow and Mass Transfer, *J. Eng. Math.*, 1992, **26**, pp. 481–492.
9. Cox, S. M., Analysis of Steady Flow in a Channel with One Porous Wall, or with Accelerating Walls, *SIAM J. Appl. Math.*, 1991, **51**, No. 2, pp. 429–438.
10. Cox, S. M. and King, A. C., On the Asymptotic Solution of High-Order Nonlinear Ordinary Differential Equation, *Proc. Roy. Soc. Lond.*, 1997, **A453**, pp. 711–728.
11. King, J. R. and Cox, S. M., Asymptotic Analysis of The Steady-State and Time-Dependent Berman Problem, *J. Eng. Math.*, 2001, **39**, pp. 87–130.
12. Nield, D. A., The Beavers – Joseph Boundary Condition and Related Matters: A Historical and Critical Note, *Transp. Por. Media*, 2009, **78**, pp. 537–540.
13. Press, W. H., Flannery, B. P., and Teukolsky, S. A., *Numerical Recipes*, Cambridge Univ. Press, Cambridge, 1986.
14. Robinson, W. A., The Existence of Multiple Solutions for the Laminar Flow in a Uniformly Porous Channel with Suction at Both Walls, *J. Eng. Math.*, 1976, **10**, pp. 23–40.
15. Rudraih, N., Siddheshwar, P. G., and Masuoka, T., Nonlinear Convection in Porous Media: A Review, *J. Por. Media*, 2003, **6**, pp. 1–32.
16. Saffman, P. G., On the Boundary Condition at the Surface of a Porous Medium, *Stud. Appl. Math.*, 1971, **2**, pp. 93–101.
17. Terrill, R. M., Laminar Flow in a Uniformly Porous Channel, *Aeronaut. Quart.*, 1964, **15**, pp. 299–310.
18. Terrill, R. M., Laminar Flow in a Uniformly Porous Channel with Large Injection, *Aeronaut. Quart.*, 1965, **16**, pp. 323–332.
19. Terrill, R. M., Laminar Flow Through a Channel with Uniformly Porous Walls of Different Permeability, *Appl. Sci. Res., Sec. A*, 1965, **15**, pp. 440–468.
20. Terrill, R. M., Laminar Flow with Large Injection Through Parallel and Uniformly Porous Walls of Different Permeability, *Quart. J. Mech. Appl. Math.*, 1968, **21**, pp. 413–432.

21. Shavit, U., Special Issue on Transport Phenomena at the Interface Between Fluid and Porous Domains, *Transp. Por. Media*, 2009, **78**, pp. 327–330.
22. Van Dyke, M., Extended Stokes Series: Laminar Flow Through a Heated Horizontal Pipe, *J. Fluid Mech.*, 1990, **212**, pp. 289–308.
23. Zaturska, M. B., Drazin, P. G., and Banks, W. H. H., On the Flow of a Viscous Fluid Driven Along a Channel by Suction at Porous Walls, *Fluid Dyn. Res.*, 1988, **4**, pp. 151–178.

□◆◆◆□

Flows along a Symmetric Slotted Wedge and Heat Transfer[†]

Md. Anwar Hossain[1], **Saleem Ashgar**[2], and **T. Hayat**[3]

[1]On leave of absence from the Department of Mathematics, University of Dhaka
Dhaka, Bangladesh

[2]Department of Mathematics, COMSATS Institute of Information Technology
30, Sector H-8/1, Islamabad, Pakistan
E-mail: sashgar@comsats.edu.pk

[3]Department of Mathematics, Quid-e-Azam University
Islamabad, Pakistan

In the present paper the forced convection flow of a viscous incompressible fluid past a uniformly heated slotted wedge has been investigated numerically. The equations governing the flow and heat transfer are reduced to local similarity equations, treating $\xi = \beta x/\mathrm{Re}_x^2$, where Re_x is the local Reynolds number) as a local slip variable. The transformed boundary-layer equations are solved numerically using implicit finite difference method for all values of ξ in the interval $[0, 10^4]$. The solutions are also obtained for smaller values of ξ using the perturbation method. Further transformed equations has also been obtained appropriate for large values of ξ, which then have been integrated by the well established local nonsimilarity method. The asymptotic solutions for both smaller and larger values of ξ, obtained in terms of the local skin-friction and local rate of heat transfer for different pressure gradient m, are found in excellent agreement with that obtained by the finite difference solutions for all ξ.

* * *

Nomenclature

C_f	skin-friction coefficient;
f	non-dimensional, reduced stream function;
F	non-dimensional stream function f expressed in terms of η;
G	non-dimensional, reduced temperature function;
k	thermal conductivity of the fluid;
C_p	specific heat at constant pressure;
L	characteristic length;

[†]Received 15.04.2009

ISSN 1064-2277
© 2010 Begell House, Inc.

m	exponent;
Re_l	Reynolds number, $U_\infty L/\nu$;
Nu	local Nusselt number;
Pr	Prandtl number, $\nu\alpha$;
T	temperature of the fluid;
T_w	surface temperature of the wedge;
T_r	reference temperature;
T_∞	ambient temperature;
$\bar{u}_e(\bar{x})$	velocity of the potential flow;
U_∞	potential flow velocity;
$\bar{u}$, $\bar{v}$	velocity components along the $\bar{x}$, $\bar{y}$ axes, respectively;
$\bar{x}$, $\bar{y}$	Cartesian coordinate measured along the surface of the wedge and normal to it respectively.

Greek symbols

α	thermal diffusivity;
β	constant defining the included angle $\pi\beta$ of the wedge;
ρ	fluid density;
λ	ratio between Gr and Re^2;
η	transformed spatial variable;
μ	dynamic viscosity;
ν	(μ/ρ) kinematic viscosity;
ψ	non-dimensional stream function;
τ	non-dimensional, reduced time.

Introduction

It is well known that the skin-friction and heat transfer in two-dimensional, viscous, incompressible laminar flow over wedge-shaped bodies can accurately be calculated by solving the boundary layer differential equations. The momentum boundary layer equation for Falkner – Skan flow from a wedge, with potential flow velocity $u_e(x) = x^m$, was first deduced by Falkner and Skan [1]. The similarity solutions of the flow were later investigated in detailed by Hartree [2]. He obtained the solutions in terms of velocity distribution for different values of pressure gradient parameter. For flow over an arbitrary body shape with known pressure or velocity distribution where there exists no similarity, the skin-friction and heat transfer are conventionally found by an approximate method, either the integral method or the equivalent wedge flow approximation. Both of these methods yield sufficiently accurate results for most engineering applications. To apply the equivalent wedge flow method for the prediction of skin-friction and heat transfer it is necessary to have the solutions of the boundary layer equations for wedge type flows. Koh and Hartnett [3] have obtained the skin-friction and heat transfer for incompressible laminar flow over porous wedges with suction subjected to variable wall temperature.

In the boundary layer with the effect of suction/blowing similarity solution is possible only when the suction/blowing rate is proportional to $x^{(m-1)/2}$, where x is the distance from the leading edge and m is the pressure gradient parameter. Koh and Hartnett [3] studied the incompressible laminar flow over porous wedge with suction and variable wall temperature. The similarity solution is obtained when the variations of the wall temperature and the suction rate are proportional to power-law of x. From the practical point of view, the transpiration velocity may be more easily

realized than with $x^{(m-1)/2}$. Watanabe [4] investigated thermal boundary layer over a uniform wall temperature wedge with transpiration velocity in forced flow. Yih [5] extended the above problem by investigating the heat transfer characteristics in the forced flow over a wedge subjected to uniform wall heat flux. Hossain et al. [6] investigated the non-Darcy forced convection boundary layer flow over a wedge embedded in a saturated porous medium. Flow of viscous incompressible fluid with temperature dependent viscosity and thermal conductivity past a permeable wedge with uniform surface heat flux has been studied by Hossain et al. [7, 8].

Recently, Laplace and Arquis [9] investigated the boundary layer flow over a slotted plate; since perforated plates and wire netting occurs in much application of fluid mechanics (such as perforated wings in order to reduce the turbulence by suction of the boundary layer, filtration or air-conditioning). These media are often characterized by their pressure drop coefficient which is mostly determined experimentally. When faced with a tangential flow, no-slip hypothesis is generally taken and this assumption is no longer valid when the perforation density is sufficiently large. In a boundary layer flow this will have consequence for the displacement thickness. Working on a ideal two-dimensional periodic perforated media placed in a purely tangential flow it has been proved by Laplace and Arquis [9] that the boundary condition $dV/dn = \beta V$, introduced by Navier in the 19^{th} century and linking the shear stress at the wall and slip velocity by the coefficient β, applies to slotted plate. By means of an experimental study, this slip condition (called the Navier condition hereafter) was revived empirically by Beavers and Joseph [10] for a fluid-porous medium interface. A theoretical justification for it was given by Saffman [11]. The Navier condition was also used by Richardson [12], Hocking [13] and recently by Miksis and Davis [14], Tuck and Kouzobov [15] and by Sarkar and Prosperetti [16] to study tangential viscous fluid flows over periodic or stochastic rough surfaces.

The purpose of the present paper is the complement to the work of Laplace and Arquis [9] for the forced convection flow past a uniformly heated slotted wedge. The equations that govern the flow and heat transfer are reduced to local similarity equations, treating the local similarity variable, $\xi = \beta x/\mathrm{Re}_x^2$, where Re_x is the local Reynolds number). The transformed boundary-layer equations are solved numerically using implicit finite difference method together with Keller box elimination technique [17] for all values of ξ in the interval $[0, 10^4]$. The solutions are also obtained for smaller values of ξ using the perturbation method. Inverse transformation has also been implemented to obtain the associated equations appropriate for asymptotic solution, which then have been integrated by the local nonsimilarity method of Sparrow et al. [18,19]. The results are expressed in terms of the local skin-friction and local rate of heat transfer coefficients against ξ for varying pressure gradient m and depicted graphically. The asymptotic solutions for both smaller and larger values of ξ are found in excellent agreement with that obtained by the finite difference solutions for all ξ.

1. Formulation of the Problem

A steady two-dimensional laminar boundary-layer flow of a viscous incompressible fluid past a symmetrical wedge having the surface as slotted (or with partial sleep condition). The inviscid flow over the wedge develops instantaneously and its velocity is given by

$$\overline{u}_e(\overline{x}) = U_\infty \left(\frac{\overline{x}}{L}\right)^m \qquad \text{for} \qquad m \leq 1, \tag{1}$$

where L is a characteristic length and m is pressure gradient related to the included angle $\pi\beta$ by $m = \beta/(2-\beta)$. It is clear that for negative values of m the solution becomes singular at $\overline{x} = 0$, whilst for m positive the solution can be defined for all values of $\overline{x}$, and this leads to a general

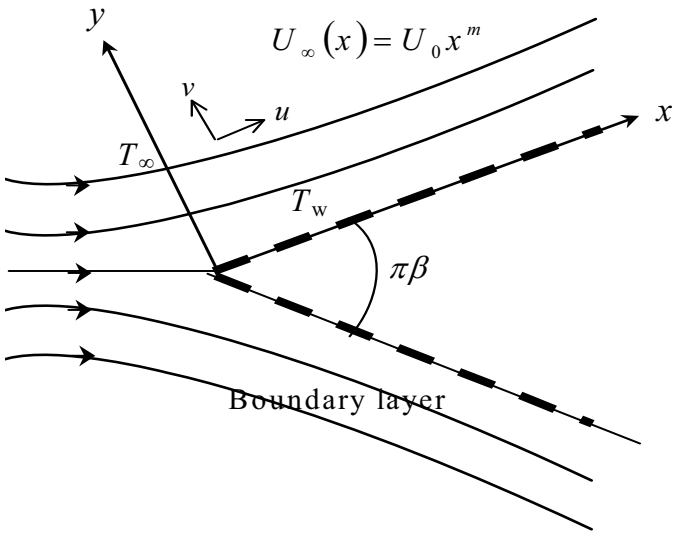

Fig. 1. Flow configuration and coordinate system.

difference between the solutions for the case of $m < 0$ and $m \geq 0$. The physical configuration considered is as shown in Fig. 1.

We consider that the flow is governed by the following equations:

$$\frac{\partial \overline{u}}{\partial \overline{x}} + \frac{\partial \overline{v}}{\partial \overline{y}} = 0, \tag{2}$$

$$\overline{u}\frac{\partial \overline{u}}{\partial \overline{x}} + \overline{v}\frac{\partial \overline{u}}{\partial \overline{y}} = \overline{u}_e \frac{\partial \overline{u}_e}{\partial \overline{x}} + \nu \frac{\partial^2 \overline{u}}{\partial \overline{y}^2}\,, \tag{3}$$

$$\overline{u}\frac{\partial \overline{T}}{\partial \overline{x}} + \overline{v}\frac{\partial \overline{T}}{\partial \overline{y}} = \frac{k}{\rho C_p}\,\frac{\partial^2 \overline{T}}{\partial \overline{y}^2}\,, \tag{4}$$

where ρ is the density; k is the thermal conductivity; C_p is the specific heat at constant pressure; $\nu = \mu/\rho$ is the kinematic viscosity, where μ is the constant viscosity of the fluid in the boundary layer region.

The boundary conditions for the present problems are

$$\begin{aligned} &\frac{\partial \overline{u}}{\partial \overline{y}} = \lambda \overline{u}, \quad \overline{v} = 0, \quad \overline{T} = T_w(\overline{x}) \quad \text{at} \quad \overline{y} = 0 \\ &\qquad \overline{u} = \overline{u}_e(\overline{x}), \qquad\qquad \overline{T} \to 0 \qquad \text{as} \quad \overline{y} \to \infty. \end{aligned} \tag{5}$$

In the boundary condition λ is defined as slip constant. It can be used to express the boundary behavior of total adhesion ($\lambda = +\infty$ and therefore $\overline{u} = 0$) and of total slip ($\lambda = 0$ and that implies $\partial \overline{u}/\partial \overline{y} = 0$). This has been proved by Laplace and Arqus [9] that this partial slip boundary condition applies to slotted surface.

We introduce non-dimensional dependent and independent variables according to

$$\begin{gathered} x=\frac{\overline{x}}{L}\,, \qquad y=\mathrm{Re}_L^{1/2}\frac{\overline{y}}{L}\,, \qquad u=\frac{\overline{u}}{U_\infty}\,, \qquad v=\mathrm{Re}_L^{1/2}\frac{\overline{v}}{U_\infty}\,, \\ u_e=\frac{\overline{u}_e}{U_\infty}\,, \qquad T=\frac{T_w-T_\infty}{T_r-T_\infty}\,, \qquad \mathrm{Re}_L=\frac{U_\infty L}{\nu}\,. \end{gathered} \tag{6}$$

The velocity over the wedge is now given by

$$u_e(x)=x^m \qquad \text{for} \qquad 0\le m\le 1 \tag{7}$$

and, sufficiently far downstream from the apex, the governing equations (2) – (4) can be written as

$$\frac{\partial u}{\partial x}+\frac{\partial v}{\partial y}=0, \tag{8}$$

$$u\frac{\partial u}{\partial x}+v\frac{\partial u}{\partial y}=u_e\frac{\partial u_e}{\partial x}+\nu\frac{\partial^2 u}{\partial y^2}\,, \tag{9}$$

$$u\frac{\partial T}{\partial x}+v\frac{\partial T}{\partial y}=\frac{1}{\mathrm{Pr}}\,\frac{\partial^2 T}{\partial y^2}\,, \tag{10}$$

The boundary conditions then turn to

$$\begin{aligned} &\frac{\partial u}{\partial y}=su, \quad v=0, \quad T=1 \quad \text{at} \quad y=0 \\ &u=u_e(x)=x^m, \quad T\to 0 \quad \text{as} \quad y\to\infty, \end{aligned} \tag{11}$$

where $s=\beta L/\mathrm{Re}_L^{1/2}$ is the slotted (or partial slip) parameter.

The number of independent variables in the governing Eqs. (8) – (10) can be reduced from three to two by introducing the non-dimensional, reduced stream function $F(\eta,\tau)$ and the non-dimensional, reduced temperature function $G(\eta,\tau)$ according to,

$$\begin{aligned} &\psi=x^{(m+1)/2}F(\eta,\xi), \qquad T=G(\eta,\xi), \\ &\eta=x^{(m-1)/2}y, \qquad \xi=sx^{(1-m)/2}, \end{aligned} \tag{12}$$

where η is a non-dimensional similarity variable, ξ is termed as the local partial slip parameter and ψ is the stream function, which is defined in the usual way, namely

$$u=\frac{\partial\psi}{\partial y} \quad \text{and} \quad v=-\frac{\partial\psi}{\partial x}.$$

Substituting the transformation (12) into Eqs. (9) and (10), we obtain:

$$F'''+\frac{m+1}{2}FF''+m(1-F'^2)=\frac{1-m}{2}\xi\left[F'\frac{\partial F'}{\partial\xi}-F''\frac{\partial F}{\partial\xi}\right], \tag{13}$$

$$\frac{1}{\mathrm{Pr}}G''+\frac{m+1}{2}FG'=\frac{1-m}{2}\xi\left[F'\frac{\partial G}{\partial\xi}-G'\frac{\partial F}{\partial\xi}\right]. \tag{14}$$

The boundary conditions to be satisfied by the above equations are

$$F(0,\xi)=0, \qquad F''(0,\xi)=\xi F'(0,\xi), \qquad G(0,\xi)=1$$
$$F'(\infty,\xi)=1, \qquad G(\infty,\xi)=0. \tag{15}$$

In this above equations, prime denotes differentiation of the functions with respect to η.

Taking $m = 0$ and neglecting terms with ξ from the right sides of Eqs. (13) and (14) one reaches to the equations investigated by Laplace and Arquis [9] for the case of a flat slotted surface.

In practical applications, two quantities of physical interest to be determined are surface shear stress and the rate of heat transfer at the surface, which may be obtained in terms of the local skin friction

$$C_f = 2\tau_w(\overline{x})/\rho\overline{u}_e^2 \tag{16}$$

and the local Nusselt number

$$\mathrm{Nu} = q_w(\overline{x})\overline{x}/k(T_w - T_\infty), \tag{17}$$

where

$$\tau_w(\overline{x}) = \mu\left(\frac{\partial\overline{u}}{\partial\overline{y}}\right)_{\overline{y}=0} \quad \text{and} \quad q_w(\overline{x}) = -k\left(\frac{\partial\overline{T}}{\partial\overline{y}}\right)_{\overline{y}=0} \tag{18}$$

are the surface shear stress and the surface heat flux, respectively.

By introducing the non-dimensional variables Eq. (6) and the transformation Eq. (12), the skin friction coefficient, $C_f\mathrm{Re}_x^{1/2}$ and the local Nusselt number, $\mathrm{NuRe}_x^{1/2}$ are given by,

$$\frac{1}{2}C_f\mathrm{Re}_x^{1/2} = \xi F'(0,\xi), \tag{19}$$

$$\mathrm{NuRe}_x^{1/2} = -G(0,\xi). \tag{20}$$

Once we know the values of $F'(0,\xi)$ and $G'(0,\xi)$ from the solutions of the governing equations (13)–(15) we get the values of the skin friction coefficient and the local Nusselt number from the relations (19) and (20).

It should be mentioned here for flat slotted surface that had been investigated by is obtained by taking $m = 0$ and neglecting the right hand terms of the Eq. (13), and that is

$$F''' + \frac{1}{2}FF'' = 0. \tag{21}$$

The boundary conditions to be satisfied by the above equations are

$$F(0,\xi)=0, \qquad F''(0,\xi)=\xi F'(0,\xi), \qquad F'(\infty,\xi)=1. \tag{22}$$

It can be seen that, for the slotted surface, the function does not depend not only the similarity variable η, it also depends implicitly on ξ and that's why in the present investigation we have considered the stream function F as a function of η and ξ and so is the case with temperature function, G that ultimately gave better results than that had been obtained by Laplace and Arquis [9]. Here we revisit the problem posed through Eqs. (21) and (15), than those proposed by Laplace and Arquis and the results thus obtained in terms of local skin-friction coefficients have been compared in Fig. 2 with the solutions obtained from the present considerations. One can see that the present solutions are better than that obtained in [9], since from the present transformed local nonsimilarity equations one can reach to the asymptotic solution at large ξ that corresponds to the Falkner – Skan flow and heat transfer (that one can see easily from Fig. 3.

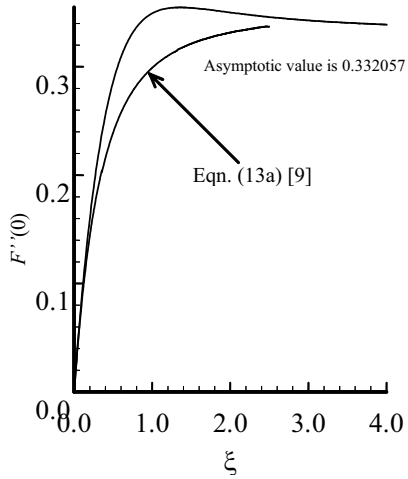

Fig. 2. Comparison on the solutions of Eq. (21) with that of Eq. (13), while $m = 0$ satisfying the prescribed boundary conditions.

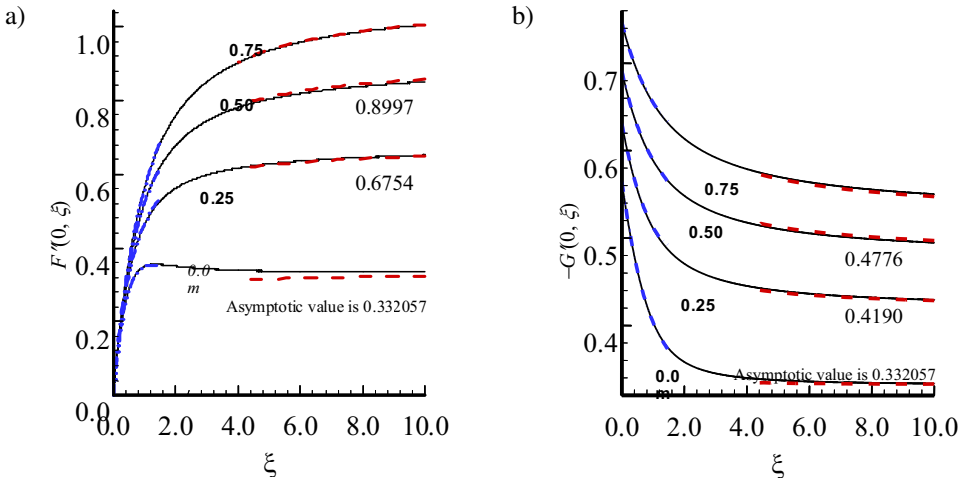

Fig. 3. Numerical values for different values of m against ξ:
a) skin-friction coefficient $F''(0,\xi)$, b) coefficient of local rate of heat transfer $-G'(0,\xi)$.

2. Solution Methodologies

The nonlinear system of partial differential equations (16) and (17) that govern the flow have been integrated employing the implicit finite difference method (FDM) together with the Keller-box scheme (details of this method had been discussed elaborately by Cebeci and Bradshaw [17]). To employ this method, the Eqs. (16) and (17), first, are written in terms of first order equations in η, which are then expressed in finite difference form by approximating the functions and their derivatives in terms of there central differences in both coordinate directions. Denoting the mesh

points in the (η, ξ) plane by ξ_i and η_j, where $i = 1, 2, 3, \ldots, M$ and $j = 1, 2, 3, \ldots, N$, central difference approximations are made such that the equations involving x explicitly are centered at $(\xi_{i-1/2}, \eta_{j-1/2})$ and the remainder at $(\xi_i, \eta_{j-1/2})$, where $\eta_{j-1/2} = (\eta_j + \eta_{j-1})/2$, etc. This results in a set of nonlinear difference equations for the unknowns at x_i in terms of their values at ξ_{i-1}. These equations are then linearized by the Newton's quasilinearization technique and are solved using a block-tridiagonal algorithm, taking as the initial iteration of the converged solution at $\xi = \xi_{i-1}$. Now to initiate the process at $\xi = 0$, we first provide guess profiles for all five variables (arising the reduction to the first order form) and use the Keller-box method to solve the governing ordinary differential equations. Having obtained the lower stagnation point solution it is possible to march step by step along the boundary layer. For a given value of x, the iterative procedure is stopped when the difference in computing the velocity and the temperature in the next iteration is less than 10^-6, i. e., when $|\delta f^i| \leq 10^6$, where the superscript denotes the iteration number. The computations were not performed using a uniform grid in the η direction, but a non uniform grid was used and defined by $\eta_j = \sinh(j-1)/a$, with $j = 1, 2, \ldots, 301$ and $a = 100$ to get $\eta_{max} = 10.02$. On the otherhand in ξ direction the grid length has been chosen as $\Delta\eta = 10^{-5}$. To initiate the solutions for increasing values of ξ the initial profile has been taken from the solution of Eqs. (25) and (26) together with the boundary conditions given in Eq. (27).

In what follows we discuss the solutions of the present problem for small and large values of the local slip parameter, ξ. For small values of ξ the regular perturbation method has been employed treating ξ as small and for large ξ values the governing equations have been transformed to a different set of partial differential equations that are suitable for large ξ values. The resulting equations are then integrated using the local nonsimilarity method.

2.1. Solutions for small ξ. For small values of ξ we consider that the function posses the following form

$$F(\eta, \xi) = \sum_{i=0}^{\infty} \xi^i F_i(\eta) \quad \text{and} \quad G(\eta, \xi) = \sum_{i=0}^{\infty} \xi^i G_i(\eta). \tag{23}$$

For convenience, we assume that

$$p_1 = \frac{1+m}{2}, \qquad p_2 = m, \qquad p_0 = \frac{1-m}{2}. \tag{24}$$

Substituting the transformation (12) into Eqs. (9) and (10), and equating the coefficients of ξ^i, we may get the following sets of equations:

$$F_0''' + p_1 F_0 F_0'' + p_2(1 - F_0^{'2}) = 0, \tag{25}$$

$$\frac{1}{\mathrm{Pr}} G_0'' + p_1 F_0 G_0' = 0. \tag{26}$$

The boundary conditions to be satisfied by the above equations are

$$\begin{gathered} F_0 = 0, \quad F_0''(0) = 0, \quad G_0(0) = 1 \\ F_0'(\infty) = 1, \qquad G_0(\infty) = 0 \end{gathered} \tag{27}$$

and for $i \geq 1$ the equations are

$$F_i''' + \sum_{i=1}^{k} (p_1 + k p_0) F_i F_{k-i}'' - \sum_{i=1}^{k} (p_2 + k p_0) F_i' F_{k-i}' = 0, \tag{28}$$

$$\frac{1}{\mathrm{Pr}}G_i'' + \sum_{i=1}^{k}\left[(p_1 + kp_0)F_iG_{k-i}' - kp_0F_i'G_{k-i}\right] = 0. \tag{29}$$

Corresponding boundary conditions should be as follows:

$$\begin{aligned} F_i(0) = 0, \quad F_i(0)'' = F_{i-1}(0), \quad G_i(0) = 0 \\ F_i'(\infty) = 0, \qquad\qquad G_i(\infty) = 0. \end{aligned} \tag{30}$$

Solutions of the set of Eqs. (25) and (26) are obtained using the standard shooting method, and the later sets (28) and (29) are solved using the method of superposition. For different values of m while $\mathrm{Pr} = 1$. Usually, one calculates only a few terms of a perturbation expansion, that is, two or three. But here we have taken the terms up to 16. Results thus obtained in terms of local skin-friction coefficient and the local heat transfer coefficients are shown graphically in the Figs. 3a and b, respectively.

2.2. Solutions for large ξ. Now we shall give attention to the behavior of the solution of Eqs. (13) and (15) when ξ is large. The boundary conditions Eq. (15) suggest that at large ξ the flow should be as that of the Falkner – Skan flow. Accordingly we simply introduce the new variable $\zeta = 1/\xi$ in place of ξ in the equations through Eqs. (13)- (15) and get the following relations:

$$F''' + \frac{m+1}{2}FF'' + m(1 - F^{'2}) = \frac{m-1}{2}\zeta\left[F'\frac{\partial F'}{\partial \zeta} - F''\frac{\partial F}{\partial \zeta}\right], \tag{31}$$

$$\frac{1}{\mathrm{Pr}}G'' + \frac{1+m}{2}FG' = \frac{m-1}{2}\zeta\left[F'\frac{\partial G}{\partial \zeta} - G'\frac{\partial F}{\partial \zeta}\right]. \tag{32}$$

The boundary conditions to be satisfied by the above equations are

$$\begin{aligned} F(0,\xi) = 0, \quad F'(0,\xi) = \zeta F''(0,\xi), \quad G(0,\xi) = 1 \\ F'(\infty,\xi) = 1, \qquad\qquad G(\infty,\xi) = 0. \end{aligned} \tag{33}$$

It can be seen clearly that for $= 0$, above set of equations take the form of that of Falkner – Skan flow and heat transfer. To get better results, instead of perturbation solutions, with a little effort we employ here the local non-similar method.

The local nonsimilarity method initiated by Chen and Sparrow [18] and has since been applied by many investigators to solve various non-similarity boundary value problems, such as, Minkowycz and Sparrow [19] and Hossain et al. [6–8]. A brief formulation of the systems of equations for the local nonsimilarity models, with reference to the present problem, will be demonstrated below now.

Using this non-similarity approach we have the following equations:

$$F''' + p_1FF'' + p_2(1 - F^{'2}) - p_0\zeta\left[F'f' - F''f\right] = 0, \tag{34}$$

$$\frac{1}{\mathrm{Pr}}G'' + p_1FG' - p_0\zeta\left[F'g - G'f\right] = 0, \tag{35}$$

$$f''' + p_1Ff'' + (p_1 - p_0)F''f + (2p_2 - p_0)F'f' + p_0\zeta\left[f^{'2} - f''f\right] = 0, \tag{36}$$

$$\frac{1}{\mathrm{Pr}}g'' + p_1 F g' + (p_1 - p_0)G'f - p_0\zeta\,[f'g - g'f] = 0. \tag{37}$$

The boundary conditions to be satisfied by the above equations are

$$\begin{gathered} F(0,\zeta) = 0, \quad F'(0,\zeta) = \zeta F''(0,\zeta), \quad G(0,\zeta) = 1, \\ F'(\infty,\zeta) = 1, \qquad\qquad G(\infty,\zeta) = 0; \end{gathered} \tag{38}$$

$$\begin{gathered} f(0,\zeta) = 0, \quad f'(0,\zeta) = F''(0,\zeta) + \zeta f''(0,\zeta), \quad g(0,\zeta) = 1, \\ f'(\infty,\zeta) = 1, \qquad\qquad g(\infty,\zeta) = 0. \end{gathered} \tag{39}$$

Here we have introduced the new variables as defined below:

$$f = \frac{\partial F}{\partial \zeta} \quad \text{and} \quad g = \frac{\partial G}{\partial \zeta} \tag{40}$$

and obtained the equations up to second level of truncation, neglecting terms of $\partial f/\partial\zeta$ and $\partial g/\partial\zeta$ as well as that of the higher order derivatives for the functions F and G with respect to η.

However, solutions of the set of four equations (34) – (37) are obtained subject to boundary conditions Eq. (38) using the Nachtsheim and Swigert iteration technique of Nachtsheim and Swiegert [20] together with sixth order implicit Runge – Kutta – Butcher method. Results thus obtained in terms of the coefficients of local skin-friction, $F''(0,\xi)$, and local Nusselt number, $G'(0,\xi)$ are for different values of the potential flow parameter m.

3. Results and Discussion

Here we have investigated the problem of forced flow and heat transfer of a viscous incompressible fluid past a slotted wedge with uniform surface temperature. Solutions are obtained for fluids having Prandtl number, $\mathrm{Pr} = 1.0$ against the local slotted parameter, ξ. We depicted the numerical values of $F(0,\xi)$ in Fig. 3a for $m = 0$, 0.25, 0.5, 0.75. In this figure we also presented the numerical values of $F(0,\xi)$ obtained by the extended series solutions obtained for small ξ values and also that obtained by the local nonsimilarity method applied for the problem derived appropriate for large values of ξ. It can be seen that these solutions are in excellent agreement, for both small and large values of ξ, with that we obtained for entire values of ξ obtained by the implicit finite difference for all values of the pressure gradient parameter m. The similar observation can also be seen in case of the corresponding heat transfer case which has been depicted in Fig. 3b.

From this figure we observe that the value of the skin-friction coefficient, $F(0,\xi)$, increases due to the increase of pressure gradient parameter, m, for the fluid of different Prandtl number, Pr. This is expected, since increase in the value m leads to increase the pressure gradient in the boundary layer and thus for higher pressure gradient the surface skin-friction will rise. It may further be observed that as the value of local slip parameter ξ increases, the numerical value of the local skin-friction lead to increase and approaches to the asymptotic values. The asymptotic values of the skin-friction coefficients are 0.33205, 0.6754, and 0.8997 that corresponds to the values of $m = 0$, 0.25, and 0.5.

For different values of the pressure gradient parameter m the numerical values of the local rate of heat transfer coefficients $G(0,\xi)$ are shown graphically in Fig. 3b against the values of ξ. In this

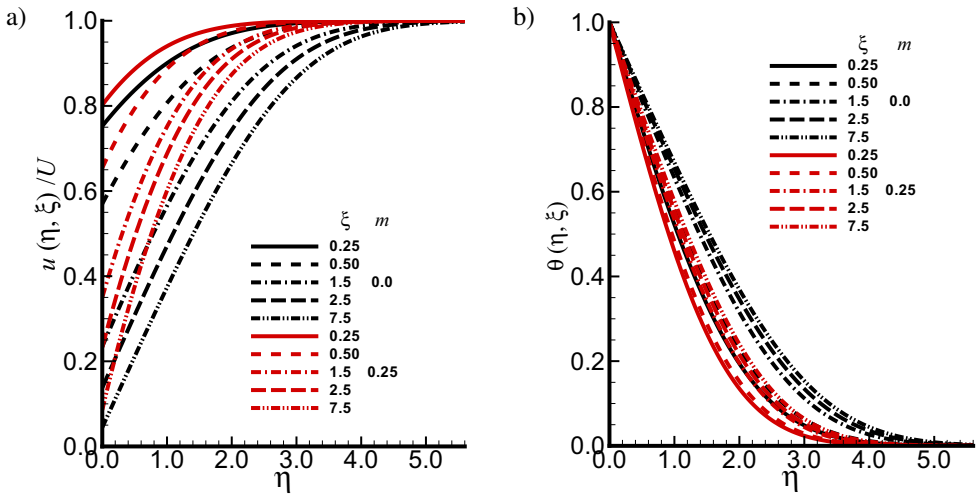

Fig. 4. Dimensional field profiles for $m = 0$ and 0.25 at different values of ξ against η::
a) velocity $u(\eta, \xi)/U$, b) temperature $\theta(\eta, \xi)$.

case also we observe that there is an increase of the value of the rate of heat transfer coefficient $G(0, \xi)$, owing to increase in the pressure gradient parameter m. We further observe that, at every value of the parameter m, the value of the rate of heat transfer coefficient $G(0, \xi)$, decreases due to increase in the value of local slip parameter ξ and approaches to the respective asymptotic values as shown in the Fig. 3b. The asymptotic values of the rate of heat transfer coefficient are 0.332057 for $m = 0, 0.25, 0.5$ and 0.75, respectively.

Fig. 4a depicts the velocity profile for different values of ξ $(0.25,\ 0.5,\ 1.25,\ 2.5,\ 7.25)$ while $m = 0$ and 0.25. From graph it can be seen that increase in the value of slip parameter ξ leads to decrease in the velocity profile near the surface of the wedge but at larger values of ξ the surface will act as slip free surface and hence the velocity field will act as that case of no-slip boundary condition $F'(0) = 0$.

Finally, we have shown the temperature profiles, for fluid having $\mathrm{Pr} = 1$, for different values of the local slip parameter ξ as mentioned before (Fig. 4b). Here one can observe that the temperature profile decreases owing to increase in the value of the local slip parameter, ξ. We further observe, as we have in case of velocity profile, further increase of the value of ξ will to the case of the temperature field with non-slip boundary condition of the on the surface of the wedge. In this figure affect of the pressure gradient parameter m on the temperature field has also been shown. This can be observed that an increase of the parameter m leads to decrease in the temperature field in the boundary layer region, since there is rise in the heat transfer from the surface with the increase of the pressure gradient parameter.

Conclusions

In the present investigation, flow of a viscous fluid and heat transfer from a wedge with partial slip (slotted) condition at the surface has been considered. The reduced equations governing the flow have been derived as local nonsilmiarity equations with respect to the local variable, ξ, the local slip parameters. Solutions of these equations are obtained employing three methods, namely, the perturbation method for small ξ, asymptotic solutions for large ξ using the local nonsimilarity

method and the finite difference method for entire region of ξ values. The present work not only augmented to what has been presented in [9] in application of their theory for Blasius flow, it further extends to the case of perforated wedge and includes the heat transfer phenomena due to uniformly heating of the wedge.

Following conclusions can be obtained from the present investigation.

1. It is observed that the friction coefficient increases with increase of pressure gradient, which is expected for the increase of m.
2. Another important observation is that with the increase of local slip parameter, the skin-friction increases and approaches to its no-slip asymptotic values.
3. We further notice that the rate of heat transfer coefficient also increases due to increase in the value of the local slip parameter.

REFERENCES

1. Falkner, V. M. and Skan, S. W., Some Approximate Solutions of the Boundary-Layer Equations, *Phil. Mag.*, 1930, **12**, ARC RM 1314, pp. 865–896.
2. Hartree, D. R., On Equations Occurring in Falkner and Skan's Approximate Treatment of the Equations of Boundary-Layer, *Proc. Cambr. Phil. Soc.*, 1937, **33**, pp. 223–239.
3. Koh, J. C. Y. and Hartnett, J. P., Skin-Friction and Heat Transfer for Incompressible Laminar Flow Over Porous Wedges with Suction and Variable Wall Temperature, *Int. J. Heat Mass Transfer*, 1961, **2**, pp. 185–198.
4. Watanabe, T., Thermal Boundary Layer Over a Wedge with Uniform Suction or Injection in Forced Flow, *Acta Mech.*, 1990, **83**, pp. 119–126.
5. Yih, K. A., Uniform Suction/Blowing Effect on Thee Forced Convection About a Wedge: Uniform Heat Flux, *Acta Mech.*, 1998, **128**, pp. 173–181.
6. Hossain, M. A., Banu, N., and Nakayama, A., Non-Darcy Forced Convection Boundary Layer Flow over a Wedge Embedded in a Saturated Porous Medium, *Num. Heat Transfer*, 1994, **26**, pp. 399–418.
7. Hossain, M. A., Munir, M. S., and Rees, D. A. S., Flow of Viscous Incompressible Fluid with Temperature Dependent Viscosity and Thermal Conductivity Past a Permeable Wedge with Uniform Surface Heat Flux, *Int. J. Therm. Sci.*, 2000, **39**, pp. 635–644.
8. Hossain, M. A., Munir, M. S., Hafiz, Z., and Takhar, H. S., Flow of Viscous Incompressible Fluid with Temperature Dependent Viscosity Past a Permeable Wedge with Uniform Surface Heat Flux, *Heat Mass Transfer*, 2000, **4**, pp. 333–341.
9. Laplace, P. and Arquis, E., Boundary Layer Over a Slotted Plate, *Eur. J. Mech. B / Fluid*, 1998, **17**, pp. 331–355.
10. Beavers, G. S. and Joseph, D. D., Boundary Conditions at a Naturally Permeable Wall, *J. Fluid Mech.*, 1967, **30**, pp. 197–207.
11. Saffman, P. G., On the Boundary Condition at the Surface of a Porous Medium, *Stud. Appl. Math.*, 1971, **2**, pp. 93–101.
12. Richardson, S., On the No-Slip Boundary Condition, *J. Fluid Mech.*, 1973, **49**, pp. 125–139.
13. Hocking, L. M., A Moving Fluid on a Rough Surface, *J. Fluid Mech.*, 1976, **76**, pp. 801–817.
14. Miksis, M. J. and Davis, S. H., Slip Over Rough and Coated Surfaces, *J. Fluid Mech.*, 1994, **273**, pp. 125–139.
15. Tuck, E. O. and Kouzoubov, A., A Laminar Roughness Boundary Condition, *J. Fluid Mech.*, 1995, **300**, pp. 59–70.

16. Sarkar, K. and Prosperitti, A., Effective Boundary Condition for Stokes Flow Over a Rough Surface, *J. Fluid Mech.*, 1996, **316**, pp. 223–240.
17. Cebeci, T. and Bradshaw, P., *Physical and Computational Aspects of Convective Heat Transfer*, Springer, New York, 1984.
18. Chen, T. S. and Sparrow, E. M., Flow and Heat Transfer over a Flat Plate with Uniformly Distributed, Vectored Surface Mass Transfer, *ASME J. Heat Transfer*, 1976, **98**, pp. 674–676 .
19. Minkowycz, W. J. and Sparrow, E. M., Numerical Solution Scheme for Local Non-Similarity Boundary-Layer Analysis, *Num. Heat Transfer*, 1978, **1**, pp. 69–85.
20. Nachtsheim, P. R. and Swiegert, P., Satisfaction of Asymptotic Boundary Conditions in Numerical Solutions of System of Nonlinear Equations of the Boundary Layer Type, *NASA TN D-3004*, 1965.

□◆◆◆□